# A FRAMEWORK OF INTEGRATED PRODUCT DESIGN AND CONTROL IN MANUFACTURING POLYMER NANOCOMPOSITES

by

Qian Gou

A dissertation submitted to the Faculty of the University of Delaware in partial fulfillment of the requirements for the degree of Doctor of Philosophy in Chemical Engineering

Spring 2014

© 2014 Qian Gou
All Rights Reserved

UMI Number: 3631178

All rights reserved

INFORMATION TO ALL USERS
The quality of this reproduction is dependent upon the quality of the copy submitted.

In the unlikely event that the author did not send a complete manuscript
and there are missing pages, these will be noted. Also, if material had to be removed,
a note will indicate the deletion.


UMI 3631178

Published by ProQuest LLC (2014). Copyright in the Dissertation held by the Author.

Microform Edition © ProQuest LLC.
All rights reserved. This work is protected against
unauthorized copying under Title 17, United States Code


ProQuest LLC.
789 East Eisenhower Parkway
P.O. Box 1346
Ann Arbor, MI 48106 - 1346

**A FRAMEWORK OF INTEGRATED PRODUCT DESIGN AND CONTROL IN MANUFACTURING POLYMER NANOCOMPOSITES**

by

Qian Gou

Approved: _____
Abraham M. Lenhoff, Ph.D.
Chair of the Department of Chemical and Biomolecular Engineering

Approved: _____
Babatunde A. Ogunnaike, Ph.D.
Dean of the College of Engineering

Approved: _____
James G. Richards, Ph.D.
Vice Provost for Graduate and Professional Education

I certify that I have read this dissertation and that in my opinion it meets the academic and professional standard required by the University as a dissertation for the degree of Doctor of Philosophy.

Signed: _____

Babatunde A. Ogunnaike, Ph.D.
Professor in charge of dissertation

I certify that I have read this dissertation and that in my opinion it meets the academic and professional standard required by the University as a dissertation for the degree of Doctor of Philosophy.

Signed: _____

Mark D. Wetzel, M.S.E.E.
Member of dissertation committee

I certify that I have read this dissertation and that in my opinion it meets the academic and professional standard required by the University as a dissertation for the degree of Doctor of Philosophy.

Signed: _____

Antony N. Beris, Ph.D.
Member of dissertation committee

I certify that I have read this dissertation and that in my opinion it meets the academic and professional standard required by the University as a dissertation for the degree of Doctor of Philosophy.

Signed: _____

Thomas H. Epps, III, Ph.D.
Member of dissertation committee

## ACKNOWLEDGMENTS

First and foremost, I want to give my thanks to my thesis advisors, Prof. Babatunde A. Ogunnaike and Mr. Mark D. Wetzel for their great support and mentorship to me during the past five years of Ph.D. study. I feel really grateful about their generous help and invaluable advice whenever I met difficulties in my researches. I feel really appreciated for their constant encouragement of expressing my own ideas. All of these helped me to develop as an independent researcher and made my Ph.D. project meaningful. In addition, I want to give my thanks to the other committee members, Prof. Antony N. Beris and Prof. Thomas H. Epps, for their advice and technical input on my project.

I want to give my thanks to the polymerase processing group in DuPont, especially Ray Pettitt for the experiments on twin screw extruder, Fred Best for training on the micro compounder, and Christopher Chan for preparing the transmission election microscopy grid. Also, I want to thank Robert A. Lewis, Timothy J. Wright, Susan Latimer and other folks in the Experimental Station.

Besides, I want to thank all of Ogunnaike research group members both past and present that supported all through my Ph.D. studies. I want to thank the past group members, Dr. St. Amand, Dr. McGill, Dr. Chung, Dr. McDonald, especially Dr. Detroja for his excellent previous researches conducted on the part of customer feedback, which shed great light on my thesis research. I want to thank all of my present research group members, Dan Cook, Robert Lovelett, James Park, Devesh Radhakrishnan, Chia-Hung Tsai, and Zack Whiteman for their friendship and their

exchange of interesting research ideas. Also, I want to thank the visiting scholar, Prof. Wang, from my undergraduate university, for her help with the stability analysis.

I want to give my thanks to the Pochan research group in the Department of Material Science, especially Yingchao Chen for her work done on transmission election microscopy.

I want to thank my friends in University of Delaware and Newark, for their support and accompany throughout the five years, especially Weiting Yu.

I want to give my thanks to my parents, who have support me unconditionally all through my life. I also want to thank my sister and brother for their roles as family as well as friends.

## TABLE OF CONTENTS

## LIST OF TABLES

## LIST OF FIGURES

## ABSTRACT

Polymer nanocomposites are increasingly used across a variety of applications in the plastics sectors, especially in the packaging and automotive industries. The demand for nanocomposites in the U.S. is projected to exceed 7 billion pounds by 2020, and the production of nanocomposites is estimated to be near 10 billion pounds by 2025 [1]. The successful development and commercialization of these polymer nanocomposites requires an appropriate product design, followed by an efficient process for manufacturing the products to achieve desired end-use product performance consistently. While product design of nanocomposites has been receiving deserved attention, the equally important next step – a control scheme designed for ensuring that what the manufacturing process produces will perform as designed – has received little or even no attention. Since it is the customer that evaluates the product performance in end-use, the control strategy required for achieving the objectives of product design must extend well beyond the traditional control scheme of merely controlling process output variables and even beyond the product end-use characteristics control; it must *explicitly* incorporate customer feedback on the product performance, in order to ascertain consistent attainment of desired product end-use performance characteristics. However, this feedback is completely missing from the control schemes typically employed in manufacturing processes.

To address these challenging issues, we have proposed a framework for integrating product design with appropriate control strategies required for achieving acceptable product performance consistently. This framework is illustrated by

manufacturing polymer nanocomposites using extrusion processes. The major contributions of this dissertation include: (i) product design: the manufacturing material, consequent manufacturing process, and required operating conditions in manufacturing polymer nanocomposites were determined judiciously, (ii) quantification of clay dispersion in polymer nanocomposites: this novel method based on describing particle length distribution data from transmission electron microscopy micrographs with a gamma probability distribution model, $\gamma(\alpha, \beta)$, and an explicit quantitative relationship between these model parameters and the extent of dispersion was established successfully, and (iii) control scheme design and implementation: a multivariable cascade-type control scheme is designed, consisting of controller $C_1$ for controlling process outputs, controller $C_2$ for regulating the product end-use properties, and controller $C_3$ for improving customer satisfaction by using customer feedback data to calculate appropriate set-points for end-use properties. The controller $C_1$ and $C_2$ were designed as multiple-input multiple-output model predictive controllers (MIMO MPC), while controller $C_3$ was designed as an unconventional customer feedback controller utilizing customer feedback data to take rational corrective action if the product does not perform in end-use precisely as designed.

# Chapter 1

# INTRODUCTION

## 1.1 Overview of Polymer-Clay Nanocomposites

Polymer-clay nanocomposites are a class of polymer materials consisting of pristine polymer as polymer matrix and nanometer-sized fillers as reinforcement. Although a variety of nanoscale fillers have been used in the preparation of nanocomposites, layered silicate minerals (e.g., montmorillonite (MMT) clay) remain the most commonly used. The layered silicates involve individual clay layers (or platelet) with 1 nm thickness and a few angstroms to possibly microns in the lateral dimensions [2]. By dispersing these high aspect ratio clay layers in the polymer matrix, a significant enhancements of matrix properties can be achieved, e.g., superior stiffness and strength [3-5], enhanced gas barrier traits [6, 7], and increased flame retardancy [8, 9]. Remarkably, these property enhancements are able to be obtained at extremely low clay concentrations, i.e., 2-5 vol %, which is about four times lower than what is typically needed in conventional composites [4].

All these attractive properties of polymer nanocomposites suggest a variety of possible industrial applications, such as automotive, construction, aerospace, food packaging, and many others [10-13]. It is no wonder that the demand for nanocomposites in the U.S. will exceed 7 billion pounds by 2020 and the production of nanocomposites will be near 10 billion pounds by 2025 [1].

### 1.1.1 Clay Dispersion

In polymer-clay nanocomposites, the clay dispersion is defined as the clay structures in the polymer matrix. Depending on the degree of clay dispersion, polymer-clay nanocomposites are traditionally classified as: (i) immiscible – in which most clay platelets are packed together into structures often referred to as "tactoids", (ii) intercalated – in which clay platelets are partially stacked, and (iii) exfoliated/delaminated – in which individual clay platelets are well-dispersed in pristine polymer [14].

The key to achieving desired end-use properties is the level of clay exfoliation in the polymer matrix. However, due to the hydrophilic nature of the clay, these clay platelets do not usually disperse in the hydrophobic polymers as individual platelets; instead, they tend to aggregate to form clay particles and tactoids. One of the most popular methods to make the clays more compatible with polymers is to modify the nano-fillers by exchanging the cation in the clay with alkyl ammonium ions to form a swollen hybrid structure, termed "organoclay". Although a considerable amount of studies has been carried out to determine the effects of the organoclay modifiers on the morphology and properties of nanocomposites based on a variety of polymer matrices [15-19], much less emphasis is placed upon the effects of processing conditions in the manufacturing process on the structure and properties of polymer nanocomposites.

### 1.1.2 Manufacturing Process

To date, there are three techniques for manufacturing polymer-clay nanocomposites: (i) *in situ* polymerization [6, 20], (ii) solvent blending [21, 22], and (iii) melt intercalation [19, 23-26]. Among them, melt intercalation is the most promising technique

that would greatly expand the commercial opportunities for nanocomposites technology because of its many advantages [27, 28]. This technique involves melt blending the polymer and the organoclay using conventional compounding devices such as extruders and mixers, which therefore requires very little additional capital investment. Also, it is environmentally benign because no solvent is required. Moreover, it shifts nanocomposite production downstream such that end-use manufacturers are able to enjoy many degrees of freedom regarding final product specifications (e.g., selection of polymer grade, choice of organoclay, level of reinforcement, etc.) [24]. As a result, the nanocomposites investigated in this research were prepared using extrusion process via melt intercalation technique, the details of which are presented in Chapter 3.

*Processing Conditions, Organoclay Dispersion, and Physical Properties*

Recent studies have demonstrated that, in addition to the polarity of the polymer and organic modification, processing conditions in the melt intercalation technique play a vital role in achieving high degree of clay dispersion which consequently affects the end-use properties of the materials [29, 30]. For example, Dennis *et al*. [31] reported that shear intensity and residence time in the extruder have significant effects on the clay exfoliation. Chavarria *et al*. [26] showed that the barrel temperature is a critical factor in exfoliating the clay platelets in the polymer matrix, while Besco *et al*. [32] reported that the level of dispersion is strongly influenced by the mixing protocol. Also, it should be noted that screw speed can either have a positive [31, 33-35] or a negative [36] effect on the exfoliation (see section 3.4 for a more extensive literature review on processing conditions).

Results from these and other similar studies provide following valuable insights regarding the effects of processing conditions on the level of organoclay dispersion:

1. The processing conditions need to be tailored for specific product applications to achieve high level dispersion of clay platelets, because the same effects of processing parameters on nanocomposite structure are not universally observed [37].

2. An optimal combination of polymer and organoclay chemistry, extrusion equipment, mixing protocol, and processing conditions (i.e., integrated product and process design) is required to facilitate clay dispersion in order to manufacture polymer nanocomposite product with attributes that meet end-use performance.

These insights indicate that, to achieve satisfactory product end-use performance in its specific application, a systematic product design involving process design is required.

## 1.2 Challenges in Ensuring Acceptable End-use Performance

After determining the optimal operating conditions via product design, the next step is to determine how to maintain these optimal conditions in the extrusion process in the presence of all sorts of variability. Traditionally, this step is done by regulating process variables in the extrusion process (e.g., die pressure, motor power, melt temperature, etc.). However, this basic control scheme of regulating process variables is not always effective to obtain products with desired end-use attributes, because these process variables are often not sufficiently good indicators of the product end-use attributes. More recently, Garge *et al.* [38, 39] proposed an inference-based control scheme that augments the basic control scheme, achieving end-use property control by manipulating the set-points for the process variables. The overall control scheme,

which involves a multivariable cascade control structure, has been demonstrated on an industrial pilot scale process. However, even a perfect implementation of such advanced cascade control schemes cannot guarantee actual product performance.

Since it is the customer that assesses the product in its end-use, the product end-use performance is ultimately determined by the end-use customer. Therefore, the feedback information from the end-use customer is the most direct indicator of product end-use performance, and such information should be *explicitly* incorporated into the overall control scheme for ensuring consistent attainment of desired end-use performance. Especially with tailor-made products designed for specific performance, consistently meeting customer demands requires a comprehensive control scheme that will take *actual* product performance in end-use explicitly into consideration. As with standard feedback control where actual measurements of desired process outputs are used to adjust process inputs, it is necessary, under such a scheme, to obtain customer feedback on product performance and employ such information directly to take rational corrective action if the product does not perform in end-use precisely as designed. Designing such a control scheme is very challenging because of the intrinsic characteristics of the customer feedback information. Currently, such a control scheme does not exist.

## 1.3 Overview of Integrated Product Design and Control

To address the aforementioned challenges, we proposed in this thesis a framework that integrates product design with appropriate control strategies that explicitly incorporate customer feedback information for ensuring product end-use performance in a consistent manner. Such a framework was developed and

implemented for an example extrusion process of manufacturing polymer nanocomposites for a specific application.

This framework, aiming to guarantee acceptable product end-use performance, involves two important components: (i) product design, and (ii) control scheme design and implementation.

According to the customer needs for a specific application, a systematic product design first needs to be performed for translating such customer needs into desired product characteristics, following which a process must be designed and operated at desired conditions to deliver satisfactory products. Therefore, the primary objective of product design is to determine manufacturing materials, consequent manufacturing process, and required operating conditions.

Next, a comprehensive control scheme is developed for maintaining these operating conditions and manufacturing acceptable products consistently. Such a control scheme involves multiple, cascading control levels to incorporate end-use property control and customer feedback information. To facilitate the on-line control of infrequently measured end-use properties, this control scheme should employ inference models for predicting these variables at a sufficiently fast rate. Since the end-use properties of polymer nanocomposites are most directly related to the level of clay dispersion, developing such inference models requires an effective means for quantifying clay dispersion. Therefore, a quantification method of clay dispersion is also emphasized in this thesis.

## 1.4 Organization of Dissertation

This dissertation is organized as follows: Chapter 2 focuses on the current state of the art of manufacturing polymer nanocomposites and the main challenges in the control of extrusion processes. Also, the overall control scheme involving end-use property control and customer feedback information is introduced for assuring acceptable product end-use performance.

Chapter 3 concentrates on the systematic product design for an illustrative example of manufacturing polymer nanocomposites for a specific application. The manufacturing materials, consequent manufacturing process, and operating conditions are tailored for this specific application.

Chapter 4 proposes a quantification method to describing the level of clay dispersion explicitly. This method is further confirmed by in-house experimental data.

Chapter 5 discusses the model predictive control of the process output variables. This basic control scheme is implemented first in simulation environment, and then in real-time. Both servo and regulatory performances of this controller are covered in this chapter.

Chapter 6 augments the basic control scheme in Chapter 5 with a higher-level control scheme to regulate end-use properties. A multiple-input multiple-output model predictive control is designed for this purpose.

Chapter 7 presents the design and implementation of a novel controller – customer feedback controller. This chapter also involves a simulation case study to illustrate the performance of the controller.

Finally, the major conclusions of this work are summarized in Chapter 8, and directions for future research are presented.

# Chapter 2

# INTEGRATED PRODUCT DESIGN AND CONTROL

## 2.1 Chapter Organization

In this chapter, we discuss the important issues related to integrating product design and control in manufacturing nanocomposites by melt intercalation technique. In section 2.2, the current state of the art in manufacturing nanocomposites is presented, with a focus on the factors affecting the clay dispersion using melt intercalation technique. Before analyzing the relevant control issues of the manufacturing process (i.e., an extrusion process), a fundamental understanding of a typical extrusion process is provided in section 2.3. Next, a literature review on the modeling and control of extruders is discussed extensively in section 2.4.1, and associated control challenges are summarized in section 2.4.2. Then, in section 2.5, we introduce the overall framework for integrating product design and control in manufacturing nanocomposites with an emphasis on the comprehensive control scheme development for guaranteeing acceptable product end-use performance. Finally, the illustrative example of manufacturing nanocomposites for a specific application is briefly discussed in section 2.6.

## 2.2 Current State of the Art in Manufacturing Nanocomposites Using Melt Intercalation Technique

The melt intercalation technique involves thermal annealing, statically or under shear, a mixture of the polymer matrix and organoclays above the softening point of

the polymer in the polymer melt [40]. Several factors affect the level of clay dispersion of polymer nanocomposites prepared using the melt intercalation technique, and these factors are discussed in detail below.

*The effect of polymer matrix*: Since the presence of polar type interactions between the polymer and layered silicates is critical to form exfoliated nanocomposites, polar polymers are more favorable for the intercalation of polymer chains into the silicate galleries [27, 41]. For example, for a relative polar polymer such as nylon 6 [42], almost fully exfoliated nanocomposites were obtained using melt mixing method, while for non-polar polymers such polyolefins, it is common to improve the polyolefin-organoclay compatibility by copolymerization of the olefin monomer with a polar monomer like acrylic acid [43] or vinyl acetate [44, 45], which enhances the mechanical properties of the resulting nanocomposites in turn.

*The effect of the organic modification of layered clays*: As mentioned in section 1.1.1, the original clays are often modified by organic surfactants to improve the compatibility between the polymer matrix and the clays. As a result, the type of surfactants plays an important role for organoclay dispersion in the polymer matrix. For nylon 6, the surfactants that have only one alkyl tail give better exfoliation than those with two alkyl tails [15], whereas for poly(ethylene-*co*-methacrylic acid) ionomers, surfactants with longer alkyl tails are better at exfoliating the organoclays than those with a shorter alkyl tails [19].

*The effect of melting process equipment and mixing protocol*: One advantage of melt intercalation technique is that it is compatible with conventional polymer processing equipment (e.g., extruders, mixers, etc.), among which co-rotating, intermeshing twin screw extruders have proven to be the most effective for exfoliation

of organoclays [25]. The mixing protocol is another factor that influences the clay particle dispersion. Specifically, the more the number of passes goes through the mixing equipment, the better the organoclay dispersion can be obtained [26].

*The effect of processing conditions*: As already discussed in section 1.1.2, for the extrusion process, operating conditions such as screw speed, residence time, and melt temperature strongly affect the clay structures in the polymer matrix [29-31]. Also, there appears to be an optimal combination of processing conditions for a specific polymer nanocomposite system.

Therefore, to design a polymer nanocomposite product for a specific end-use application, it is necessary to take these factors into consideration in order to make a rational choice of polymer matrix, organoclay type, processing equipment, mixing protocol, and processing conditions – the concept of "product design".

Although the product design of polymer nanocomposites has been extensively studied, the equally important next step – designing a control scheme to ensure that manufactured nanocomposite products perform as designed – has received little or no attention. Since customers are primarily concerned with product attributes and especially with product performance in an end-use application, the control strategy required for achieving the objectives of product design must extend well beyond the traditional practice of merely regulating process output variables and even beyond the product end-use property control; it must explicitly incorporate customer feedback to ascertain consistent attainment of desired product end-use performance characteristics. However, to the best of our knowledge, no work has been done on the design and implementation of such a control scheme for effective control of end-use characteristics, consistently to target, in the manufacture of polymer nanocomposites.

## 2.3 Extrusion Process Description

Before analyzing the relevant control issues of an extrusion process for manufacturing nanocomposites, it is important to have a fundamental understanding of the process itself. Extrusion is a continuous process in which materials are mixed, modified or transformed. A typical extrusion process is shown in Figure 2-1 and is described in detail as follows: the raw materials are fed into the extruder through the hoppers. Usually, more than one feed can be charged from different hoppers to maintain a certain feed composition. Then, the feed is transported from the hopper to the die by the force generated by the screw rotation and friction. At the die exit, extruded strands at steady-state extrusion condition are immediately quenched in water and then pelletized [46].

In the remaining part of this section, we discuss the key characteristics of the extruder screw, types of screw extruders that are typically used in manufacturing nanocomposites, and the process analysis of the extrusion process.

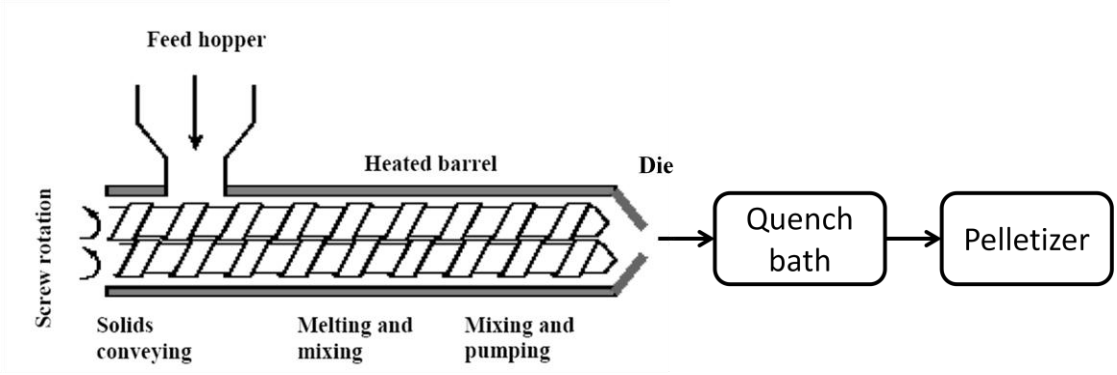


Figure 2-1: Schematic diagram of a extrusion process [47]

### 2.3.1 Extruder Screw Characteristics

The rotating screw, a key component of the extrusion process, forces the feed forward into the barrel and the solid feed is melted as it travels along the heated barrel. Most screws have the following functional zones: a solids conveying zone, a melting section, one or more mixing sections, and a pumping zone. At the conveying zone, the feed materials are almost solid, while they become partially melted as they are transported from the conveying zone to the melting zone where a number of processes such as mixing and reaction may take place [48]. The feed materials are essentially considered a complete melt in the mixing and pumping zone and are ready to be extruded through the die.

The screw design is critical for efficient melting of the materials and for decreasing the impact of process disturbances during operation. A typical screw design incorporates several types of screw elements such as a conveying element for direct flow (positive helix angle), a screw element for reverse flow (negative helix angle), and a kneading block (staggered disks providing shear and extensional flows for melting and mixing). By appropriately configuring these screw elements, it is possible to compose an efficient screw design to fit the specific application.

The geometry of an extruder screw, which was fully studied by Booy [49] and Potente *et al.* [50], also plays a key role in the compounding process in the extruder. The key screw parameters describing the geometry of the extruder screw are presented in Figure 2-2. Of these, some screw parameters are discussed as follows [51]:

- Channel depth ($H$): This variable generally decreases along the transition section, and it has the largest value in the mixing and pumping zone. This design allows more work to the polymer feed and therefore provides stable and consistent material feed-rate to the die channel.

- Pitch ($C$): This parameter is directly related to the screw helix angle ($\phi$). Usually, the optimal pitch is obtained based on the rheological properties of the polymer feed.

- Length-over-diameter ($L/D$) ratio: Since higher $L/D$ ratio leads to more homogenized melt and a higher production rate, high $L/D$ ratio is desirable in most cases. Just as selecting the extruder size and drive combination, the $L/D$ ratio should be carefully evaluated according the materials being processed. Especially for a polymer that melts easily, a longer $L/D$ extruders can actually penalize overall performance [52].

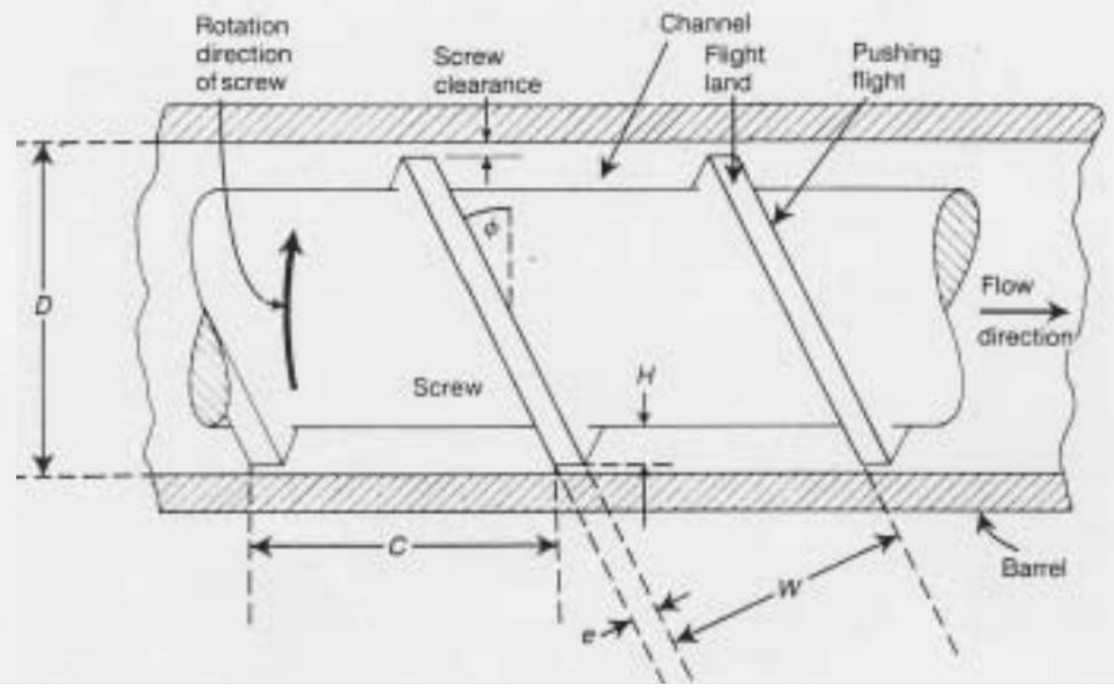


Figure 2-2: The key screw parameters: Barrel diameter ($D$), Helix angle ($\phi$), Flight Width ($W$), Channel depth ($H$), Pitch ($C$), and Tip width ($e$) [53]

### 2.3.2 Classification of Extruder Types

Generally, the screw extruders can be divided into two main categories: the single screw extruder (SSE) and the twin screw extruder (TSE). The major difference between single and twin screw extruders is the conveying mechanism: in the single screw extruder, the materials are conveyed due to their friction with the channel walls, while in the twin screw extruder, the twin screw rotation forces the materials forward, making the conveying behavior less dependent on the friction [54]. The twin screw extruder enjoys several advantages over the single screw extruder. For example, the twin screw extruder offers better mixing and superior control over residence time. Moreover, the flexibility of twin screw extrusion equipment allows this operation to serve more specific processing requirements [55, 56]. Therefore, the twin screw extruder has been found to be more suitable for manufacturing nanocomposites using the melt intercalation technique [31].

According to the direction of rotation and engagement of the screw, twin screw extruders can be categorized as follows:

- Direction of rotation: The extrusion machine is termed as a counter-rotating extruder if the two screws have the opposite direction of rotation, while it is known as co-rotation extruder when the two screws rotate in the same direction. Since co-rotating extruders provide better mixing and heating, they are more effective than the counter-rotating counterparts for favoring organoclay dispersion [57].

- Interpenetration: Twin screw extruders are classified as intermeshing or non-intermeshing. Intermeshing TSEs are extruders where the flights of one screw protrude into the channel of the other screw. Therefore, these extruders provide positive conveying, extensional flows and back mixing, which facilitate the clay dispersion in the polymer matrix.

### 2.3.3 Process Variables and Product Properties

In this section, we discuss the variables associated with control of the extrusion process. According to their measurement frequency, these variables, involving process variables and product properties, can be classified as follows:

1. Process variables: These variables are often measured online, with the measurement rate being of the order of seconds and available without any delay. Usually, they are divided into process input/manipulated variables, $u$, (e.g., screw speed, feed-rates, composition, and barrel temperature), and process output variables, $y$, (e.g., die pressure, motor power, and melt temperature).

2. Product quality variables: These variables, $q$, (e.g., melt index, molecular weight, clay dispersion, and viscosity), are often not measured online and are available after a delayed laboratory analysis (a few minutes to an hour). A number of techniques have been employed to predict the product quality variables from available process variables [58-61].

3. End-use property variables: The measurements of these variables, $w$, (e.g., modulus, toughness, tear strength, and gas barrier properties), are obtained after every few hours or one day. Only a few studies predicted these property variables by inferential models [62].

4. Customer feedback variable: The customer feedback information, $z$, is often received from the end-use customers after a few days or even months. Note that this variable is a binary variable: customers either accept the product, $z = 1$, or decline it, $z = 0$. Although this variable is vital to assure acceptable end-use product performance, it is completely missing from current control schemes.

Selection of process manipulated variables and process controlled variables is required for the proper design of traditional control system (process control). As discussed by Seborg et al. [63], one of the criteria for selecting process input variables is that the barrel temperature is the least suitable manipulated variable because of the slow speed of correction. Further, the selection of process output variables is usually based on the control objectives. Note that the process output variables can be used as

controlled variables for product property control. Such process output variables needs to be identified judiciously based on their influence on the product property characteristics.

## 2.4 Control of Extrusion Processes

In this section, modeling and control of extrusion processes (especially twin screw extruder) are reviewed with a focus on polymer extrusion processes. Then, the challenges associated with the control of these processes are discussed.

### 2.4.1 Literature Review

Extrusion is a complex process and highly affected by unmeasured disturbances. Any disturbance in process variables can cause variations in end-use properties of the final product; therefore, understanding the types of disturbances is essential to the effective control of these properties. In general, the disturbances associated with an extrusion process can be classified as:

1. Fluctuation: This kind of disturbances is mainly caused by the rotation of the twin screws in the barrel and the rotations of the feeder screws [64]. The fluctuations are the dominant disturbances affecting the extrusion process [65], which may lead to undesired product properties.

2. Bulk density: This disturbance occurs at the feed end because of compositional and property variations in the polymer feed [66]. These disturbances often result in undesirable variability in product end-use properties. To reduce the effect of this disturbance, feed-rates can be used as the manipulated variables.

3. Die resistance: These disturbances, often occurring during start-up or after step changes in operating conditions, result from abrupt changes in die resistance. This type of disturbances also contributes to variations in product properties [66].

To ensure acceptable product properties consistently and effectively in the presences of disturbances, it is necessary to understand the process of interest. Therefore, developing a good mathematical model for the extrusion process is extremely important, which is also a prerequisite for controller design [67]. In this respect, three main modeling approaches are employed and discussed as follows.

*First-principles or mechanistic approach*: This approach requires *à-priori* knowledge of the process, such as physical, chemical and other mechanistic knowledge. However, in most cases, the process physics for an extrusion process is either unknown or not well defined, which makes it difficult to build reasonably accurate process models by this approach. Moreover, these models, consisting of a set of coupled nonlinear equations (see, for example, Zagal *et al.* [68] and Choulak *et al.* [69]), are usually computationally intensive to solve on-line, which makes it difficult to employ them for on-line control.

*Empirical approach*: This approach employs input-output data to develop linear correlations. Since the input-output data are obtained entirely from process system identification, the key of this approach is the design of input excitations used to generate the output responses. Traditionally, step changes in input variables are employed to excite the process [70, 71]; however, the resulting models can only capture the low frequency process characteristics. A different type of input signal, named PRBS (pseudo-random-binary-sequence) signal, has been designed to excite the process at both low and high frequencies (see, for example, Iqbal *et al.* [72] and Trifkovic *et al.* [73]).

*Grey-box or hybrid approach*: This approach combines both mechanistic and empirical methods. For example, Garge *et al.* [62] discussed the development of a hybrid

model for predicting key product properties such as tensile strength and toughness using pulse perturbation technique to generate the data. In another study, Iqbal *et al*. [65] developed a gray box model for a twin screw extruder to predict the melt temperature and die pressure, where the model parameters were estimated from the input-output data obtained by exciting the system using by PRBS signals. This approach also needs some mechanistic information of the process, and how to combine such information and process data depends on the extrusion process under consideration.

Very limited work has been done for effective control of polymer extrusion processes, and Table 2-1 presents a summary of current efforts towards on-line control of these processes. The literature review reveals the following insights regarding the control of polymer extrusion processes:

1. The most popular control scheme for extrusion processes is model predictive control (MPC). Some researchers designed multiple-input multiple-output (MIMO) MPC to realize multivariate control of twin screw polymer extrusion processes.

2. Most researchers employed the single loop control scheme for the regulation of product viscosity and molecular weight. One notable exception was Garge *et al.* [39], who designed and implemented a cascade multivariate control strategy for controlling product end-use properties.

3. To the best of our knowledge, no studies have been carried out on control paradigms for ascertaining acceptable product end-use performance in the manufacture of polymer nanocomposites.

The modeling and control of food extrusion processes are not included in this literature review, because (1) models of food extrusion processes hardly provide insights into the understanding of the polymer extrusion processes since plastic has complex rheology while food does not, and (2) food extrusion processes have completely different process characteristics and control objectives.

Table 2-1: Comparative study of different approaches to control twin screw extrusion processes

| References | Control scheme [a] | Manipulated variables [b] | Controlled variables [c] | Polymers [d] |
|---|---|---|---|---|
| Ozbek *et al.* [74] | MPC | SS | $M_v$ | PET |
| Trifkovic *et al.* [75] | MIMO MPC | WT, SS | ML, MT | TPV |
| Garge *et al.* [39] | Cascade MIMO MPC | SS, FR | IL: DP, MP, WF OL: $\eta$, TS, T | EBAGMA, EMAA |
| Broadhead *et al.* [76] | PI, MV | FR | $\eta$ | EMMA, I |

[a] Model predictive control (MPC), multiple-input multiple-output (MIMO), proportional integral (PI), minimum variance (MV)

[b] Screw speed (SS), WT (wall temperature), FR (feed rate)

[c] Molecular weight ($M_v$), motor load (ML), melt temperature (MT), die pressure (DP), motor power (MP), weight fraction (WF), viscosity ($\eta$), inner loop (IL), outer loop (OL), tensile strength (TS), toughness (T)

[d] Poly(ethylene-terephthalate) (PET), thermoplastic vulcanizate (TPV), poly(ethylene-butyl acrylate-glycidal methacrylate) (EBAGMA), poly(ethylene-*co*-methacrylic acid) (EMAA), sodium ionomer of poly(ethylene-*co*-methacrylic acid) (I)

### 2.4.2 Challenges in the Control of Extrusion Processes

The literature review reveals the following challenges with regard to the control of extrusion processes:

1. Extrusion is complex process with a variety of disturbances affecting the process variables, which in turn influence the product properties of the final product. Therefore, an adequate model is necessary for effective control of such a complex process.

2. These processes are inherently multivariable and the process variables are highly interacting. Thus, multiple-input multiple-output model predictive control (MIMO MPC) is a better choice compared to traditional control schemes.

3. It is difficult to guarantee acceptable product end-use performance even with good regulation of process variables (e.g., die pressure, motor power, etc.), product quality variables (e.g., viscosity, molecular weight, etc.), and end-use properties (e.g., tensile strength, toughness, etc.). As a result, customer feedback has to be incorporated in any cascade control scheme designed for controlling product properties. Since this variable is binary in nature, it is extremely difficult to model it with continuous product properties. Therefore, current control schemes do not incorporate customer feedback information.

## 2.5 Proposed Framework

To address these challenges, we have developed a framework for integrating product design with the appropriate control strategies required to achieve the target end-use characteristics consistently in the manufactured product. This framework is developed for general designed products, using polymer nanocomposites as a focusing problem.

In product design, a specific type of polymer nanocomposites is designed according to the tailored application. Then, the appropriate equipment is selected to

manufacture the product (e.g., extruders), following which the operating conditions are optimized to achieve the end-use property specifications.

Then, an appropriate control scheme needs to be designed to achieve the acceptable end-use performance consistently in the polymer nanocomposite product. Such a control scheme is responsible not only for regulating the process output variables and end-use properties, but also for incorporating customer feedback information, $z$, to guarantee acceptable end-use performance.

To achieve these objectives, we propose a multivariable, cascade structure for the extrusion process shown in Figure 2-3, consisting of controllers at three levels: controller $C_1$ for regulating the process output variables by adjusting process manipulated variables, controller $C_2$ for controlling the end-use properties by manipulating the process output variables, and controller $C_3$ for improving the product end-use performance by regulating the set-points of the end-use properties using customer feedback information. Besides these controllers, the controller set $C_0$ (not shown explicitly), mostly as single loop proportional-integral (PI) controllers, includes the regulatory controllers for implementing basic control in the manipulated variables. While controllers $C_1$ and $C_2$ are designed as multiple-input multiple-output model-based controllers, the controller $C_3$ is going to be an unconventional controller because of the binary nature of customer feedback information.

To compensate the infrequent measurements of end-use properties, inference models are necessary for predicting these variables at a sufficiently fast rate. For polymer nanocomposite materials, the level of clay dispersion is the most direct indicator of the end-use properties. Thus, developing such inference models requires an effective means for quantifying clay dispersion. Such a quantification method of

clay dispersion is proposed and validated in this thesis (see Chapter 4), while the development and implementation of these inference models are reserved for future work (see Chapter 8).

In addition to inference models, models for designing the above-mentioned controllers are also required and involve the following models: (i) $M_{uy}$ – a model that links the manipulated variables, $u$, to process output variables, $y$, (ii) $M_{yw}$ – a model relating the process output variables, $y$, to end-use properties, $w$, and (iii) $M_{wz}$ – relating the end-use properties, $w$, to the customer feedback information, $z$. Of these, the model $M_{uy}$, as an indispensable component of model predictive control, has been discussed extensively [65, 68, 69, 72, 73, 77]; the models $M_{yw}$ and $M_{wz}$, on the other hand, are rarely discussed, not to mention incorporated in control schemes. Besides, the model $M_{wz}$ needs to be developed using nontraditional modeling methods because end-use properties are continuous while the customer feedback data are binary.

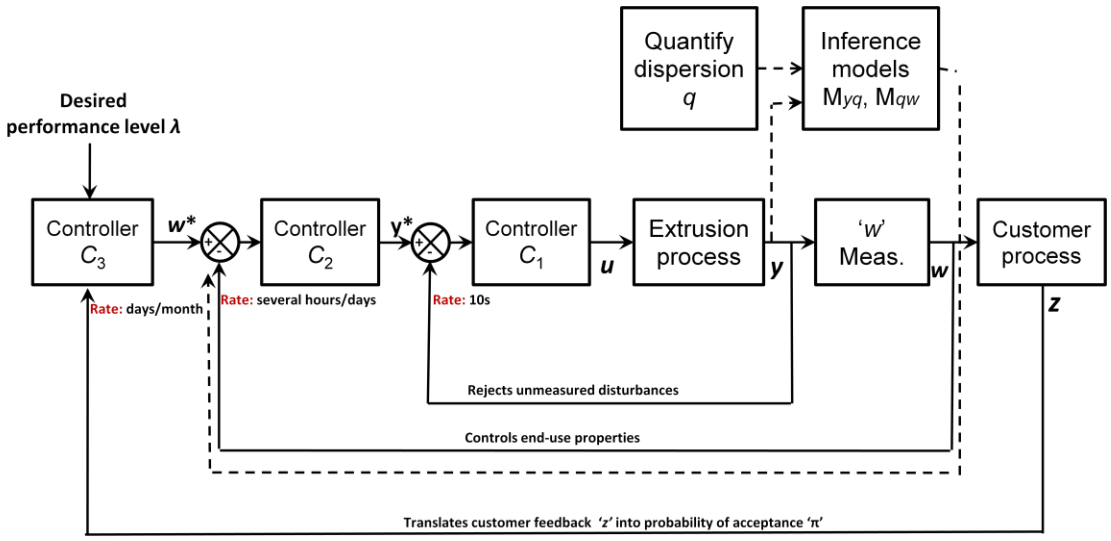


Figure 2-3: Proposed structure for end-use property control of an extrusion process for manufacturing polymer nanocomposites (explicitly incorporating customer feedback) showing nested multivariable, multiple-rate feedback loops

## 2.6 Example Application of Polymer Nanocomposites

The proposed framework is illustrated by manufacturing polymer nanocomposites using extrusion processes for packaging films. Specifically, the niche application is the packaging of cereals and cookies/crackers.

Based on this tailored application, a polymer nanocomposite system will be designed, following which the appropriate processing protocol and corresponding extrusion equipment will be determined. Then, the operating conditions required to achieve desired end-use performance are determined in a systematic way. These major components in product design will be discussed in detail in Chapter 3.

Next, the proposed multivariable, multiple-rate control scheme is used to manufacture the designed polymer nanocomposites in order to achieve the customer's requirement consistently. The design and implementation of the three controllers are detailed in Chapter 5, Chapter 6, and Chapter 7.

## 2.7 Conclusions

In this chapter, we have laid the foundation for the remaining part of the thesis. We first reviewed the current state of the art in manufacturing polymer nanocomposites based on extrusion processes. Then, we presented a fundamental description of the extrusion processes. Further, a literature review on the control of extruders was discussed extensively, and the challenges associated with the control of extrusion processes were presented. These challenges are addressed by the proposed framework of integrated product design and appropriate control strategies for assuring acceptable product performance, which is the essence of this thesis. Finally, we introduced the example application of polymer nanocomposites, based on which the

development and implementation of the proposed framework are illustrated in the following chapters.

# Chapter 3

# SYSTEMATIC PRODUCT DESIGN OF POLYMER NANOCOMPOSITES

## 3.1 Introduction

To manufacture tailor-made products designed for a specific application, it is necessary first to go through "product design". As discussed in Chapter 1, the primary objective of product design is to determine manufacturing material, consequent manufacturing process, and required operating conditions. Therefore, a systematic product design involves three steps: (i) translating customer needs for a specific application (e.g., packaging films in our case) into a particular type of polymer nanocomposites, (ii) choosing an appropriate manufacturing process to produce the material determined in step one, and (iii) determining required melt processing conditions to achieve customer's specifications and high level of clay dispersion. Since the dispersion is the key factor to achieving desired product performance, it is imperative to identify critical factors that strongly affect clay dispersion, which is another step included in product design. In sections 3.2 through 3.5, we discuss these steps of product design and illustrate these steps via our specific application on packaging films.

The next step is to design an appropriate control scheme to maintain the melt processing conditions and control the dispersion via identified critical factors. However, before analyzing the relevant control issues, it is useful to understand the selected manufacturing process. Section 3.6 provides the necessary insight into the specific manufacturing process chosen in section 3.3.

## 3.2 Product Specification

The manufacturing material is determined according to customer's needs for a specific application. In this illustrative example, the manufacturing material is to be used in packaging films; the required product attributes are therefore enhanced mechanical properties, good clarity, and improved barrier properties. To fulfill required attributes, polymer-clay nanocomposites based on a structurally modified copolymer of polyethylene, Surlyn® 8945 (sodium ionomer of poly(ethylene-*co*-methacrylic acid) (Na ionomer)), were selected as the manufacturing materials, as this type of materials offers significant improvements in both barrier properties and mechanical properties by addition of low concentration of clays [78]. We chose an organically modified MMT, Cloisite® 20A, modified by quaternary ammonium salt was chosen as the reinforcement since it demonstrates the best ability to improve the clay dispersion in the Na ionomer [19].

## 3.3 Melt Mixing Masterbatch Process

The melt intercalation technique was employed to manufacture the polymer nanocomposites for achieving good clay dispersion (see Chapter 1). This technique includes dispersing organoclays directly in the polymer matrix via mixing equipments and can be applied through many different methods. There are two key issues related to this technique: the selection of appropriate mixing equipments and the determination of a mixing protocol.

In melt intercalation technique, nanocomposites have been formed using a variety of polymer processing equipments, such as the single-screw extruder [79, 80], the twin screw extruder [81, 82], the twin-screw microextruder [83, 84], and batch mixers [28, 85].

Since the twin screw extruder (TSE) has proven to be the most effective for facilitating the clay dispersion [5, 24], it is ideal for preparing polymer nanocomposites.

Typically, two mixing protocols that can be used to prepare the nanocomposites: a direct mixing method (one-step mixing) and a masterbatch method (two-step mixing). In the direct mixing method, polymer and clay are dry-premixed or separately fed to the mixing equipment in the desired amounts to obtain desired clay concentration, while in the two-step masterbatch method, clay-rich masterbatches are first prepared in one mixing unit and then diluted with the polymer melt to desired clay concentration in another unit. Since increasing the number of passes through the mixing equipment leads to higher clay particle dispersion [26], the two-step masterbatch method, which introduces two passes, is more effective than the one-step mixing method [29, 86, 87].

Therefore, we employed a TSE to perform the melt mixing masterbatch process, which includes the following steps: Initially, masterbatches containing 25 wt. % organoclay were prepared by melt blending in a co-rotating, intermeshing TSE to achieve good organoclay dispersion in the masterbatches; subsequently, the clay-rich masterbatches and polymer pellets were dried in a vacuum oven at 65 °C for a minimum 48 hours. This is followed by a dilution step where Na ionomer is added to the clay-rich masterbatch in a twin-screw microextruder (15-mL micro compounder, DSM Xplore®, DSM Research, Geleen, The Netherlands (DSM)) to achieve a desired concentration.

After the DSM batch process, the materials were injection molded using a DSM Xplore® 10-mL injection molding machine to obtain tensile bars (ASTM D 638, Type V). The melt temperature was the same as the temperature set in the

microextruder, and the mold temperature was 50 °C. The injection and holding pressures were set to 10 bars and 16 bars, while injection and holding times were 15 s and 60 s, respectively.

### 3.4 Process Design

Besides the properties of the polymer matrix, the organic modifier of the nanoclays, and the mixing method/equipment, the processing conditions have been reported to have important effects on the dispersion of the organoclay. Currently, researchers are primarily concentrated on nanocomposites prepared by direct mixing method using equipment such as TSE and batch mixers. Several studies reported that processing parameters in the TSE process such as the residence time [26, 86, 88], screw speed [33, 34], and feed rate [33, 34], are significant on the exfoliation of organoclay, while processing temperature [5, 33], as long as it is within a certain range, does not affect the clay dispersion. Some researchers studied the processing conditions of batch mixers on the structure and properties of nanocomposites and found that mixing time [30, 35, 89, 90], temperature [30, 35, 89], screw speed [30, 35, 84, 90], and nanofiller amount [35, 89] strongly affect the clay particle dispersion. Some of these studies determined the optimal processing conditions that achieve significant improvements in mechanical properties of the product [30, 35, 89], using experimental design and empirical modeling.

Until recently, only a few researchers have attempted to explore the effects of processing conditions on clay dispersion in nanocomposites produced by the two-step masterbatch method. For example, Domenech *et al.* [91] prepared nanocomposites by twin screw extrusion using a pre-compounded masterbatches. However, they only studied the processing conditions in the dilution TSE process of the masterbatch method, which is essentially no different from the direct melting method by TSE.

Another group, Besco *et al.* [32], first prepared the masterbatches by TSE at two different screw speeds (i.e., high and low) and then diluted the masterbatches via two mixing units, a TSE and a single screw extruder, at high and low screw speeds. They found that a combination of masterbatches manufactured at high screw speeds and the dilution in TSE at high screw speeds leads to the best clay particle dispersion in the composites. However, this study neither considered the effect of feed rate nor provided optimal processing conditions with regards to desired mechanical properties.

In the remaining part of this section, we present a comprehensive study to evaluate the effects of processing conditions of both masterbatch process and dilution process on the clay dispersion. Also, the optimal processing conditions are determined to achieve high level of exfoliation as well as desired mechanical properties. The processing conditions of DSM dilution process were studied first due to the potential time and cost saving. Besides, the systematic process design of the DSM batch system will provide insights into process design for the TSE process.

### 3.4.1 Process Conditions of the DSM Micro Compounder

As mentioned earlier, the batch processing parameters potentially affecting the dispersion and mechanical properties are mixing time, temperature, and screw speed. Clay concentration is also expected to affect mechanical properties strongly [35, 89, 92]; for Na ionomer-based nanocomposites, increasing clay concentration can improve the stiffness/modulus but at a cost of sacrificing toughness/elongation [93]. Therefore, it is imperative to determine optimal combination of the processing parameters and clay concentration to achieve an acceptable manufactured product.

To this end, a systematic procedure based on the statistical design of experiments (DoE) was employed. Four factors (mixing time, screw speed,

temperature, and clay concentration) and two response variables (stiffness and toughness) were considered in the DoE. The stiffness and toughness were represented by 1% secant modulus and elongation at break, respectively, which were determined by testing the tensile bars on an Instron® universal test machine according to ASTM D 638. The crosshead speed was 0.51 cm/min, and five samples were tested for each state.

With four potential factors, a two-step DoE strategy was designed: (i) screening experiments were performed to determine which of the four variables are significant, and (ii) optimization studies were carried out to determine the optimal settings for the significant factors required to achieve the desired response variable levels (i.e., stiffness and toughness).

#### 3.4.1.1 Screening Experiment

A $2^{4-1}$, resolution IV fractional factorial design of experiment was employed for screening the four DSM factors to determine which ones have statistically significant effects on the responses. The experimental conditions (see Table 3-1) and the "high" and "low" values were carefully chosen to ensure chemical stability of polymers and organoclays. Two replicates were included for each condition to test the reproducibility of the process. Experimental sequence was randomized to minimize the sample preparation error.

Table 3-1: $2^{4-1}$ fractional factorial design of experiment for screening important DSM factors on secant modulus and elongation at break

| | DSM factors | | | | Measured responses | |
|---|---|---|---|---|---|---|
| State No. | Time (min) | Temp (°C) | Screw speed (rpm) | Clay conc. (wt. %) | Secant modulus (MPa) | Elongation (%) |
| 15 | 5 | 240 | 240 | 3 | 178.23 | 311.91 |
| 7 | 5 | 240 | 240 | 3 | 192.05 | 333.15 |
| 5 | 5 | 180 | 240 | 10 | 203.00 | 175.35 |
| 9 | 5 | 180 | 60 | 3 | 197.82 | 204.80 |
| 8 | 15 | 240 | 240 | 10 | 328.97 | 231.58 |
| 14 | 15 | 180 | 240 | 3 | 210.51 | 194.30 |
| 12 | 15 | 240 | 60 | 3 | 194.58 | 284.32 |
| 3 | 5 | 240 | 60 | 10 | 310.72 | 272.06 |
| 4 | 15 | 240 | 60 | 3 | 192.93 | 292.13 |
| 6 | 15 | 180 | 240 | 3 | 186.57 | 193.04 |
| 16 | 15 | 240 | 240 | 10 | 317.01 | 227.30 |
| 2 | 15 | 180 | 60 | 10 | 309.83 | 165.12 |
| 13 | 5 | 180 | 240 | 10 | 293.80 | 155.42 |
| 10 | 15 | 180 | 60 | 10 | 188.87 | 151.66 |
| 1 | 5 | 180 | 60 | 3 | 339.73 | 182.21 |
| 11 | 5 | 240 | 60 | 10 | 338.46 | 234.40 |

The statistical analysis performed via Minitab® (see Table 3-2) revealed that clay concentration has a statistically significant effect on the 1% secant modulus (stiffness), while three factors – mixing time, temperature, and clay concentration – have statistically significant effects on elongation at break (toughness); the interaction between mixing time and screw speed was significant in both responses.

Further investigation of the interaction term is required, since 2-way interactions are confounded with the other 2-way interactions in a resolution IV fractional factorial design [94]. The results show that screw speed has no significant effect on either response, which indicates that the significant interaction, initially identified as between residence time and screw speed, is actually between the other two factors, i.e., mixing time and temperature. Consequently, mixing time, temperature, and clay concentration were determined to have significant effects on stiffness and toughness, while screw speed had no significant effect on mechanical properties in the DSM dilution process.

Table 3-2: Screening test results for the effects of DSM factors on polymer nanocomposite mechanical properties. Factors with *p*-values less than 0.05 are considered significant at $\alpha = 0.05$ significance level (bold)

| | | *p*-values for secant modulus | *p*-values for elongation |
|---|---|---|---|
| Main effects | Time | 0.57 | **0.05** |
| | Screw speed | 0.58 | 0.54 |
| | Temp | 0.46 | **0.00** |
| | Clay conc | **0.02** | **0.00** |
| Interactions | Time and temp | 0.49 | 0.10 |
| | Time and screw speed | **0.05** | **0.05** |
| | Temp and screw speed | 0.58 | 0.91 |

*Discussion of Results*

To study how the DSM processing conditions affect the dispersion from a physical point of view, it is necessary to introduce the mechanism of the formation of nanocomposites in melt processing. As Dennis et al [31] proposed, two pathways are related to the formation of nanocomposites in melt processing: (i) large organoclay particles are broken up into dispersed stacks of tactoids and small stacks of platelets, and (ii) the polymer chains diffuses in the clay galleries (the space between platelets). Pathway one requires shear intensity, while pathway two is facilitated by mixing time and temperature. Therefore, the results of screening experiments, which show that screw speed does not have a significant effect on the mechanical properties, indicate that the dominant pathway in the dilution process is polymer diffusion (pathway (ii)), while the structures of clay platelets (pathway (i)) are mostly determined during the preparation of the masterbatches.

#### 3.4.1.2 Optimization Study

Based on the results of screening experiments, a response surface (face-centered cubic) experimental design was carried out to determine the optimal settings for the three significant factors for obtaining products with high secant modulus without sacrificing elongation at break. Specifically, the desired 1% secant modulus and elongation at break were set in the ranges of 225 – 230 MPa and 245 – 255 %, respectively. The experimental conditions investigated are provided in Table 3-3 with the screw speed set at 100 rpm for all conditions. The centerpoint run conditions were performed with six replicates to determine the reproducibility of the process. Additionally, a random experimental sequence was implemented to minimize sample preparation error.

Table 3-3: Face-centered response surface design of experiment for optimizing the screened DSM factors to achieve desired secant modulus and elongation at break

| State No. | Significant DSM factors | | | Measured responses | |
|---|---|---|---|---|---|
| | Time (min) | Temp (°C) | Clay conc. (wt. %) | Secant modulus (MPa) | Elongation (%) |
| 10 | 15 | 210 | 6.5 | 246.56 | 250.33 |
| 5 | 5 | 180 | 10.0 | 323.30 | 191.25 |
| 13 | 10 | 210 | 3.0 | 171.50 | 320.11 |
| 12 | 10 | 240 | 6.5 | 227.15 | 311.61 |
| 4 | 15 | 240 | 3.0 | 162.56 | 409.12 |
| 11 | 10 | 180 | 6.5 | 264.83 | 179.64 |
| 20 | 10 | 210 | 6.5 | 235.66 | 277.45 |
| 19 | 10 | 210 | 6.5 | 235.70 | 246.24 |
| 8 | 15 | 240 | 10.0 | 374.20 | 105.74 |
| 7 | 5 | 240 | 10.0 | 370.43 | 123.38 |
| 17 | 10 | 210 | 6.5 | 258.67 | 221.24 |
| 18 | 10 | 210 | 6.5 | 269.73 | 226.56 |
| 15 | 10 | 210 | 6.5 | 261.54 | 243.21 |
| 2 | 15 | 180 | 3.0 | 208.43 | 220.49 |
| 3 | 5 | 240 | 3.0 | 182.83 | 329.16 |
| 1 | 5 | 180 | 3.0 | 199.08 | 202.19 |
| 14 | 10 | 210 | 10.0 | 342.01 | 178.14 |
| 16 | 10 | 210 | 6.5 | 265.45 | 227.39 |
| 9 | 5 | 210 | 6.5 | 267.06 | 230.72 |
| 6 | 15 | 180 | 10.0 | 359.18 | 146.01 |

Using response surface methodology, it is possible to establish quantitative relationships between factors (i.e., significant DSM factors) and response variables (i.e., stiffness and toughness). In general, the model is a low-order polynomial, shown as follows:

$$y = \beta_0 + \sum \beta_i x_i + \sum \beta_{ii} x_i^2 + \sum \sum \beta_{ij} x_i x_j \qquad 3\text{-}1$$

where $y$ is the response, $x$ is the parameter, $\beta_0$ is a constant, $\beta_i$ is the coefficient of individual factors, $\beta_{ii}$ is the coefficient of squared factors, and $\beta_{ij}$ is the coefficient of interactions.

Based on the results shown in Table 3-3, regression analysis carried out using Minitab® was applied to determine the coefficients associated with each response. The results of analysis are presented in Table 3-4.

Table 3-4: Response surface experimental results: model coefficients for secant modulus and elongation at break as a function of residence time, temperature, and clay concentration

| Terms | | Model coefficient of secant modulus | Model coefficient of elongation |
|---|---|---|---|
| Linear terms | Time | 0.377 | 4.608 |
| | Temp | -0.330 | 7.763 |
| | Clay conc. | -21.427 | 102.014 |
| Square terms | Time × Time | 0.412 | -0.555 |
| | Temp × Temp | -0.001 | -0.010 |
| | Clay conc. × Clay conc. | 0.368 | -0.431 |
| Interaction terms | Time × Temp | -0.051 | 0.074 |
| | Time × Clay conc. | 0.361 | -1.151 |
| | Temp × Clay conc. | 0.148 | -0.504 |

With these models, contour plots for secant modulus and elongation at break were generated and are presented in Figures 3-1 and 3-2, respectively. A contour plot consists of a 2-dimentional collection of equipotential curves of $y$, as a function of two independent variables $x$. Therefore, these figures visualize how each response behaves with respect to two factors at a constant value of the third factor, and they also help to identify the optimal settings that achieve the desired values of the responses.

The contour plot for secant modulus, shown in Figure 3-1, presents nonlinear behavior in the mixing time versus temperature panel, suggesting that factor interaction is as important as individual variables for the secant modulus response.

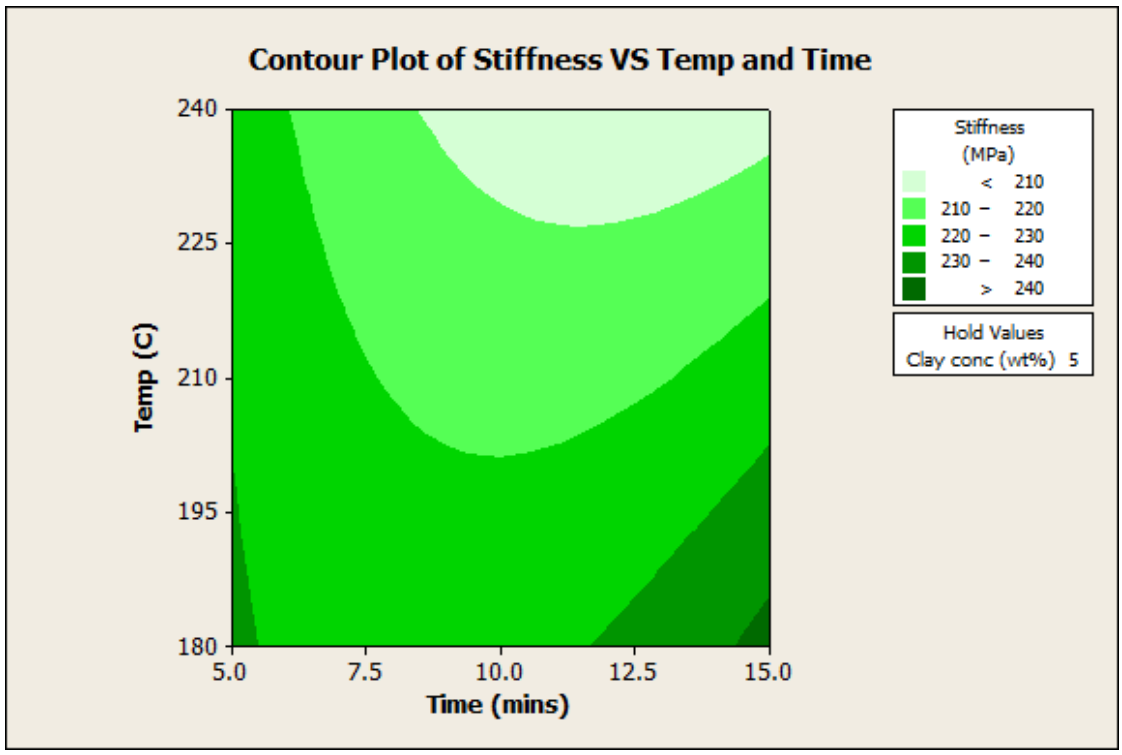


Figure 3-1: Contour plot for the stiffness (secant modulus) as a function of time and mixing temperature (with clay concentration held at 5 wt. %)

On the other hand, the contour plot for elongation at break, shown in Figure 3-2, suggests that elongation at break increases as the temperature increases, while it does not have significant change with increasing residence time.

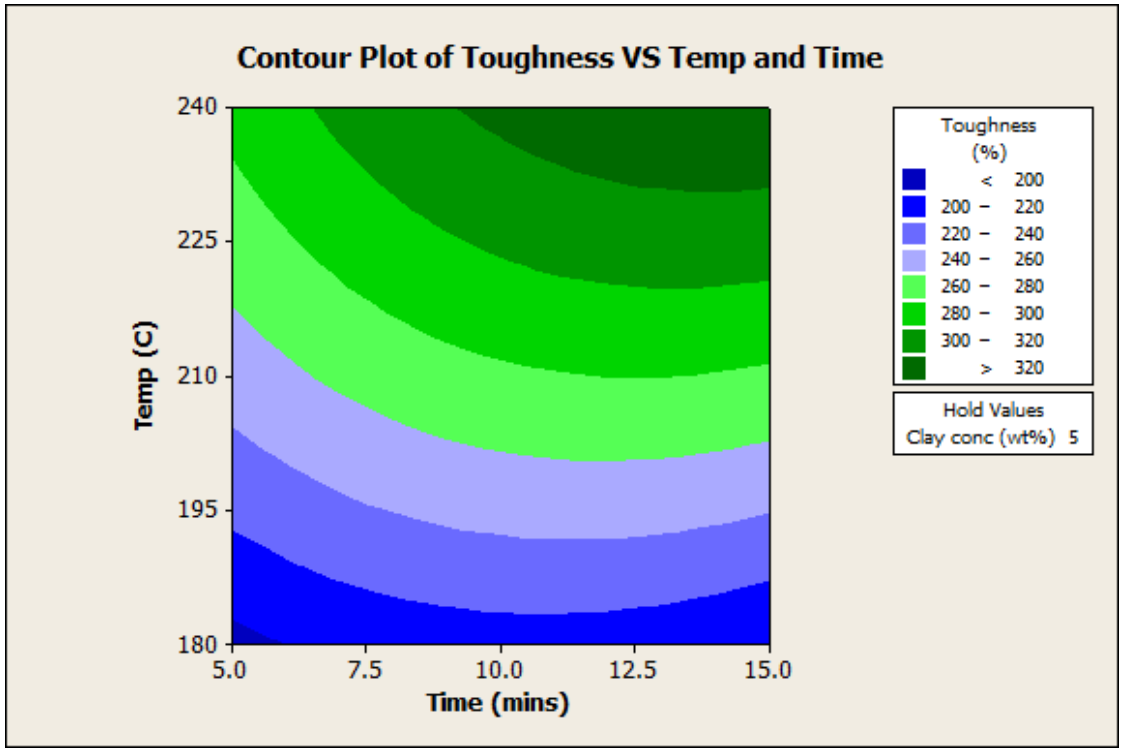


Figure 3-2: Contour plot for the toughness (elongation at break) as a function of time and mixing temperature (with clay concentration held at 5 wt. %)

Next, it is necessary to determine the optimal settings for achieving the desired property requirements. This was accomplished by overlaying the two contour plots for secant modulus (Figure 3-1) and elongation at break (Figure 3-2). The resulting overlaid contour plots are shown in Figure 3-3. Feasible regions occur where the objectives are met simultaneously in the overlaid contour plots. Given the desired values for secant modulus (225 – 230 MPa, shown in red lines) and elongation at break (245 – 255 %, shown in green lines), the feasible regions are represented as the white regions in Figure 3-3. The optimal clay concentration for this system is approximately 5 wt. %, which is consistent with Wetzel's report [93].

These results lead to the following conclusion: The optimal settings for the DSM processing conditions and clay concentration for obtaining product with desired stiffness and toughness are a screw speed of 100 rpm, a mixing time of 5 min, a melt temperature of 210 °C, and a clay concentration of 5 wt. %.

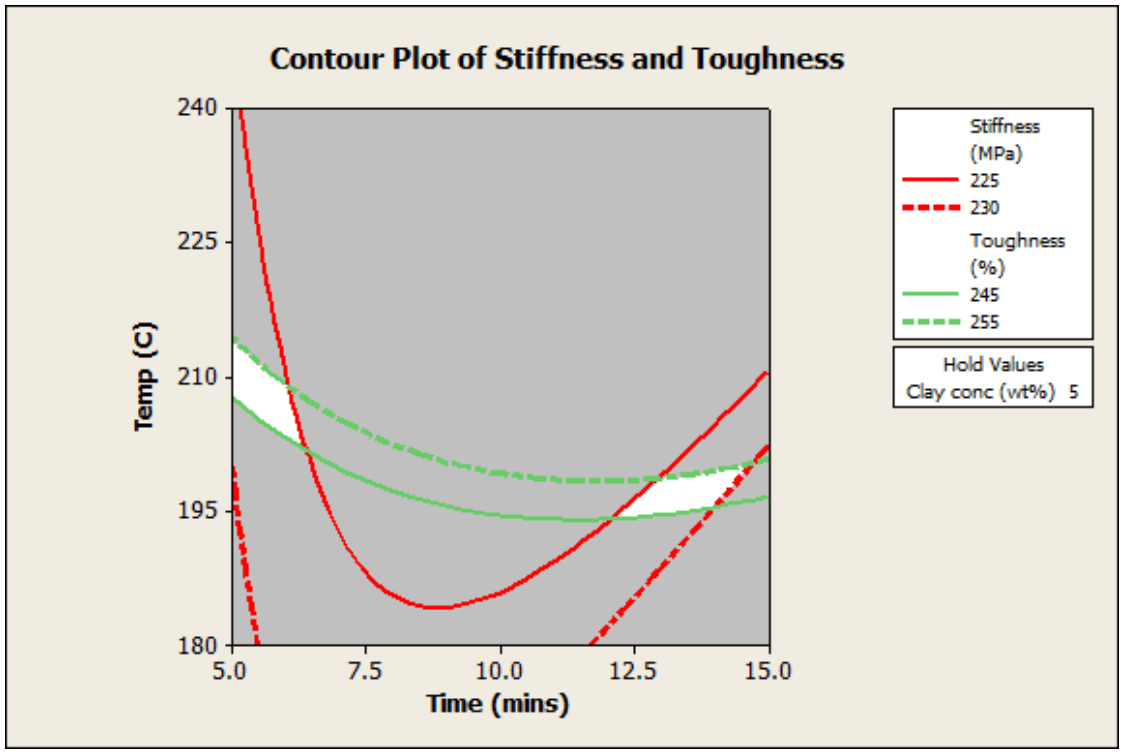


Figure 3-3: Overlaid contours for the stiffness and the toughness showing feasible region for desired optimum. The region between red lines is desired for secant modulus, while the region between green lines is desired for elongation at break. Therefore, the overlapping regions, the white regions, are the feasible regions

### 3.4.2 Processing Conditions of Twin-Screw Extruder

Since organoclay dispersion is the key to obtaining enhanced mechanical properties, it is necessary to evaluate and optimize the effects of the TSE processing parameters (i.e., screw speed and feed rate) on clay dispersion in the masterbatches. Since a temperature of 210 °C was determined to facilitate clay dispersion in DSM dilution process, a temperature range of 180 – 210 °C was set in the TSE (see the temperature profile in Figure 3-5). For the specific polymer nanocomposite used in this study, the manufactured masterbatches contain 25 wt. % organoclay, which was determined by previous work in DuPont. Note that the feed-rate is a total feed-rate (the sum of polymer feed-rate and organoclay feed-rate).

The organoclay dispersion was quantified by stiffness (1% secant modulus) of the final product, where larger values of the secant modulus correspond to better dispersion of organoclay [42]. The optimal DSM processing conditions determined in the previous section were used in the masterbatch diluting process.

A face-centered cubic response surface design with experimental conditions indicated in Table 3-5 was employed in evaluating the effects of the TSE processing parameters, screw speed ($N$) and feed rate ($Q$), on the secant modulus of the final product. The ranges of the conditions were determined by the capabilities of the extruder and the feeders. Five centerpoint run condition replicates were performed to determine the reproducibility of the process. Moreover, a random sequence of experiments was implemented to minimize the sample preparation error.

Table 3-5: Face-centered cubic response surface design of experiment for optimizing the TSE factors to achieve desired dispersion level in the masterbatches

| State No. | TSE factors | | Response |
|---|---|---|---|
| | Screw speed (rpm) | Feed-rate (lb/h) | Secant modulus (MPa) |
| 5 | 300 | 10 | 217.97 |
| 7 | 500 | 5 | 208.75 |
| 3 | 300 | 15 | 230.62 |
| 11 | 500 | 10 | 216.86 |
| 8 | 500 | 15 | 225.13 |
| 10 | 500 | 10 | 218.41 |
| 2 | 700 | 5 | 205.85 |
| 13 | 500 | 10 | 211.29 |
| 6 | 700 | 10 | 206.92 |
| 12 | 500 | 10 | 211.82 |
| 9 | 500 | 10 | 215.62 |
| 1 | 300 | 5 | 221.19 |
| 4 | 700 | 15 | 218.50 |

The results of statistical analysis carried out by Minitab® are shown in Figure 3-4. Recalling that large values of the secant modulus indicate better dispersion of organoclay, the contour plot reflects that organoclay dispersion improves as screw speed decreases and feed-rate increases, which means that the dispersion increases with high $Q/N$ ratio. These findings are consistent with a recent study of Bigio's group, where an increase in the dispersive mixing with high $Q/N$ ratio was reported [95].

Based on the results, a screw speed of 300 rpm (the lowest screw speed) and a feed-rate of 8 lb/h were selected as the operating condition that facilitates the clay dispersion in the masterbatches. Although Figure 3-4 suggests that a maximal feed-rate, 15 lb/h, will yield the stiffest product, a feed-rate of 8 lb/h was chosen instead. The rationale of such a choice is related to the process physics, which will be discussed in the next section.

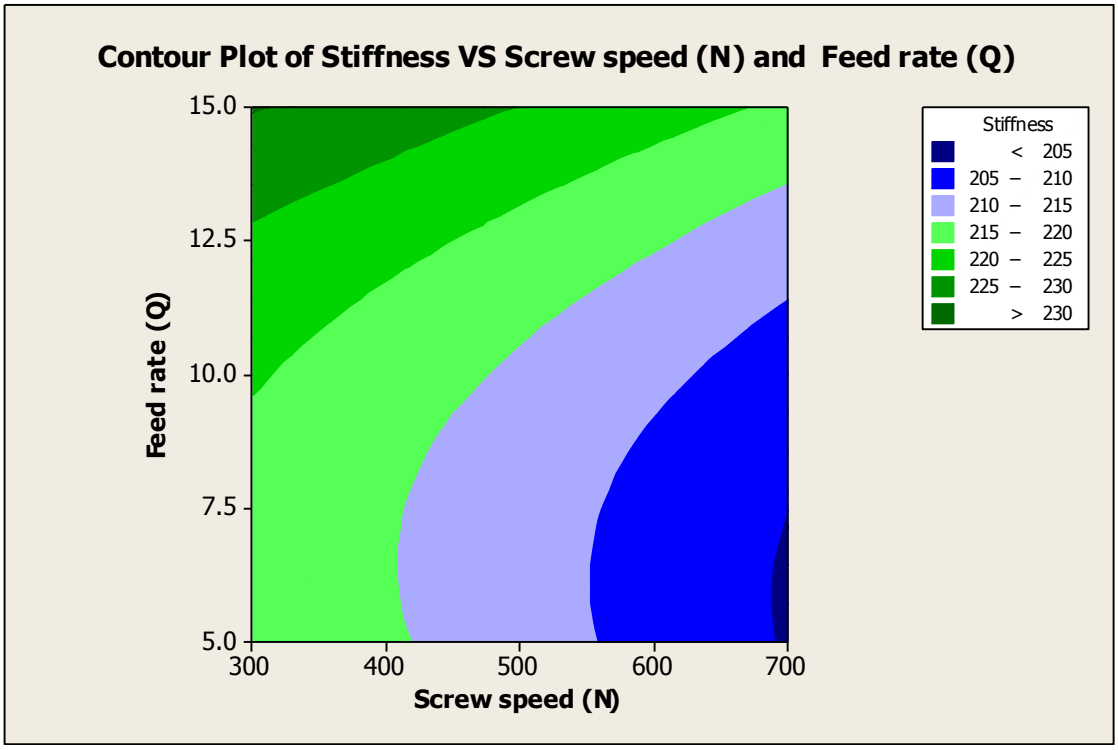


Figure 3-4: Contour plot for the stiffness as a function of screw speed and feed rate

### 3.5 Dispersion Sensitive Factor Identification

The key to producing nanocomposites with target performance is to ensure desired dispersion of clay particles in the polymer matrix, which in turn affects the end-use properties. For an effective control of end-use properties, the ideal manipulated variables must be sensitive to the clay dispersion. As a result, a control diagram directly incorporating regulation of end-use properties needs to be designed and implemented effectively in the manufacturing process. However, the TSE processing variables, such as screw speed and feed rate, do not satisfy this requirement. From Figure 3-4, it is observed that the range of stiffness between the lowest and highest magnitude of stiffness is approximately 25 MPa, which is not significant enough to demonstrate the change in clay dispersion.

Alternatively, as the types of amine surfactants used to modify clays have significant effects on organoclay dispersion in the polymer matrix, it is reasonable to use the organoclay types to alter the clay dispersion. For our specific Na ionomer-based polymer nanocomposites, two organically modified clays, Cloisite® 20A (20A) and Cloisite® 93A (93A), were used as reinforcement. Both organoclays were prepared by a cation exchange reaction between Na-MMT and ammonium surfactants. The surfactant used to prepare 20A was a quaternary ammonium surfactant with two long-alkyl tails (di-methyl bis(hydrogenated) tallow), i.e., $M_2(HT)_2$ [15], while the surfactant used to prepare 93A was a ternary ammonium surfactant with two long-alkyl tails (methyl di(hydrogenated) tallow), i.e., $M_1H_1(HT)_2$, where M is for methyl, H is for hydrogen, and HT is for hydrogenated tallow oil. Since 93A is treated with a more polar modifier ($M_1H_1(HT)_2$), it appeared to be thermodynamically incompatible with the Na ionomer, which results in poor organoclay dispersion [93]. Therefore, the organoclay mixture of 20A and 93A were used to reinforce the polymer matrix, and

the 20A concentration in the mixture is the ideal candidate for the manipulated variable to regulate the clay dispersion.

To incorporate the 20A concentration in the control diagram, a third feeder must be used for 93A to change the 20A concentration dynamically. The 93A feeder available can only run as high as 0.8 lb/h. Under this limitation, we have to maintain the organoclay concentration in masterbatches at 25 wt. % and at the same time be able to adjust the 20A concentration. Also, as previously discussed in section 3.4.2, a higher total feed rate is desired since it leads to better dispersion. Given these considerations, a total feed-rate of 8 lb/h was selected as the TSE operating condition, and an initial 20A concentration of 70% was determined.

## 3.6 Detailed Process Description

The proposed product design needs to be integrated with an appropriate control scheme for the manufacturing process to ensure the properties of polymer nanocomposites aligning with customer specifications. Using a melt mixing masterbatch method as the manufacturing process, the specific experimental system that is used to illustrate the design and implementation of the control strategy involves the mixing of Na ionomer polymer and organoclay mixture of 20A and 93A to manufacture masterbatches in a Coperion W&P ZSK-18mm co-rotating, intermeshing twin screw extruder. Other components of the experimental process includes separate Ktron® feeders for polymer, organoclay 20A, and organoclay 93A, thermocouples, pressure transducers, a cold-water quench bath, and a pelletizer mounted onto the machine.

The key features of the twin screw extruder are listed as follows. The polymer pellets and the organoclay powder were fed from two different hoppers: Polymer in

the main feeding hopper while organoclay mixture in the side feeding hopper (see Figure 3-5). The screw length-to-diameter ratio is 41, and the screw configuration and temperature profile are shown in Figure 3-5. It consists of forward conveying elements and three sets of kneading discs with the first and the third ones followed by a reverse conveying element. The function of the first set of kneading discs is to melt the solid polymer feed, while the second and third sets are used for mixing the polymer melt and the organoclay powder effectively.

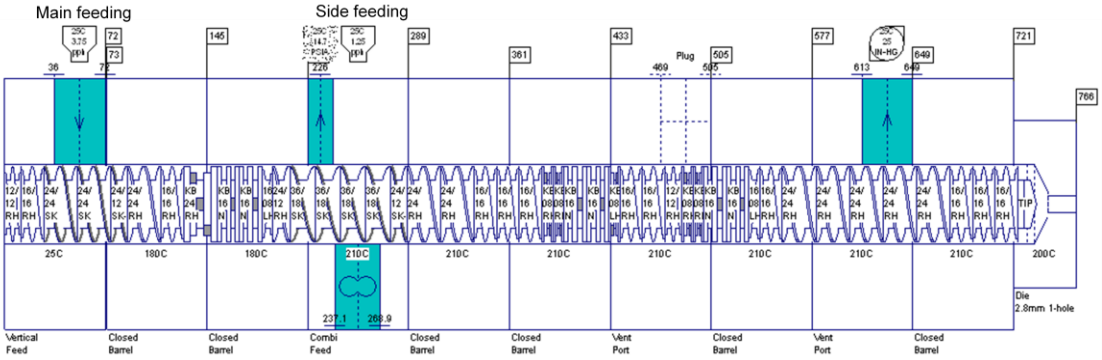


Figure 3-5: Screw configuration and temperature profile in the twin-screw extruder

A specialized data acquisition (DAQ) system developed by DuPont, the "Extrusion Pulse Analysis System" (EPAS) [96, 97], was employed for data acquisition of process variables. The signals wired to the EPAS front end are screw speed, feed-rates for three feeders, motor power, die pressure, and exit melt temperature (see Figure 3-6). This DAQ system was employed to collect process data for controller $C_1$, which will be discussed in Chapter 5.

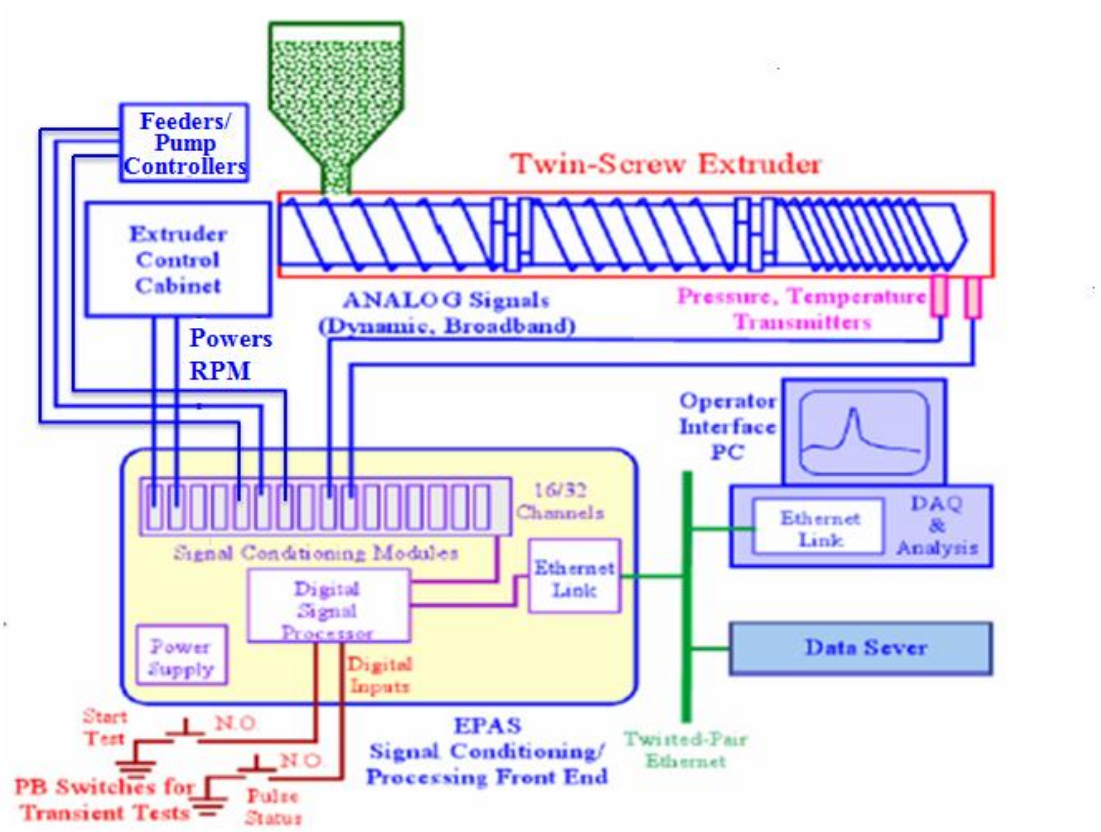


Figure 3-6: The architecture of the EPAS for data acquisition [96] (the twin screw extruder is used to manufacture clay-rich masterbatches)

## 3.7 Conclusions

Systematic product design is a premise to manufacture products designed for a specific end-use application in a continuous fashion. In product design, the customer needs are first translated into specific materials, following which the manufacturing process is designed and the required operating conditions are determined. In this chapter, we illustrated the systematic procedure of product design using a specific example of product design for packaging films.

In the packaging film example, according to the packaging application, the manufacturing product was initially determined to be polymer nanocomposites with Na ionomer as the polymer matrix and an organically modified MMT as the reinforcement. Then, a two-step melt mixing masterbatch method was employed to manufacture the material. Specifically, we selected the TSE for producing clay-rich masterbatches and the DSM micro compounder for diluting the product to the desired clay concentration. Subsequently, we determined the optimal settings for the DSM processing conditions and clay concentration (screw speed – 100 rpm, mixing time – 5 min, melt temperature – 210 °C, and clay concentration – 5 wt. %) required to obtain product with desired end-use properties (e.g., stiffness and toughness) through a series of experimental designs. Finally, we selected TSE processing conditions as a screw speed of 300 rpm and a total feed-rate of 8 lb/h to obtain high level of clay dispersion.

Another component of product design is to identify factors that strongly affect clay dispersion. The successful performance of an effective property control of polymer nanocomposites strongly depends on the selection of appropriate manipulated variables that have significant effects on clay dispersion. We found that the organoclay type has a significant effect on the clay dispersion, which strongly affects the mechanical properties in turn: Cloisite® 20A improves the clay dispersion, while

Cloisite® 93A deteriorates the extent of clay exfoliation. Therefore, the 20A concentration in the 20A and 93A mixture was identified as the factor that is sensitive to clay dispersion, and the 20A concentration will be used as the manipulated variable for the product property control. Finally, the details of the TSE process was introduced, based on which the multivariate multiple-loop control scheme (see Figure 2-3) will be developed and implemented in the following chapters.

# Chapter 4

# QUANTIFICATION OF CLAY DISPERSION

## 4.1 Introduction

Because the degree of clay dispersion within the polymer matrix is the key to obtaining desired product properties, any rational strategy for manufacturing polymer nanocomposites (PNC) that will meet prescribed product property targets consistently requires a means for quantifying clay dispersion. In practice, it is customary to characterize the dispersion level of clay layers by such techniques as X-ray diffraction (XRD) [98, 99], transmission election microscopy (TEM) [25, 82, 99-102], rheological measurements [25, 103, 104], atomic force microscopy (AFM) [105] and nuclear magnetic resonance (NMR) [106, 107], with XRD and TEM being the most widely used. While XRD is effective in most cases, it is often incapable of distinguishing what should be classified as immiscible from what is delaminated [99, 108]. On the other hand, TEM, with its visual representation of clay dispersion, provides a much more direct and reliable method for determining the degree of dispersion than XRD. However, in principle, these techniques allow only qualitative evaluation of the degree of clay dispersion.

### 4.1.1 Previous Efforts for Quantifying Dispersion

To date, the few techniques available for quantitative analysis of the degree of layered silicates dispersion are based on TEM image analysis and fall into the following two categories.

1). *Distance measurement based method*. Eckel *et al.* [109] quantified the dispersion of clay particles with linear intercept distances, determined by placing an array of parallel lines across TEM micrographs and then dividing the total length of the lines by the number of times the lines intersect the clay particles. A smaller line intercept distance, indicating a larger number of particles along the lines, indicates better dispersion. However, this method is based on average distances, an aggregate metric not truly representative of the actual distribution of the spacing between particles (since it is possible for differently distributed spacings could end up with identical averages); the metric is also highly dependent on clay loading and clay orientation. Luo and Koo [110] developed a quantification method based on relating the degree of dispersion to the "free-path distance", the distance between single platelets along parallel lines superimposed on TEM images. A histogram of the free-path distance was then obtained from TEM image analysis and fitted to a log-normal model. A dispersion parameter, $D_{0.1}$, defined as the probability of the free-path distance falling in the range of $\mu \pm 0.1\mu$ (where $\mu$ is the mean value of the free-path distance), was then calculated from the log-normal model. They noted that for exfoliated composites, $D_{0.1} > 8\%$, while $4\% < D_{0.1} < 8\%$ for intercalated composites. This method is effective for exfoliated and intercalated microstructures with small size tactoids and provides critical values for systems with different dispersion levels. However, for a microstructure containing larger agglomerations, the method is

ineffective because of the inherent difficulty in determining distances within the large agglomerations accurately. To rectify this problem so that agglomerations can be adequately taken into consideration, Tyson et al. [111] modified the Luo and Koo's method by introducing an agglomeration parameter $A$ in addition to $D_{0.1}$. The parameter $A_{0.3}$, representing the total number of particles in the range of $\mu \pm 0.3\mu$, was then calculated from the log-normal model fitted to the histogram of particle size data (including agglomerations). By its definition, a lower value of $A_{0.3}$ indicates lower agglomeration. The dispersion parameter $D_{0.1}$ and agglomeration parameter $A_{0.3}$ are considered simultaneously in determining dispersion. This method was shown to be effective when applied to carbon nanotubes (CNTs) within aqueous solutions; but it does not work well with agglomerations of uniform dimensions. Also, as noted in Bray *et al.* [112], there are no formal statistical assessment of the validity of the probability model assumptions on which these methods are based.

2). *Particle analysis based methods*. Dennis *et al.* [31] and Fornes *et al.* [25] proposed clay particle density, the number of platelets or intercalates per unit area, as a quantitative means of comparing the degree of dispersion in different samples. According to the proposition, a higher clay density should indicate better dispersion. However, this metric is clearly dependent on clay loading and therefore cannot be used universally. An alternative method proposed by Nam *et al*. [113] involves measuring the clay particle length $L_{clay}$ and thickness $d_{clay}$ of dispersed clay particles, and the correlation length $\xi_{clay}$ between dispersed layers (the space distance surrounded by the dispersed clay particles), and using them to estimate the average number of individual layers in a clay stack. However, this method is also based on averages, which are non-unique representations of full distributions of the $L_{clay}$, $d_{clay}$,

and $\zeta_{clay}$ measurements. Recent studies [82, 100-102, 114, 115] characterize the dispersion of clay particles with an additional parameter, aspect ratio of the clay stack. For example, Paul and coworkers in Lee *et al.* [100], Shah *et al.* [101], Kim *et al.* [102], and Spencer *et al.* [82] used measurements of number-/weight-average particle length ($\overline{l_n}$, $\overline{l_w}$), number-/weight-average particle thickness ($\overline{t_n}$, $\overline{t_w}$), and number-/weight-average aspect ratio ($\langle l/t \rangle_w$, $\langle l/t \rangle_n$) to characterize the dispersion levels of clay particles, concluding that higher aspect ratios indicate lower number of platelets in a stack, and hence correspond to better dispersion. The distributions of these parameters were available; however, these distributions were only used to provide qualitative description about clay dispersion. Carastan *et al.* [114] and Vermogen *et al.* [115] categorized clay particle formations in nanocomposites into several discrete groups (such as "individual sheets", "thinner tactoids", "thicker tactoids", and "agglomerates") according to the number of platelets in each particles. Each categorical group was then characterized by such metrics as mean thickness, mean length, and aspect ratio. These groups are subsequently used as the basis for characterizing the dispersion state of a polymer nanocomposite sample in terms of the relative frequency of occurrence of each group in the sample in question. For example, the predominance of micron size agglomerates in a PNC sample indicates poor dispersion, as opposed to the predominance of "individual sheets". The methodology is thus based on a bar chart representation of the composition of the particles in each sample, indicating the relative amount of the "basis groups" represented in the sample. Such a representation is thus only visual and does not provide an absolute, single quantitative characterization of the actual extent of dispersion in each sample.

### 4.1.2 Objectives and Approaches

The aim of this chapter is to propose an alternative quantification method for evaluating layered silicates dispersion based on a probabilistic analysis of particle length distributions obtained from TEM images. The approach is based on a formally validated probability model of particle length distribution and uses the model parameters to quantify clay dispersion directly. In this chapter, we first present fundamental arguments to justify the appropriateness of a proposed probability model for characterizing the distribution of clay particle lengths in polymer matrices in section 4.2.1. The resulting particle length distribution (PLD) model is then validated with experimental data in section 4.2.2 before we discuss how to quantify dispersion with the PLD characteristic parameters in section 4.2.3. Finally, the proposed technique is demonstrated experimentally by using it to quantify the dispersion of polymer nanocomposites with distinct dispersion characteristics that were produced in our laboratory in section 4.3.

## 4.2 Quantification Method Development

### 4.2.1 Characterizing Particle Length Distributions

Our quantification method is based on appropriate probability distribution function (pdf) to describe particle lengths. In polymer nanocomposites, the particle length, defined as the length of a single dispersed platelet or an agglomerate of platelets, as depicted in Figure 4-1 [25], is not uniform for several reasons. First, the length of each platelet in a particle is non-uniform. Secondly, a particle consists of one or more platelets, so that the number of platelets in each particle varies randomly from one particle to another (Figure 4-1 a). Finally, how the platelets are stacked to form a particle is also non-uniform so that two particles with the same number of platelets

may still have difference effective lengths (Figure 4-1 b). Consequently, the particle lengths of layered silicates in a polymer matrix are randomly distributed over a range of values which in practice can be anywhere from several nanometers to a few hundred microns.

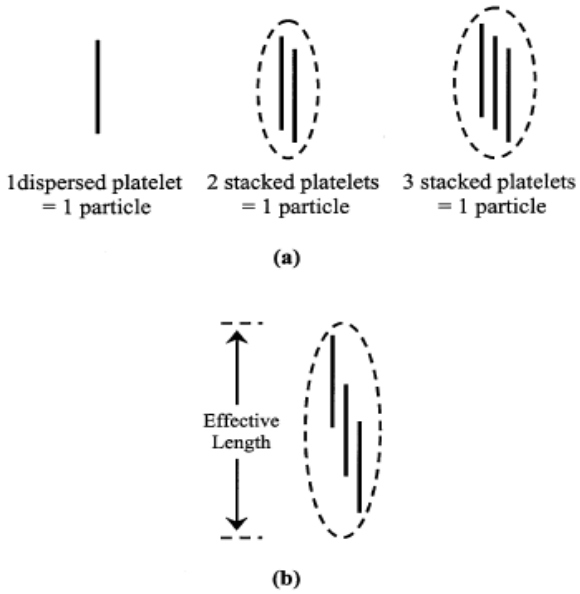


Figure 4-1: An example of (a) particle definition; (b) effective particle length measurement [25]

To describe the variability inherent in layered silicate particle lengths adequately, we observe first that the number of platelets in a particle has Poisson-like characteristics (see the reference [116]). Thus, if $z$ is the number of platelets in a particle, then the formation of each particle occurs as a result of the occurrence of $z$ Poisson events; and if the Poisson events are occurring at a mean "intensity" of $1/\beta$ per unit

length, then $x$, the interval length over which $\alpha$ Poisson events have occurred is known to follow a gamma distribution with the following pdf [116]:

$$f(x) = \frac{1}{\beta^{\alpha}\Gamma(\alpha)} x^{\alpha-1} e^{-x/\beta} \qquad 4\text{-}1$$

Thus, we postulate that for truly randomly dispersed clay platelets in a polymer matrix, the distribution of the particle length will be adequately described by the indicated gamma $\gamma(\alpha, \beta)$ pdf, where $\alpha$ represents the mean number of platelets per particle. Now, $\mu$, the mean of the gamma distribution (in this case, the mean particle length) by definition is given by:

$$\mu = \alpha\beta \qquad 4\text{-}2$$

Consequently, the parameter $\beta$ in this particular application, which, mathematically is obtained as:

$$\beta = \mu/\alpha \qquad 4\text{-}3$$

implies that for this specific application of the gamma distribution,

$$\beta = \frac{mean\ particle\ length}{mean\ number\ of\ platelet\ per\ particle} \qquad 4\text{-}4$$

We may now observe that the parameter $\beta$ corresponds to a mean effective platelet length.

We propose that these gamma pdf parameters may be used to quantify layered silicate dispersion as follows. Because the dispersion of silicate layers is related to the number of platelets stacked together, technically, fewer platelets should imply better dispersion. Consequently, smaller values of $\alpha$ will indicate better dispersion. But this is not sufficient. The second parameter, $\beta$, by definition of the gamma distribution, is a

scale parameter, indicative of the width of the PLD. Large values of $\beta$ are associated with broader distributions, generally indicating poorer overall dispersion. But since $\beta$ represents the mean effective particle length, its value can be large (within reason) either because the mean particle length is large (not desired) or because the mean number of platelets per particle, $\alpha$, is small (desired), or both. The implication therefore is that a relatively large $\alpha$ value by itself is not necessarily bad, so long as it is accompanied by a commensurably small value of $\beta$; similarly, a large value of $\beta$ does not automatically indicate poor dispersion, so long as the accompanying $\alpha$ value is commensurately small. Thus, neither $\alpha$ nor $\beta$ in isolation is sufficient by itself to ascertain the quality of dispersion; a combination of both is required. As we show later with actual data, quality of dispersion may be quantified by the empirical expression:

$$\alpha + C_1\beta = C_2 \qquad 4\text{-}5$$

But first we will validate the proposed gamma probability model for characterizing PLD with experimental data.

### 4.2.2 PLD Model Validation

To validate the gamma probability model postulated for describing PLDs, we turn to data from the literature. The studies from which these data sets were obtained involve polymer-clay nanocomposites samples made by melt intercalation and PLD data obtained from TEM micrographs of these samples. The lengths of several hundred particles were determined from appropriate image analyses of the TEM micrographs, from which the particle length distribution data were generated. A representative example in Figure 4-2 (a) shows a histogram of raw particle length data (ranging from 10 nm to 300 nm), for polyamide 6/organoclay nanocomposites [117]. The

theoretical gamma probability model fit (blue line) to the normalized histogram (gray bars) is shown in Figure 4-2 (b) along the least squares estimates of the parameters $\alpha$ and $\beta$ and the corresponding 95% confidence intervals.

While a visual inspection of Figure 4-2 (b) definitely indicates reasonable agreement between model and data, rigorous model validation requires formal statistical tests of "goodness-of-fit" of which the two most widely employed are the Chi-square test and the Kolmogorov-Smirnov test [116].

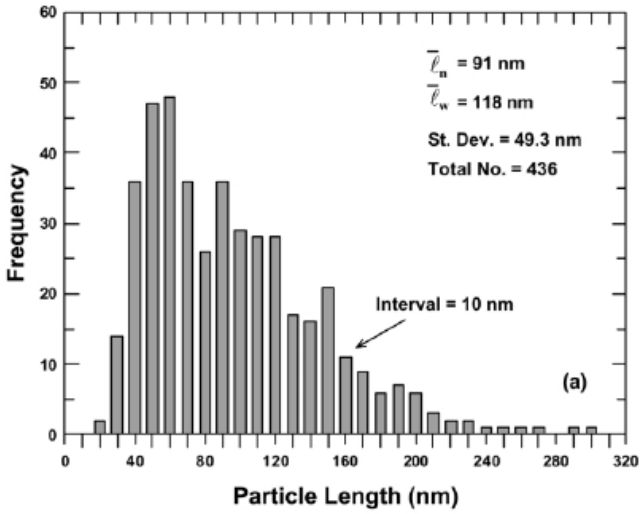


(a)

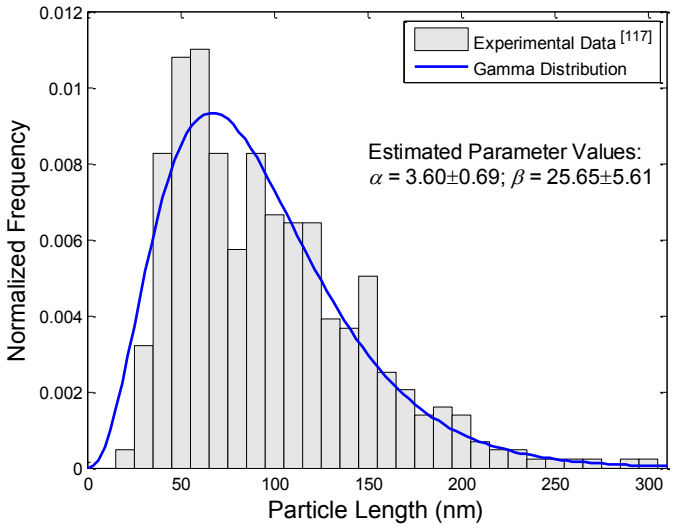


(b)

Figure 4-2: (a) Particle length histogram for polyamide/clay nanocomposites [117]; (b) Particle length distribution (histogram) and the corresponding theoretical gamma distribution fit (indicated estimates of parameters $\alpha$ and $\beta$ along with corresponding 95% confidence intervals obtained via least squares.)

The Chi-square test is a formal hypothesis test based on the test statistic $C^2$ defined as:

$$C^2 = \sum_{i=1}^{m} \frac{(f_i^0 - \varphi_i)^2}{\varphi_i} \quad 4\text{-}6$$

where $f_i^0$ is the observed frequency from data, $\varphi_i$ is the corresponding frequency from the candidate probability model under consideration, and $m$ is the number of bins in the histogram. The null hypothesis (that the data follow the postulated probability model), when tested at the traditional $\alpha = 0.05$ significance level, is rejected if

$$C^2 > \chi^2_{0.05}(\upsilon) \quad 4\text{-}7$$

with $\chi^2_{0.05}(\upsilon)$ as the $\upsilon$-degrees-of-freedom Chi-square variate for which the right tail area probability is 0.05 ($\upsilon = m - p - 1$, and $p$ is the number of parameters in the candidate probability model) (see Chapter 17 of the reference [116]).

The Kolmogorov-Smirnov (K-S) test, on the other hand, is a non-parametric test based on a comparison of the empirical cumulative distribution function $F_E(x)$ (obtained from the data in question) with the theoretical cumulative distribution function $F(x)$ of the postulated probability model. The null hypothesis (that the data follow the postulated probability model) is rejected at the 0.05 significance level when the value of the test statistic:

$$D_n = \sup_{x \in R} \left| F_E(x) - F(x) \right| \quad 4\text{-}8$$

exceeds the critical value $D_{0.05}$, a value typically determined from statistical analysis software packages (see Chapter 18 of the reference [116]).

For the illustrative example in Figure 4-2 (b), the result of Chi-square test is shown in Table 4-1. It is observed that $C^2 < \chi^2_{0.05}(26)$. Therefore, we conclude that

the gamma probability model provides adequate representation of the particle length distribution data.

Figure 4-3 shows a comparison of the empirical cumulative distribution (from data) and the theoretical gamma model cumulative distribution. The results of a formal K-S test returned a value of $D_n$ = 0.0371 which when compared with the critical value $D_{0.05}$ = 0.0582 leads us to conclude, once again, that the gamma probability model provides an adequate fit to the experimental data. In the rest of the chapter, we will employ only the K-S test to validate our probability models.

The gamma pdf model $\gamma(\alpha, \beta)$ with $\alpha$ = 3.6 and $\beta$ = 25.65 has thus been formally validated as providing a good representation of the particle length distribution in polyamide 6/organoclay nanocomposites discussed in reference [117]. For now, we observe that the value $\alpha$ = 3.6 indicates that the material in question has an average of 3.6 platelets stacked together per particle, indicating relatively good layered silicates dispersion. The value $\beta$ = 25.65 (representative of a relatively broad distribution of particle lengths as seen from the histogram), even though indicative of a fairly large mean effective platelet length, taken in combination with the relatively small $\alpha$ value appears to suggest good clay dispersion. As we now show, it is possible to combine these parameters mathematically to generate a quantitative and objective measure of dispersion.

Table 4-1: Chi-square test results for polyamide/clay nanocomposites

| Polymer nanocomposites | Chi-square test | | |
|---|---|---|---|
| | $C^2$ | $\chi^2_{0.05}(26)$ | Result |
| Polyamide/clay nanocomposites | 35.29 | 38.90 | Adequate |

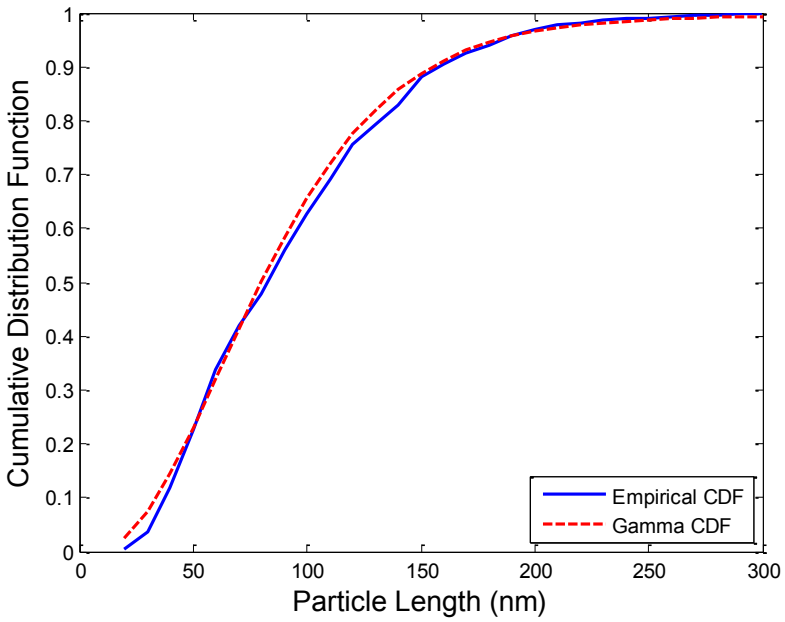


Figure 4-3: Kolmogorov-Smirnov test results for the PLD data of polyamide/clay nanocomposites

### 4.2.3 Dispersion Quantification

Dispersion states, indicative of how particles are distributed within the polymer matrix, are generally (and qualitatively) classified as exfoliated, intercalated or immiscible. Having just established that such particle distributions (specifically of the particle lengths) are well represented quantitatively by the gamma pdf, $\gamma(\alpha, \beta)$, with the parameters $\alpha$ and $\beta$ fundamentally and *jointly* indicative of the extent of dispersion but in a yet unspecified manner, what remains now is for us to relate these parameters explicitly and quantitatively to dispersion states. For this, we adopt the following empirical approach where (i) PLD data from a wide variety of polymer nanocomposites having different dispersion characteristics will be fit to the gamma pdf model, thereby (ii) generating a collection of $\alpha$ and $\beta$ parameter values along with the dispersion states corresponding to each pair, from which finally, (iii) we will then determine a quantitative expression relating $\alpha$ and $\beta$ pairs to dispersion explicitly.

The specific PLD data sets chosen for this procedure all come from Paul and co-workers [42, 100, 101, 118, 119], i.e., from the same research group, and ostensibly generated by the same experimental protocol, thereby eliminating any potential and extraneous lab-to-lab variability. The relevant details about the various nanocomposites materials used in generating the data sets are as follows. Polymer Matrix: Polyamide 6 (PA-6) [42, 119], polyamide 66 (PA-66) [119], poly(ethylene-*co*-methacrylic acid) (EMMA) [101], sodium, zinc, and lithium ionomers of EMMA (ionomer) [118], polypropylene (PP) [100]; Organoclays: Sodium MMT (Na-MMT), which were ion exchanged with different quaternary ammonium surfactants; Surfactants: $(HE)_2M_1R_1$-YM and $(HE)_2M_1R_1$-WY [42], $M_2(C_{18})_1$ [119], and $M_2(HT)_2$ [100, 101, 118], (where YM and WY stand for Na-MMT sources located in Yamagata, Japan and Wyoming,

USA, respectively, and some frequently used abbreviations are employed here to describe the ammonium structures, i.e., HE for hydroxy-ethyl, R for rapeseed, M for methyl, H for hydrogen, and HT for hydrogenated-tallow oil). As discussed in the references, PA-6 and PA-66 based nanocomposites show fully exfoliated dispersion [42, 119], and the nanocomposites prepared from EMMA, and sodium, zinc, and lithium ionomers reveal thicker clay stacks compared to the one prepared from PA-6 and PA-66 [101, 118], while PP/organoclay nanocomposites have a mixed morphological structure, which is a combination of exfoliated particles and intercalated stacks [100]. These data sets therefore collectively provide representative samples from all the dispersion states of interest.

Upon subsequently characterizing the PLD data sets with the gamma pdf, the resulting least squares estimates of the characteristic parameters, $\alpha$ and $\beta$ along with their respective 95% confidence intervals, are shown in Table 4-2. Each resultant gamma probability model is validated using the Kolmogorov-Smirnoff (K-S) test; the result is shown in Table 4-2, where "A" indicates that the gamma pdf model is sufficiently adequate to describe the experimental data (i.e., the associated $p$-value is greater than 0.05), while "IN" suggests that the model's adequacy is indeterminable (because $0.01 < p < 0.05$; see reference [116]). Observe that the three cases for which the gamma model adequacy is questionable are all from the same reference [119]. The reason for this anomaly is not clear, but it may be attributable to the nature of the data sets, which in each case involves a large number of total particles but which were available only in the form of normalized particle length *histograms*, not raw particle length data. For consistency and to err on the side of caution, we excluded these data sets from subsequent analyses.

Table 4-2: Gamma probability model parameters estimates (and corresponding 95% confidence intervals) for various polymer nanocomposite PLD data, and corresponding goodness of fit test results ("A" represents that the model is adequate, while "IN" indicates that the model adequacy is indeterminate)

| Polymer nanocomposites (NC) | $\alpha$ with 95% confidence interval | $\beta$ with 95% confidence interval | K-S test result | No. of particles |
|---|---|---|---|---|
| PP/$M_2(HT)_2$ NC (1 wt. %) [100] | 4.21 ± 1.71 | 72.71 ± 33.28 | A | 120 |
| PP/$M_2(HT)_2$ NC (2.8 wt. %) [100] | 4.60 ± 0.82 | 48.23 ± 9.49 | A | 226 |
| PP/$M_2(HT)_2$ NC (6.8 wt. %) [100] | 5.64 ± 1.07 | 42.26 ± 8.72 | A | 311 |
| EMAA-1/$M_2(HT)_2$ NC [101] | 5.20 ± 1.56 | 24.59 ± 8.12 | A | 321 |
| PA-6/$(HE)_2M_1R_1$-WY NC [42] | 3.60 ± 0.69 | 25.65 ± 5.61 | A | 551 |
| PA-6/$(HE)_2M_1R_1$-YM NC [42] | 3.15 ± 0.52 | 32.40 ± 6.34 | A | 436 |
| PA-6/$M_2(C_{18})_1$ NC (240 °C) [119] | 4.45 ± 0.45 | 10.87 ± 1.22 | IN | 2121 |
| PA-6/$M_2(C_{18})_1$ NC (270 °C) [119] | 3.98 ± 0.53 | 11.90 ± 1.78 | IN | 2275 |
| PA-66/$M_2(C_{18})_1$ NC (270 °C) [119] | 4.82 ± 0.55 | 11.11 ± 1.46 | IN | 1414 |
| Li ionomer/$M_2(HT)_2$ NC [118] | 3.65 ± 0.38 | 47.02 ± 5.50 | A | 502 |
| Na ionomer/$M_2(HT)_2$ NC [118] | 3.91 ± 0.49 | 24.16 ± 3.45 | A | 762 |
| Zn ionomer/$M_2(HT)_2$ NC [118] | 3.58 ± 0.33 | 26.84 ± 2.84 | A | 703 |

From well-established characteristics presented in the literature, the dispersion state was determined for each nanocomposite allowing us to assign *à-priori* categorical ranks to each material. For example, PA-6 based nanocomposites are often "fully exfoliated" (excellent dispersion); EMMA and ionomer based nanocomposites are "less exfoliated" compared to PA-6 based nanocomposites; and PP based nanocomposites are "intercalated" (poor dispersion). Such an "*à-priori*" dispersion rank is shown in Table 4-3 in descending order from 1 to 9, where 1 indicates the best dispersion and 9 the worst. We observe that overall the degree of dispersion degree worsens as $\alpha$ and $\beta$ values increase. However, as noted earlier, the value of $\alpha$ or of $\beta$ by itself in isolation is insufficient as an indicator of the degree of dispersion; instead, the dispersion state depends on both $\alpha$ and $\beta$ simultaneously.

Table 4-3: Validated gamma probability model parameter estimates for various polymer nanocomposites, along with associated *à-priori* organoclay dispersion ranking in descending order

| "*a-prior*" dispersion rank | Polymer nanocomposites (NC) | $\alpha$ with 95% confidence interval | $\beta$ with 95% confidence interval | $\delta$ with 95% confidence interval |
|---|---|---|---|---|
| 1 | PA-6/$(HE)_2M_1R_1$-YM NC [42] | 3.60 ± 0.69 | 25.65 ± 5.61 | 4.88 ± 0.74 |
| 2 | PA-6/$(HE)_2M_1R_1$-WY NC [42] | 3.15 ± 0.52 | 32.40 ± 6.34 | 4.77 ± 0.61 |
| 3 | Zn ionomer/$M_2(HT)_2$ NC [118] | 3.58 ± 0.33 | 26.84 ± 2.84 | 4.92 ± 0.36 |
| 4 | Na ionomer/$M_2(HT)_2$ NC [118] | 3.91 ± 0.49 | 24.16 ± 3.45 | 5.12 ± 0.52 |
| 5 | EMAA-1/$M_2(HT)_2$ NC [118] | 4.19 ± 1.40 | 31.47 ± 11.77 | 5.76 ± 1.52 |
| 6 | Li ionomer/$M_2(HT)_2$ NC [118] | 3.65 ± 0.37 | 47.02 ± 5.50 | 6.00 ± 0.46 |
| 7 | PP/$M_2(HT)_2$ NC (1 wt. %) [100] | 4.21 ± 1.71 | 72.71 ± 33.28 | 7.85 ± 2.39 |
| 8 | PP/$M_2(HT)_2$ NC (2.8 wt. %) [100] | 4.60 ± 0.82 | 48.23 ± 9.49 | 7.01 ± 0.95 |
| 9 | PP/$M_2(HT)_2$ NC (6.8 wt. %) [100] | 5.64 ± 1.07 | 42.26 ± 8.72 | 7.75 ± 1.16 |

A scatter plot of $\alpha$ versus $\beta$ for each nanocomposite sample, shown in Figure 4-4, reveals a few important features regarding how these two parameters jointly encode dispersion characteristics. First, the points represented by the blue symbols, which correspond to nanocomposites with exfoliated dispersion characteristics, lie in the bottom left hand corner of the $\alpha$-$\beta$ plane; the points represented by the black symbols, corresponding to less exfoliated nanocomposites, lie in the middle of the plane; while the remaining points, represented by the red symbols, and corresponding to composites consisting of a combination of tactoids and exfoliated platelets

(indicative of poor dispersion), are located in the uppermost portions of the plane. Next, we observe that the three broadly identified regions in the $\alpha$-$\beta$ plane may be separated, to a first approximation, by the indicated parallel straight lines, represented mathematically as:

$$\alpha + 0.05\beta = \delta \qquad 4\text{-}9$$

The entire collection of parallel straight lines represented by Equation 4-9 may now serve as dispersion contours in the $\alpha$-$\beta$ plane, with $\delta$ as a quantitative measure of the dispersion state for each polymer/layered silicates nanocomposite in question, whose PLD data have been characterized by gamma model parameters $\alpha$ and $\beta$. As Figure 4-4 shows, lower $\delta$ values indicate better dispersion while higher $\delta$ values are associated with poorer clay dispersion. Finally we note in particular in Figure 4-4 that the dispersion for the specific samples used to generate this figure, $\delta$ = 5 indicates the boundary between exfoliated dispersion and less exfoliated dispersion, while $\delta$ = 6.5 indicates the boundary between less exfoliated dispersion and the poorer dispersion with combination of exfoliated particles and intercalated stacks. Consequently, if the data in Figure 4-4 are representative of general dispersion characteristics of polymer/layered silicates nanocomposites, then the implication is as follows: For dispersion characteristics quantified according to the empirical expression in Equation 4-9, $\delta < 5$ for exfoliated composites, $5 < \delta < 6.5$ for less exfoliated composites with stacks containing several layers, and $\delta > 6.5$ for intercalated composites. The next step is to confirm this result experimentally with new materials that are not part of the data employed to develop the methodology and the results shown in Figure 4-4 (see the scatter plot with error bars in Appendix B).

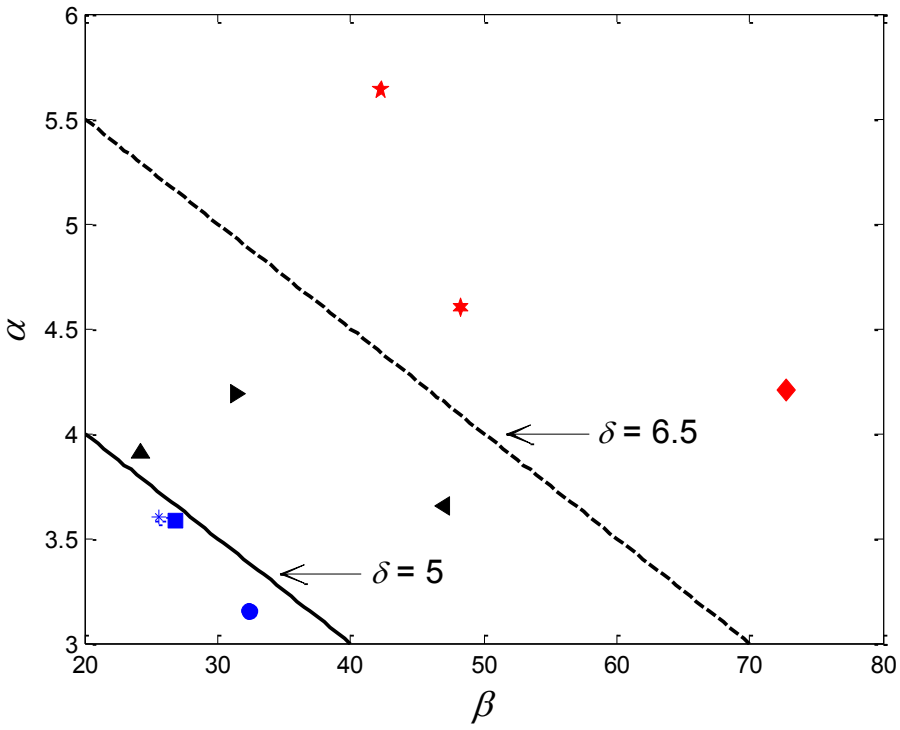


Figure 4-4: $\alpha$ versus $\beta$ for different polymer nanocomposites; the dispersion contours in the form of $\alpha + 0.05\beta = \delta$. Specifically, * for PA-6/$(HE)_2M_1R_1$-YM NC, ● for PA-6/$(HE)_2M_1R_1$-WY NC, ■ for Zn ionomer/$M_2(HT)_2$ NC, ▲ for Na ionomer/$M_2(HT)_2$ NC, ► for EMAA-1/$M_2(HT)_2$ NC, ◄ for Li ionomer/$M_2(HT)_2$ NC, ♦ for PP/$M_2(HT)_2$ NC (1 wt. %), six-pointed star in red PP/$M_2(HT)_2$ NC (2.8 wt. %), five-pointed star in red for PP/$M_2(HT)_2$ NC (6.8 wt. %)

## 4.3 Experimental Confirmation

The methodology of quantifying dispersion proposed in section 4.2 is then validated experimentally by using it to characterize and quantify the dispersion of two polymer nanocomposite samples made in our lab as described below.

In this section, we quantified the dispersion of two polymer nanocomposites with different clay mixtures as reinforcement: Na ionomer reinforced by 20A (i.e., Sample 1), and Na ionomer reinforced by the organoclay mixture with 80 wt. % 20A and 20 wt. % 93A (i.e., Sample 2). The dispersion of Sample 1 is expected to be better than that of Sample 2.

### 4.3.1 Experimental Details

*Nanocomposite preparation*

The masterbatch method proposed previously was employed to synthesize nanocomposites by diluting clay rich masterbatches (25 wt. % organoclay) into nanocomposites with 5 wt. % clay in a Coperion W&P ZSK-18mm co-rotating, intermeshing twin screw extruder. The processing conditions of the twin screw extruder were at a screw speed of 700 rpm and a total feed rate of 15 lb/h. Tensile specimens for TEM characterization were obtained via a DSM micro compounder and injection molding system (see section 3.4.1).

*TEM characterization*

Samples for TEM analysis were cut from the central part of the tensile bars perpendicular to the flow direction using an ultramicrotome with a diamond knife. Then, these samples were examined by FEI TECNAI G2 12 TWIN TEM operating under an accelerating voltage of 120 kV. The resulting TEM micrographs were at magnifications of 30 – 60 K, depending on the extent of exfoliation in the samples.

Representative TEM micrographs are shown in Figure 4-5 (a) for Sample 1 and Figure 4-5 (b) for Sample 2 (see Appendix A for all the TEM micrographs). In both cases the stacks of clay particles are broken up nicely and the clay particles are well exfoliated overall, even though fewer and smaller aggregates are observed in Sample 1 compared to Sample 2 than in Sample 1. A visual inspection of these TEM images therefore clearly suggests that Sample 1 shows better dispersion than Sample 2. We now employ the method proposed in previous section to ascertain quantitatively the dispersion characteristics of each sample and the extent to which the dispersion in one is better than the dispersion in the other.

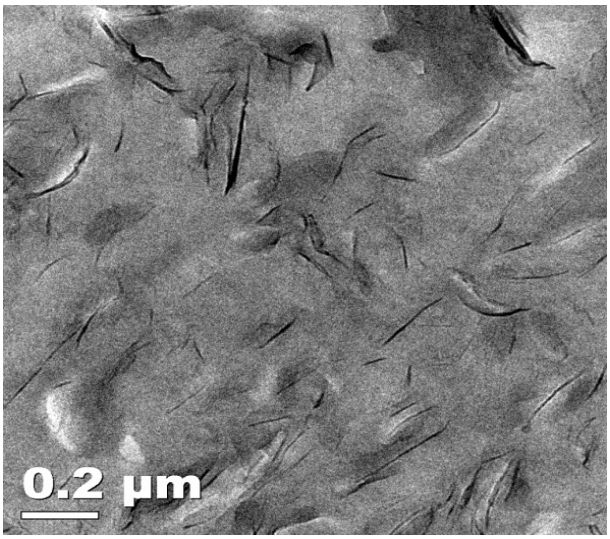


(a)

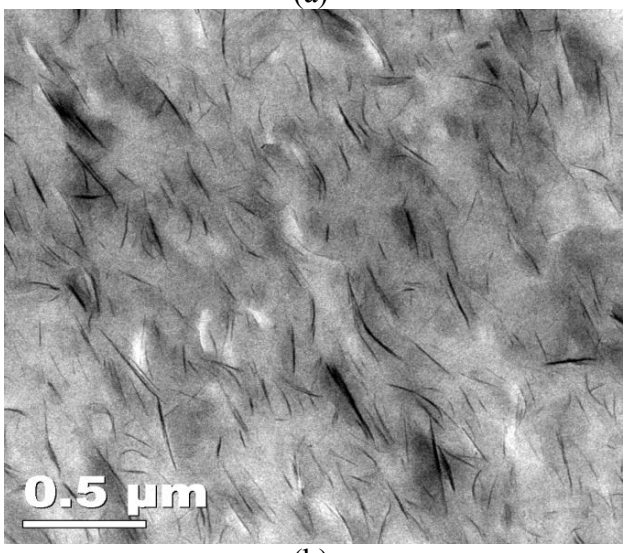


(b)

Figure 4-5: (a). TEM photomicrographs of Na ionomer/$M_2(HT)_2$ nanocomposites with nominally 5 wt. % MMT; (b). TEM photomicrographs of Na ionomer/organoclay mixture nanocomposites with nominally 5 wt. % MMT

### 4.3.2 Particle Analysis

Accurate particle lengths are determined based on image analysis of an original image with exceptional resolution and contrast. Unfortunately, most TEM images of polymer nanocomposites consist of different shades of gray such that image analysis tools are not able to distinguish the particles from the polymer matrix [117]. Therefore, it is necessary first to convert the original TEM micrographs into high contrast images before computing the particle lengths.

This section describes the details of particle analysis procedure used to determine the particle lengths from TEM images. Particle analysis involves two steps: (i) utilizing image processing to convert the low contrast TEM images to high contrast images (black and white images), and (ii) applying image analysis on the resulting high contrast images to compute the particle lengths.

#### 4.3.2.1 Image Processing

The image processing procedure we employed, shown schematically in Figure 4-6, is as follows. The original TEM micrographs, saved in .jpg or .tiff format, were first opened in GIMP (GNU Image Manipulation Program), where transparent layers were superimposed on the TEM images. Then, the lengths of the layered silicate particles were traced manually on the transparent layers, which were subsequently exported as black and white images where the particles stand out in sharp contrast against the white background. To avoid potential image analysis errors caused by variable line thicknesses, the black lines were "skeletonized" (rendering thick lines thin) with the software "Image J" to produce images of particles rendered as uniformly thin lines.

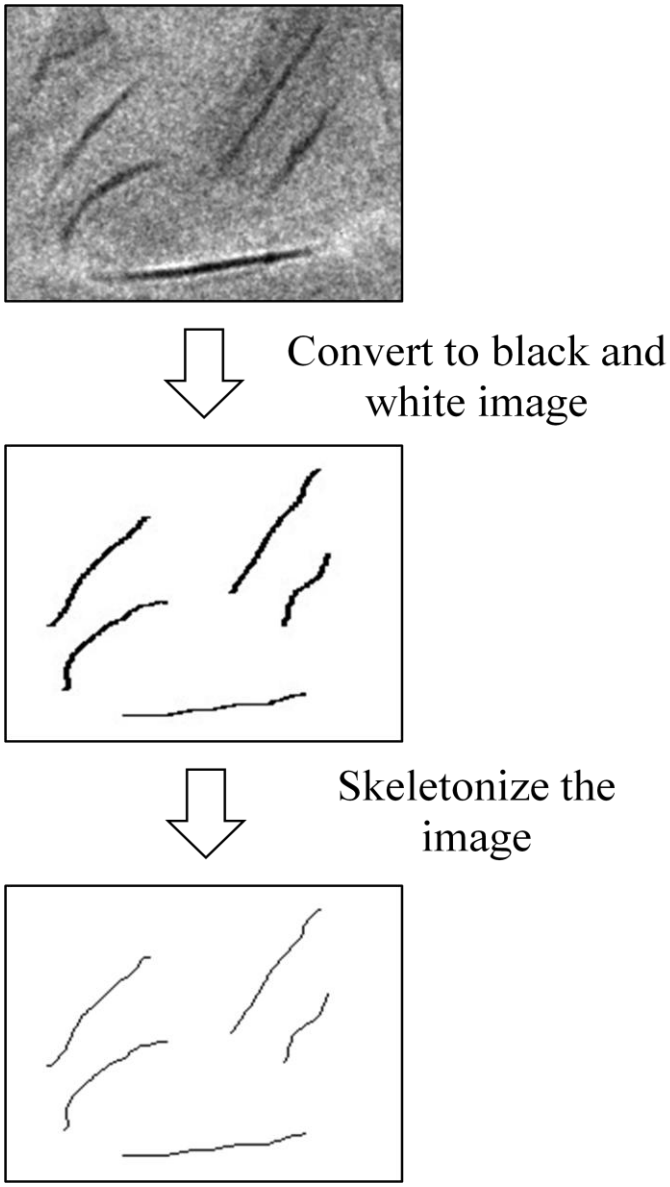


Figure 4-6: Schematic representation of TEM micrograph image processing procedure

#### 4.3.2.2 Image Analysis

The processed images were then imported into MATLAB® for image analysis from where we obtained raw particle length data using MATLAB's image analysis function *regionprops*. Particle length histograms were subsequently generated from data sets obtained from five to six TEM images in each case, for a total of at least 300 particles. The summary statistical characteristics for both data sets are shown in Table 4-4. And the resulting histograms of particle length are presented in Figure 4-7 (a) and Figure 4-7 (b), for Sample 1 and Sample 2, respectively.

Table 4-4: Statistics of Sample 1 (Na ionomer/$M_2(HT)_2$ nanocomposites) and Sample 2 (Na ionomer/organoclay mixture nanocomposites)

| Sample No. | Materials | $\mu$ (nm) | Minimum $x$ (nm) | Maximum $x$ (nm) | No. of particles |
|---|---|---|---|---|---|
| 1 | Na ionomer/$M_2(HT)_2$ NC | 114.25 | 30.26 | 350.22 | 304 |
| 2 | Na ionomer/organoclay mixture NC | 138.70 | 48.60 | 426.43 | 332 |

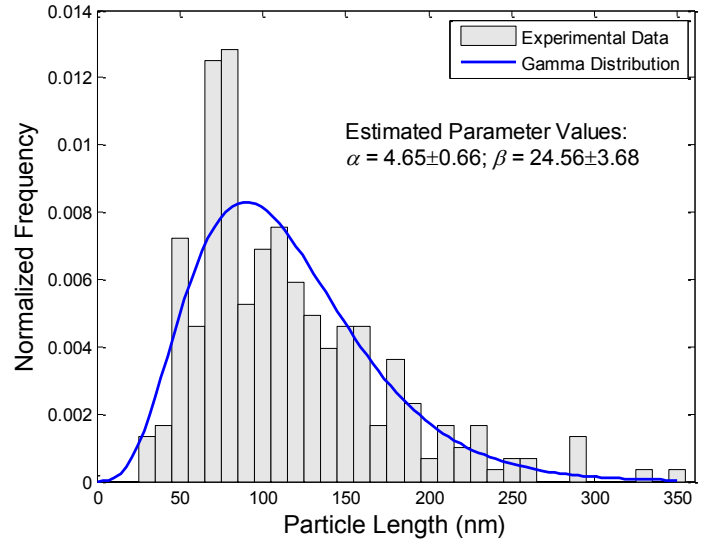


(a)

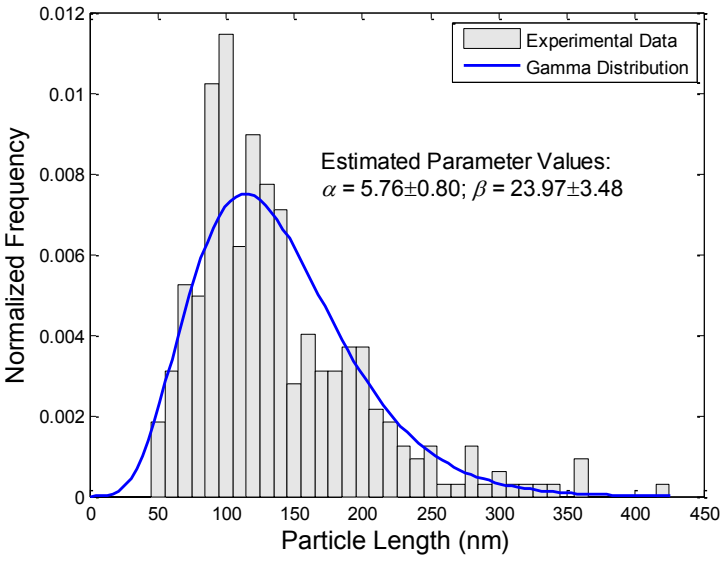


(b)

Figure 4-7: Particle length histogram and gamma probability model fit superimposed in blue along with least squares estimates of the parameters $\alpha$ and $\beta$ and corresponding 95% confidence intervals for (a). Sample 1: Na ionomer/$M_2(HT)_2$ nanocomposites; (b). Sample 2: Na ionomer/organoclay mixture nanocomposites.

### 4.3.3 Dispersion Characterization

We quantified organoclay dispersion for these samples by applying the proposed method to the resulting particle length histograms shown in Figure 4-7. First, a least squares fit of a gamma pdf to each PLD data produced the results shown in Figure 4-7; the blue lines represent theoretical probability model fit with estimated parameters along with 95% confidence intervals superimposed. The results of the K-S test employed to assess each probability model's goodness-of-fit – using MATLAB® hypothesis test function *kstest* – are shown in Figure 4-8 (a) and (b) for Sample 1 and Sample 2, respectively. (In each case, the formal statistical test, returned a value of $h$ = 0, indicating that there is no evidence to reject the null hypothesis, that the data follow the gamma probability model, at the 0.05 significance level). We conclude therefore that the gamma probability model indeed provides adequate theoretical representation of the particle length distribution for each sample.

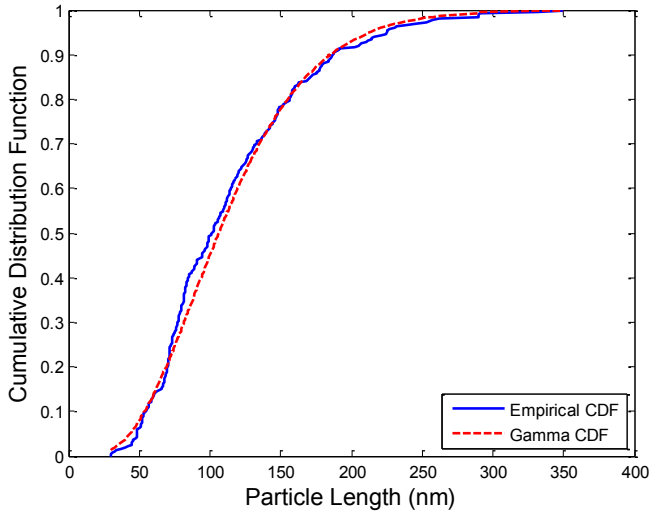


(a)

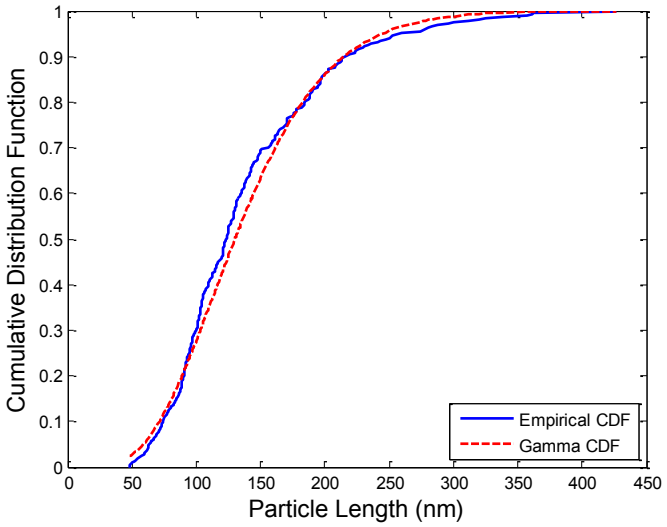


(b)

Figure 4-8: Comparison of empirical cdf and theoretical gamma cdf as part of the Kolmogorov-Smirnov goodness-of-fit test: (a). Na ionomer/$M_2(HT)_2$ nanocomposites; (b). Na ionomer/organoclay mixture nanocomposite

From the gamma distribution parameters and Equation 4-9, we now obtain the dispersion characteristic parameters as shown in Table 4-5: for the Sample 1, $\delta_1 = 5.85 \pm 0.69$ (between 5 and 6.5), indicating a mixed morphological structure, i.e., a combination of exfoliated platelets and intercalated stacks, as expected; for Sample 2, $\delta_2 = 6.96 \pm 0.82$ (larger than 6.5) indicating that there are more intercalated stacks in the polymer matrix, again, as expected. The dispersion index $\delta$ shows that the dispersion of Sample 1 is about 20% better than the dispersion of Sample 2, which is consistent with the findings in the reference [101]. We have thus established, with this set of new, independent experimental data obtained in our laboratory, that the proposed method is able to provide appropriate quantification of the extent of organoclay dispersion in polymer nanocomposites.

Table 4-5: Dispersion characteristics of Sample 1 (Na ionomer/$M_2(HT)_2$ nanocomposites) and Sample 2 (Na ionomer/organoclay mixture nanocomposites)

| Sample number | Materials | $\alpha$ | $\beta$ | $\delta$ |
|---|---|---|---|---|
| 1 | Na ionomer/$M_2(HT)_2$ NC | 4.65 ± 0.66 | 24.56 ± 3.68 | 5.85 ± 0.69 |
| 2 | Na ionomer/organoclay mixture NC | 5.76 ± 0.80 | 23.97 ± 3.48 | 6.96 ± 0.82 |

## 4.4 Conclusions

Effective quality control of polymer/organoclay nanocomposites is virtually impossible without a simple and quantitative dispersion characterization method. Developing such a quantification method that will relate clay dispersion directly to product performance remains a challenge. In this chapter, we proposed a novel method to quantify layered silicate dispersion in polymer/organoclay nanocomposites.

The method is based on a gamma probability model $\gamma(\alpha, \beta)$ description of particle length distribution data obtained from TEM micrographs, a postulate based on the fundamental mechanisms associated with clay particle formation in the polymer matrix. As a consequence of linking the postulated probability model to fundamental mechanisms, we were able to establish a connection between the probability model parameters, and physical characteristics of the polymer nanocomposites: specifically, $\alpha$ represents the mean number of platelets per particle, and $\beta$, the mean "effective platelet length". By an empirical analysis of multiple data sets from a wide variety of polymer nanocomposite materials, we showed that these characteristic gamma distribution parameters are related to the degree of dispersion according to the expression: $\alpha + 0.05\beta = \delta$, with $\delta$ as a dispersion index able to distinguish among different dispersion states. Specifically, from the data sets used in the analysis, we observed that: $\delta < 5$ for exfoliated composites, $5 < \delta < 6.5$ for less exfoliated composites with stacks containing several layers, and $\delta > 6.5$ for intercalated composites.

At last, we confirmed the proposed method with independent *experiments* involving two nanocomposites with different morphologies synthesized in our lab. This methodology can be used to establish inference models for implementing

effective online control of nanocomposites' end-use properties. Some preliminary work relating to the inference models are presented in Appendix C. Other applications of this method of quantifying clay dispersion are discussed in Chapter 8.

# Chapter 5

# CONTROL SYSTEM DESIGN AND IMPLEMENTATION I: PROCESS OUTPUT VARIABLES

## 5.1 Introduction

As discussed in Chapter 2, the proposed control scheme has a multiple-loop structure with a controller at each cascading level: (i) the innermost loop with controller $C_1$ for controlling process outputs, $y$, by adjusting manipulated variables, $u$, (ii) the outer loop with controller $C_2$ for regulating the product end-use properties, $w$, by manipulating the process outputs, $y$, and (iii) the outermost loop with controller $C_3$ for improving customer satisfaction by translating customer feedback data, $z$, into appropriate set-points for end-use properties, $w$. In this scheme, the performance of an outer-level controller highly relies on the performance of the lower-level controllers. Therefore, the success of the overall control scheme requires an effective design of the controller at each level. (Note that manipulated variables, $u$, are regulated by standard Proportional-Integral (PI) controllers, which have already been tuned independently to ensure satisfactory performance, and no further discussion is needed for these controllers.) The design and implementation of these effective controllers are discussed in detail in the following three chapters (i.e., Chapter 5, Chapter 6, and Chapter 7).

This chapter is devoted to designing a high performance controller $C_1$ operated at the innermost level for rejecting unmeasured disturbances. Good understanding of the extrusion process will provide insights into the design of this controller. Typically,

the extrusion process is characterized by the following properties: It has multiple inputs and multiple outputs (MIMO process); the process variables must be constrained within certain regions to ensure safe and efficient operation of the process; the process variables interact strongly among themselves [120]. Because of these inherent characteristics, MIMO model-based predictive controller (MPC) should be more effective at the innermost level of the control scheme compared to conventional control strategies and is highly recommended by academia and industry [121]. In this chapter, we present the procedure for designing such an MPC and evaluating its performance by both simulation and experiment. First, we determine the controller structure and select the manipulated inputs $u$ and the process outputs $y$ in section 5.2. Then, the process model is identified to relate process outputs $y$ and the manipulated inputs $u$, and the identification procedure is presented in section 5.3. The details of the controller design are provides in section 5.4. The simulation study for the controller evaluation is discussed in section 5.5, and the controller is implemented experimentally on a pilot-scale extrusion process in section 5.6.

## 5.2 Controller Structure Design: Process Inputs and Outputs

The extrusion process in this work is based on a Coperion W&P ZSK-18mm co-rotating, intermeshing twin screw extruder, which was employed to manufacture masterbatches of polymer nanocomposites with 25 wt. % organoclay concentration. The polymer matrix is Na ionomer, and the reinforcement is a mixture of two organically modified clays, 20A and 93A.

As mentioned in section 3.6, the signals wired to the DAQ system are listed as follows: Na ionomer feed-rate, 20A feed-rate, 93A feed-rate, screw speed, motor power, die pressure, and exit melt temperature. Thus, the candidate process inputs are

Na ionomer feed-rate ($u_1$), 20A feed-rate ($u_2$), 93A feed-rate ($u_3$), screw speed ($u_4$), and the barrel temperatures ($u_5$) in the eight extruder zones. Also, the candidate process outputs are motor power ($y_1$), organoclay concentration ($y_2$), and 20A concentration ($y_3$), die pressure ($y_4$), and exit melt temperature ($y_5$). Of these, $y_2$ and $y_3$ are determined from the feed-rates of the polymer and organoclays, shown in Equations 5-1 and 5-2, respectively:

$$y_2 = \frac{u_2+u_3}{u_1+u_2+u_3} \quad 5\text{-}1$$

$$y_3 = \frac{u_2}{u_2+u_3} \quad 5\text{-}2$$

### 5.2.1 Selection of Process Inputs

The manipulated variables were determined based on a previous study and understanding on the given extrusion process [122]. As discussed in section 3.5, the screw speed does not affect the clay dispersion significantly, suggesting it is not a good manipulated variable. Also, because the dynamics of the process output responses to barrel temperature changes are much slower than the dynamics of the response to other input variables, there is no advantage to using the barrel temperatures as manipulated variables [97]. Therefore, Na ionomer feed-rate, 20A feed-rate, and 93A feed-rate were selected as the manipulated variables for the system.

### 5.2.2 Selection of Process Outputs

Compared to the selection of process inputs, the selection of process outputs was much more complicated and can be done by the following two steps: (i) screening the candidate controlled variables based on control requirements; and (ii) determining the controlled variables through system analysis.

Besides rejecting rampant unmeasured disturbances, the controller $C_1$ aims to maintain the organoclay concentration in the masterbatches at the desired level (i.e., $y_2$ = 25 wt. %), as well as to tracking the set-point of $y_3$ specified by the output of controller $C_2$ because the 20A concentration in the organoclay mixture is highly related to the clay dispersion (see sections 3.4.2 and 3.5). As a result, the process output variables $y_2$ and $y_3$ *must* be chosen as the controlled variables. Since the exit melt temperature does not have strong influence on the organoclay dispersion (see section 3.4.2), it is not considered as an appropriate control variable. Thus, the candidate controlled variables are now narrowed down to four variables: motor power, organoclay concentration, 20A concentration, and die pressure, among which organoclay concentration and 20A concentration *must* be under control.

Unfortunately, the system is now under-defined with three input variables and four output variables. Since it is impossible to control four variables by three manipulated variables independently, we have to choose the third controlled output from motor power and die pressure. We approach this problem by subdividing the available outputs into two candidate output subsets, listed in Table 5-1, from which more appropriate subset will be chosen.

Table 5-1: Two candidate output sets for the process

| Set No. | Candidate controlled variables |
|---|---|
| 1 | motor power, organoclay concentration , and 20A concentration |
| 2 | die pressure, organoclay concentration , and 20A concentration |

To tackle the output selection problem, the steady-state gain matrix needs be obtained first, based on which several methods such as non-square relative gain array (NRGA) and singular value decomposition (SVD) will be employed.

The steady-state gain matrix was obtained by implementing a series of independent step changes in the manipulated variables at the nominal operating condition (Table 5-2), where the operating condition was determined previously in section 3.5. The gain matrix was then scaled by the following rule: The input data for each input variables were scaled by the maximum introduced changes while the output responses were scaled by the maximal measurements; and the resulting scaled gain matrix is shown in Table 5-3.

Table 5-2: Step changes implemented at the operating conditions

| Step change (lb/h) | Ionomer feed-rate $u_1$ (lb/h) | 20A feed-rate $u_2$ (lb/h) | 93A feed-rate $u_3$ (lb/h) | Organoclay conc. $y_2$ (wt. %) | 20A conc. $y_3$ (%) |
|---|---|---|---|---|---|
| $u_1$: 8 – 4 | 8 – 4 | 1.4 | 0.60 | 20 – 30 | 70 |
| $u_2$: 2.4 – 0.4 | 6 | 2.4 – 0.4 | 0.60 | 33 – 14 | 80 – 40 |
| $u_3$:0.75 – 0.45 | 6 | 1.4 | 0.75 – 0.45 | 26 – 24 | 65 – 76 |

Table 5-3: Results of step change experiments: full scaled gain matrix **G**

| O/I | Ionomer feed-rate $u_1$ | 20A feed-rate $u_2$ | 93A feed-rate $u_3$ |
|---|---|---|---|
| Motor power $y_1$ | 0.7089 | 0.6161 | -0.0240 |
| Organoclay conc. $y_2$ | -0.3951 | 0.5868 | 0.0888 |
| 20A conc. $y_3$ | 0.0000 | 0.5170 | -0.1147 |
| Die pressure $y_4$ | -0.3016 | 0.9214 | -0.0668 |

*Non-square Relative Gain Array Analysis*

Since the number of inputs is not equal to the number of outputs, the relative gain array (RGA) of the system is a non-square RGA (NRGA), which can be computed as follows:

$$\boldsymbol{\Lambda}(\boldsymbol{G}) = \boldsymbol{G} \otimes (\boldsymbol{G}^{\dagger})^{T}$$

$$\boldsymbol{G}^{\dagger} = (\boldsymbol{G}^{T}\boldsymbol{G})^{-1}\boldsymbol{G}^{T} \qquad 5\text{-}3$$

where $\boldsymbol{G}$ is the full scaled gain matrix, $\boldsymbol{G}^{\dagger}$ is the pseudo inverse of $\boldsymbol{G}$, and $\otimes$ is element-by-element product. The resulting NRGA is presented in Table 5-4.

Table 5-4: Non-square relative gain array (NRGA) and the row-sum of the NRGA

| O/I | Ionomer feed-rate $u_1$ | 20A feed-rate $u_2$ | 93A feed-rate $u_3$ | Row-sum of NRGA |
|---|---|---|---|---|
| Motor power $y_1$ | 0.7587 | 0.2848 | -0.0449 | 0.9987 |
| Organoclay conc. $y_2$ | 0.1082 | 0.3072 | 0.4214 | 0.8368 |
| 20A conc. $y_3$ | 0.0000 | 0.0389 | 0.5020 | 0.5409 |
| Die pressure $y_4$ | 0.1330 | 0.3692 | 0.1214 | 0.6236 |

The selection criterion is that the output which corresponds to the row with the smallest sum can be eliminated [123]. In the specific case of the experimental system under consideration, organoclay concentration and 20A concentration must be under control; as a result, the organoclay concentration cannot be eliminated although it corresponds to the smallest row-sum of the NRGA. Comparing the sum of the first row, corresponding to motor power, to the sum of the forth row, corresponding to die

pressure (see Table 5-4), it is reasonable to eliminate die pressure from the acceptable output sets.

*Singular Value Decomposition Analysis*

Singular value decomposition (SVD) analysis was performed for each output set in Table 5-1, and the results for output set 1 and 2 are listed in Tables 5-5 and 5-6 respectively. The selection rule is that the candidate set of controlled outputs corresponding to the largest minimum singular value $\underline{\sigma}(\boldsymbol{G})$ is the most effective set. According to Tables 5-5 and 5-6 minimum singular values $\underline{\sigma}(\boldsymbol{G})$ for output sets 1 and 2 are 0.1317 and 0.0162, respectively; and the condition number $\kappa$, the ratio of the largest to the smallest singular value, is much larger for candidate set 2 than for candidate set 1. Therefore, output set 1 provides better condition and should be selected as the output variable, which coincides with the NRGA results. The results of NRGA and SVD analyses indicate that the first output set in Table 5-1 is a better choice.

Table 5-5: Singular value matrix and condition number $\kappa$ for output set 1

| O/I | Ionomer feed-rate $u_1$ | 20A feed-rate $u_2$ | 93A feed-rate $u_3$ |
|---|---|---|---|
| Motor power $y_1$ | 1.0443 | 0 | 0 |
| Organoclay conc. $y_2$ | 0 | 0.7507 | 0 |
| 20A conc. $y_3$ | 0 | 0 | 0.1317 |
| $\kappa = 7.9271$ | | | |

Table 5-6: Singular value matrix and condition number $\kappa$ for output set 2

| O/I | Ionomer feed-rate $u_1$ | 20A feed-rate $u_2$ | 93A feed-rate $u_3$ |
|---|---|---|---|
| Organoclay conc. $y_2$ | 1.2839 | 0 | 0 |
| 20A conc. $y_3$ | 0 | 0.2906 | 0 |
| Die pressure $y_4$ | 0 | 0 | 0.0162 |
| $\kappa = 79.3719$ | | | |

*Discussion: Motor Power and Dispersion Characteristics*

Another reason to selecting motor power as the controlled variable is based on the physical point of view. As a function of viscosity, motor power can be used to infer viscosity of the polymer nanocomposites. From the literature, the viscosity is related to the dispersion characteristics by the following equation [124].

$$\eta = f(\phi, \dot{\gamma}) \qquad 5\text{-}4$$

where $\phi$ represents the filler concentration, and $\dot{\gamma}$ is the shear rate. The parameter $\phi$ is often used to characterize the dispersion state of the polymer nanocomposites.

Therefore, one can use motor power, which is easier to measure compared to viscosity, to predict the dispersion characteristics. Based on measurements of motor power, we are able to infer the viscosity as well as the dispersion characteristics. This discussion provides physical support for selecting motor power as the controlled variable.

As a result, the output variables for the given system were determined as motor power, organoclay concentration, and 20A concentration. And the resulting system of interest is a 3 × 3 system with Na ionomer feed-rate, 20A feed-rate, and 93A feed-rate as the manipulated variables, $\boldsymbol{u}$, and motor power, organoclay concentration, and 20A concentration as the controlled variables, $\boldsymbol{y}$. Here, $\boldsymbol{u} = [u_1\ u_2\ u_3]^T$ and $\boldsymbol{y} = [y_1\ y_2\ y_3]^T$.

## 5.3 Process Model Identification

The process model relating the manipulated variables, $\boldsymbol{u}$, with the process outputs, $\boldsymbol{y}$, was identified by an empirical approach, which involves the collection of input-output data for modeling. The systematic procedure of this method consists of three major steps: (i) preliminary process test design, implementation, and analysis, (ii) final identification test design and collection of input-output data, and (iii) model development and validation.

### 5.3.1 Preliminary Tests

The rational design of an appropriate final identification test requires *à-priori* knowledge of the process. Such process knowledge was obtained by preliminary tests involving a series of step changes and staircase changes in the manipulated variables at the operating point. The step tests in the manipulated variables were used to estimate the process gains and the dominant time constant at the operating point, while the staircase tests were applied to check the non-linearity around the operating point.

Several step changes in the process inputs (Table 5-2) were performed. Table 5-7 shows the estimated process gains matrix and the resulting RGA calculated from the gain matrix. As a measure of interaction, the RGA suggests that the $3 \times 3$ system is strongly interactive, which indicates that traditional single loop controllers will not be able to achieve effective control.

The SVD analysis was employed to study the conditioning of the $3 \times 3$ system. The process conditioning can be quantified by the condition number, the ratio between the gains in the strong and weak directions. The condition number for this system was

computed as 7.9, suggesting a well-conditioned process where the combinations of the inputs have fairly equal effects on the outputs (see Table 5-5).

Also, the process settling time of about 210 s was estimated by the step test data, which will be used for design of staircase tests and final identification tests.

Table 5-7: Results of step change experiments: scaled gain matrix and relative gain array for the 3 × 3 system

| Scaled gain matrix | | | |
|---|---|---|---|
| O/I | Ionomer feed-rate $u_1$ | 20A feed-rate $u_2$ | 93A feed-rate $u_3$ |
| Motor power $y_1$ | 0.7089 | 0.6161 | -0.0240 |
| Organoclay conc. $y_2$ | -0.3951 | 0.5868 | 0.0888 |
| 20A conc. $y_3$ | 0.0000 | 0.5170 | -0.1147 |
| Relative gain array | | | |
| O/I | Ionomer feed-rate $u_1$ | 20A feed-rate $u_2$ | 93A feed-rate $u_3$ |
| Motor power $y_1$ | 0.7587 | 0.2848 | -0.0449 |
| Organoclay conc. $y_2$ | 0.1082 | 0.3072 | 0.4214 |
| 20A conc. $y_3$ | 0.0000 | 0.0389 | 0.5020 |

Then, the non-linearity of the process needs to be studied for designing a good identification test. The staircase tests in the process inputs explore the process dynamics both above and below the operating point under consideration, so that it is an efficient tool to investigate the process non-linearity [122]. In this 3 × 3 system, the staircase test in Na ionomer feed-rate was designed based on the process settling time, shown in Figure 5-1. The results (right panel in Figure 5-1) illustrate that the process is reasonably linear around the operating condition under consideration.

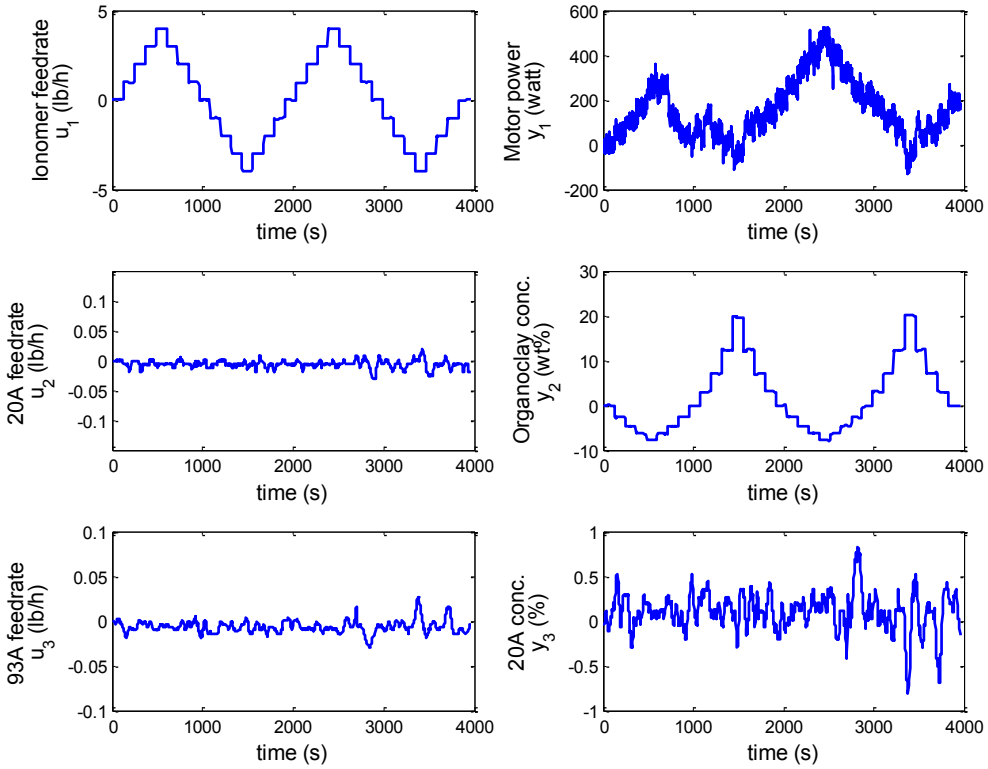


Figure 5-1: Results of Na ionomer feed-rate staircase change at the operating point under consideration

### 5.3.2 Final Identification Test

The results of the preliminary tests reveal that the extrusion process is approximately linear locally around the operating point under consideration. Thus, local linear models are suitable to characterize the process behavior at the operation point. To identify such linear models, the final identification tests consisting of suitable input excitations were designed and implemented.

The selection of the signals for the input excitation is the key to system identification. A persistently exciting sequence is required to excite the process over a wide range of frequency. Some studies used a random binary sequence (RBS) as the input excitation method [65, 72, 73]. However, this method has a relative low signal-to-noise ratio in some frequency ranges [122]. We chose the general binary noise (GBN) signals as the input excitation because they have better signal-to-noise ratio as well as excellent ability to excite the process over a wide range of frequency. The GBN signals, proposed by Tulleken [125], switch between two values $-a$ and $a$ according to the switching probability $p_{sw}$.

Guided by the design rules proposed by Zhu [122], the mean switching time of the GBN signal was chosen as 70 s, which is one third of the process settling time (210 s). The duration of the test (4000 s) was approximately 19 times the process settling time. Since the process of interest is fairly well-conditioned, the GNB signals for manipulated variables do not need to be correlated. Therefore, three uncorrelated GBN signals were implemented simultaneously in $u_1$, $u_2$, and $u_3$ at the operating point (see Figure 5-2).

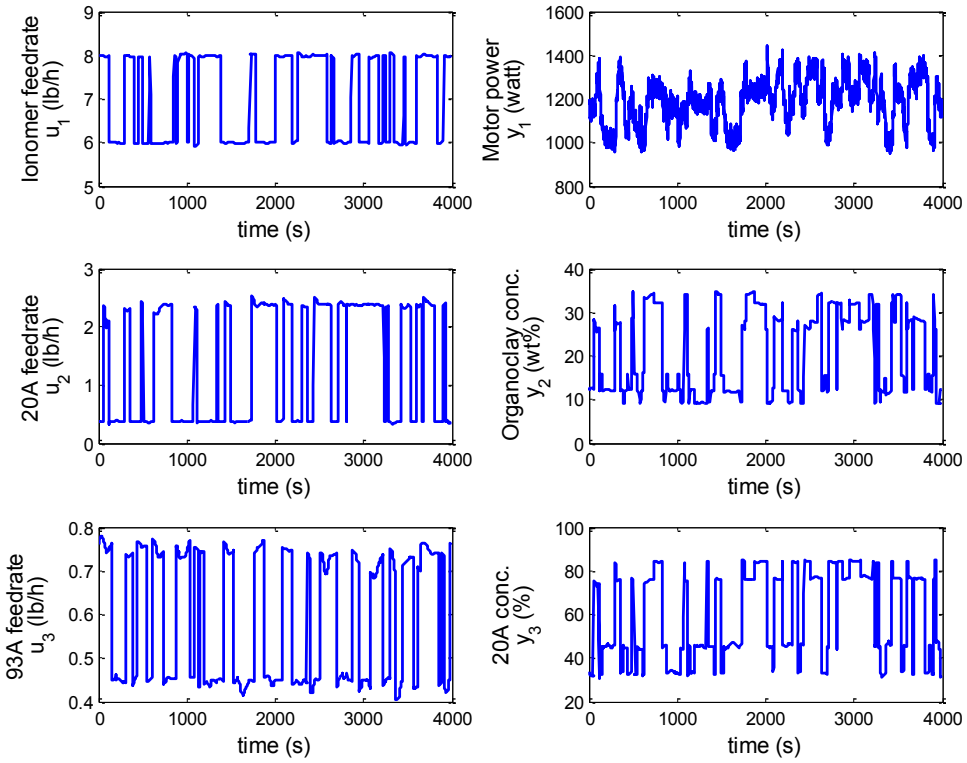


Figure 5-2: Results of uncorrelated general binary noise test signals at the operating point

### 5.3.3 Model Development and Validation

The candidate linear models and their structures are listed as follows:

1. Autoregressive moving average with exogenous inputs (ARMAX): A linear model where the disturbance is assumed to be a moving-average process. The structure of ARMAX model is shown as:

$$A(q)y(t) = B(q)u(t - n_{k1}) + C(q)e(t - n_{k2}) \quad 5\text{-}5$$

2. Box-Jenkins (BJ): A general linear model where the disturbance model dynamics behavior is assumed different from that of the system. The structure of BJ model is presented as:

$$y(t) = \frac{B(q)}{A(q)}u(t - n_{k1}) + \frac{C(q)}{D(q)}e(t - n_{k2}) \quad 5\text{-}6$$

where in both case, $q$ is the backshift operator, and $A(q)$, $B(q)$, $C(q)$, and $D(q)$ are polynomials of $q^{-1}$, represented as below:

$$A(q) = 1 + a_1q^{-1} + a_2q^{-2} + \cdots + a_{na}q^{-na}$$

$$B(q) = 1 + b_1q^{-1} + b_2q^{-2} + \cdots + b_{nb}q^{-nb}$$

$$C(q) = 1 + c_1q^{-1} + c_2q^{-2} + \cdots + c_{nc}q^{-nc}$$

$$D(q) = 1 + d_1q^{-1} + d_2q^{-2} + \cdots + d_{nd}q^{-nd}$$

We employed the so-called "cross-validation" technique to estimate the model parameters and select the model structures/orders because such a technique is able to avoid initialization errors [122]. This technique divides the data set obtained from the final identification test into two equal halves: the first half of the data set was used to develop the model, while the other half was used in validating the model. The parameters were estimated with the help of the System Identification Toolbox of MATLAB®. Model structures/orders were selected based on the normalized root mean square (NRMSE) measure of the goodness of the fit, which is defined as follows:

$$fit = 100(1 - \frac{\|y - y_{pred}\|}{\|y - y_{mean}\|}) \quad 5\text{-}7$$

The fit value is usually calculated by the *compare* function in the System Identification Toolbox of MATLAB®. Specifically, the higher the fit value is, the better the model fits the experimental data. Multiple-input single-output (MISO) BJ models provide the best fits to the measured data for motor power and 20A concentration, while for organoclay concentration, the MISO ARMAX model has the highest fit value. The model orders and their corresponding fit values are shown in Table 5-8, and Figure 5-3 shows the comparison between the data and model predictions.

Table 5-8: Identified BJ model structures for motor power and 20A concentration, $y_1$ and $y_3$, and ARMAX model structures for organoclay concentration, $y_2$

| Model type | | MISO model orders | | | | | Delay ($n_{d1}$, $n_{d2}$) | | | Best fit (%) |
|---|---|---|---|---|---|---|---|---|---|---|
| | O/I | $u_1$ ($n_a$, $n_b$) | $u_2$ ($n_a$, $n_b$) | $u_3$ ($n_a$, $n_b$) | Noise ($n_c$) | Noise ($n_d$) | $u_1$ | $u_2$ | $u_3$ | |
| BJ | $y_1$ | 5,3 | 5,3 | 5,3 | 2 | 1 | 1,1 | 1,1 | 1,1 | 70.87 |
| | $y_3$ | 2,2 | 2,2 | 2,2 | 0 | 0 | 0,0 | 0,0 | 0,0 | 83.37 |
| ARMAX | $y_2$ | 2,2 | 2,2 | 2,2 | 1 | / | 0,0 | 0,0 | 0,0 | 91.76 |

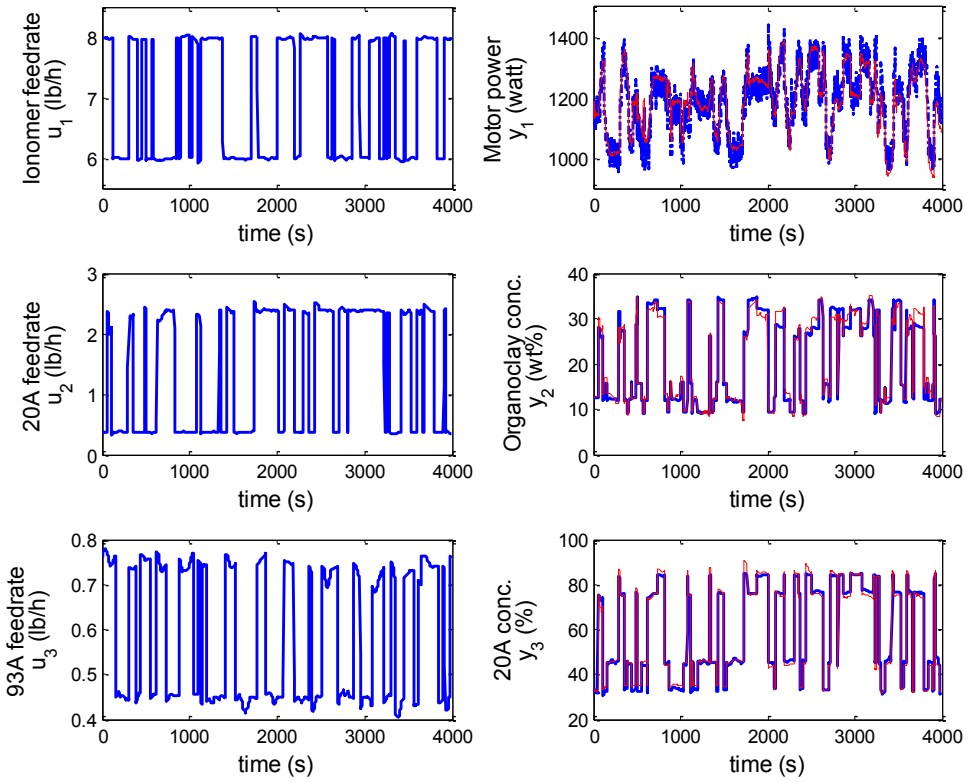


Figure 5-3: Identified MISO model fit to the output data in response to GBN input excitations. The fit values are 70.87% for motor power, 83.37% for organoclay concentration, and 91.76% for 20A concentration. The blue lines in the right-hand panels are the output responses, while the red lines are the model predictions

Although the fit values for the output responses $y_1$ and $y_2$ are not very high, they are good enough for effective model predictive control. These three MISO models (listed in Appendix C) constitute the final multiple-input multiple-output (MIMO) model which will be used for controller design.

It is worthwhile to note that the best fit models for motor power and 20A concentration are BJ models, whereas the best fit model for organoclay concentration is ARMAX model. The different model structures for the outputs reveal how the process outputs relate to the process inputs and the disturbances. The structure of the BJ model (Equations 5-6) shows that the denominator for the process model is distinct from the denominator for the noise model, indicating that the process inputs and the disturbances affect the output in different ways. On the other hand, the identical denominator for both the process and noise models in the ARMAX model (Equation 5-5) indicates that the process inputs and the disturbances contribute to the output in the same way.

Therefore, the outputs such as motor power and 20A concentration are affected by the process inputs and the disturbances via different dynamic behaviors, while organoclay concentration is influenced by the process inputs and the disturbances in the same way. These results are quiet reasonable and consistent with the intrinsic characteristics of the process outputs:

- Motor power: The disturbances that affect motor power include not only the input disturbances (e.g., fluctuations in the feed-rates occurring due to the rotations of the main and side hopper screws, and compositional and property variations in the polymer and organoclay feeds), but also the process disturbances (e.g., high frequency fluctuation due to screw rotation). Therefore, the sources of the dynamics of the inputs and disturbances are distinct, which corresponds to the conclusion that the BJ model is more suitable to capture the dynamics of the motor power.

- Organoclay concentration: As shown in Equation 5-1, the organoclay concentration is determined by three feed-rate inputs simultaneously. Thus, the disturbances that influence this output only consist of the input disturbances, which is consistent with the selection of ARMAX model for organoclay concentration.

- 20A concentration: The 20A concentration depends on the feed-rates of organoclays (see Equation 5-2), feeding from the side hopper. Therefore, the disturbances that affect this output are part of the input disturbances (e.g., fluctuation in the organoclay feed-rates occurring due to the rotation of the side stuffer screw, and compositional and property variations in organoclay feed). Since the disturbance sources are different from the sources of process inputs, the BJ model is a better choice for 20A concentration.

## 5.4 Controller Design

Since any fluctuations in the process variables can cause undesirable variations in the product quality, it is important to minimize the input and process disturbances. The objectives of controller $C_1$ is to reject these disturbances as well as to track the set-points for the process outputs determined by the outer loop controller $C_2$. A multivariable MPC is designed to achieve these goals (see Appendix E for theoretical support of using MPC).

The sample interval $t_s$ of the controller was first chosen as 10 s according to the following criterion:

$$\frac{T_{st}}{100} \leq t_s \leq \frac{T_{st}}{20} \qquad 5\text{-}8$$

where $T_{st}$ is the process settling time obtained from step test (see section 5.3.1).

Generally, the MPC algorithm consists of three basic elements: (i) prediction model, (ii) objective function, and (iii) obtaining the control law [126]. These elements for the innermost loop controller $C_1$ are discussed as follows.

1. The predictions for the process outputs are based on the empirical MIMO model (see section 5.3.3) with a discrete state-space formulation:

$$\begin{aligned} x(k+1) &= Ax(k) + Bu(k) + v_1(k) \\ y(k) &= Cx(k) + Du(k) + v_2(k) \end{aligned} \quad \text{5-9}$$

where $y$ is the vector of outputs, $u$ is the vector of inputs, and $x$ is the vector of states, and $v_1$ and $v_2$ are the noises affecting the process and the output, respectively.

2. The objective function has a quadratic form, shown as:

$$J = \sum_{j=1}^{p} \left[ y_{k+j}^T Q y_{k+j} + u_{k+j}^T R u_{k+j} \right] \quad \text{5-10}$$

Here, $Q$ and $R$ are diagonal weighting matrices, $k$ is the sampling instant, and $p$ is the prediction horizon.

3. The control action $u(t)$ is computed by minimizing the objective function $J$ in Equation 5-10 at each time interval $k$, subjecting to the following constraints:

$$\begin{bmatrix} u_{min}(k|k) \\ u_{min}(k+1|k) \\ \vdots \\ u_{min}(k+m-1|k) \end{bmatrix} \leq \begin{bmatrix} u(k|k) \\ u(k+1|k) \\ \vdots \\ u(k+m-1|k) \end{bmatrix} \leq \begin{bmatrix} u_{max}(k|k) \\ u_{max}(k+1|k) \\ \vdots \\ u_{max}(k+m-1|k) \end{bmatrix} \quad \text{5-11}$$

$$\begin{bmatrix} y_{min}(k|k) \\ y_{min}(k+1|k) \\ \vdots \\ y_{min}(k+m-1|k) \end{bmatrix} \leq \begin{bmatrix} y(k|k) \\ y(k+1|k) \\ \vdots \\ y(k+m-1|k) \end{bmatrix} \leq \begin{bmatrix} y_{max}(k|k) \\ y_{max}(k+1|k) \\ \vdots \\ y_{max}(k+m-1|k) \end{bmatrix} \quad \text{5-12}$$

where $m$ is the control horizon. Constraints for the inputs and outputs were selected to ensure the process is operated in the safe region. Also, as in the standard MPC algorithm, the receding strategy is employed: Only the first element of the vector $u(t)$ is applied, rejecting the rest and repeating the optimization procedure at the next sampling instant.

## 5.5 Controller Implementation: Simulation Study

The controller $C_1$ performance was evaluated first in simulation to tune the MPC parameters for satisfactory set-point tracking and disturbance rejection. The tuning parameters, shown in Table 5-9, were determined based on the tradeoff between fast controller action and the stability of the process. The weights for all the manipulated variables were chosen to for a mediate aggressive control action (see weighing matrix $R$). In addition, the weights for $y_2$ and $y_3$ were selected to be much higher than $y_1$ (see weighing matrix $Q$), because it is important to maintain the organoclay concentration at the desired value ($y_2$ = 25 wt. %) and the 20A concentration is strongly related to the clay dispersion as well as the end-use properties. The constraints were selected to ensure that the process is operated in a stable and safe fashion.

Table 5-9: MPC parameters used in the simulation

| MPC parameter | Value |
|---|---|
| Input weight matrix $R$ | diag[3 1 1] |
| Output weight matrix $Q$ | diag[0.5 50 50] |
| Control horizon | 250 s |
| Prediction horizon | 500 s |
| Input constraints | $u_1$: [2 10] (lb/h) |
| | $u_2$: [0.1 3] (lb/h) |
| | $u_3$: [0.10 0.8] (lb/h) |
| Output constraints | $y_1$: [700 1600] (watt) |
| | $y_2$: [20 30] (wt. %) |
| | $y_3$: [60 90] (%) |

In the simulation, we introduced 5% plant–model mismatch such that the state-space matrices of the plant model was obtained by multiplying corresponding matrices of the prediction model by 0.95. To evaluate the controller performance on set-point tracking and disturbance rejection, we implemented a set-point change in each process output at $t = 0$ and step disturbances in $y_1$ at $t = 1000$ s. Note that no step disturbances were introduced in the concentration variables ($y_2$ and $y_3$), because step disturbances are not feasible for $y_2$ and $y_3$. Since the disturbances associated with $y_2$ and $y_3$ are input disturbances, introducing step disturbances must deliberately change the input variables and maintain these changes in the manipulative variables, which will lead to no control actions for the controller $C_1$.

The simulation results are presented in Figure 5-4, which shows that while the controller is able to follow the set-point changes in $y_2$, it cannot eliminate the offsets in $y_1$ and $y_3$. These offsets can be explained by the following reason: In principle, in this $3 \times 3$ system, three manipulated inputs, $u_1$, $u_2$, and $u_3$, are used to control three process outputs, $y_1$, $y_2$, and $y_3$. However, due to the fact that $y_2 = (u_2 + u_3) / (u_1 + u_2 + u_3)$ and $y_3 = u_3 / (u_2 + u_3)$, there is only one truly independent manipulated variable. With the loss of two degree of freedoms, only one of the three output variables can be driven independently to an arbitrary set-point. Moreover, the offset in $y_1$ (~ 10 watt) is larger than the offset in $y_3$ (< 1%). This observation results from the choice of the output weighting matrix $Q$ (Table 5-9). Since more weight was imposed on $y_3$ than $y_1$, the $Q$ matrix leads to less offset in $y_3$ than in $y_1$.

Although offsets are present in $y_1$ and $y_3$, it may not have a significant effect on the performance of the overall control scheme, because the outer loop controller $C_2$ is able to compensate for the offsets.

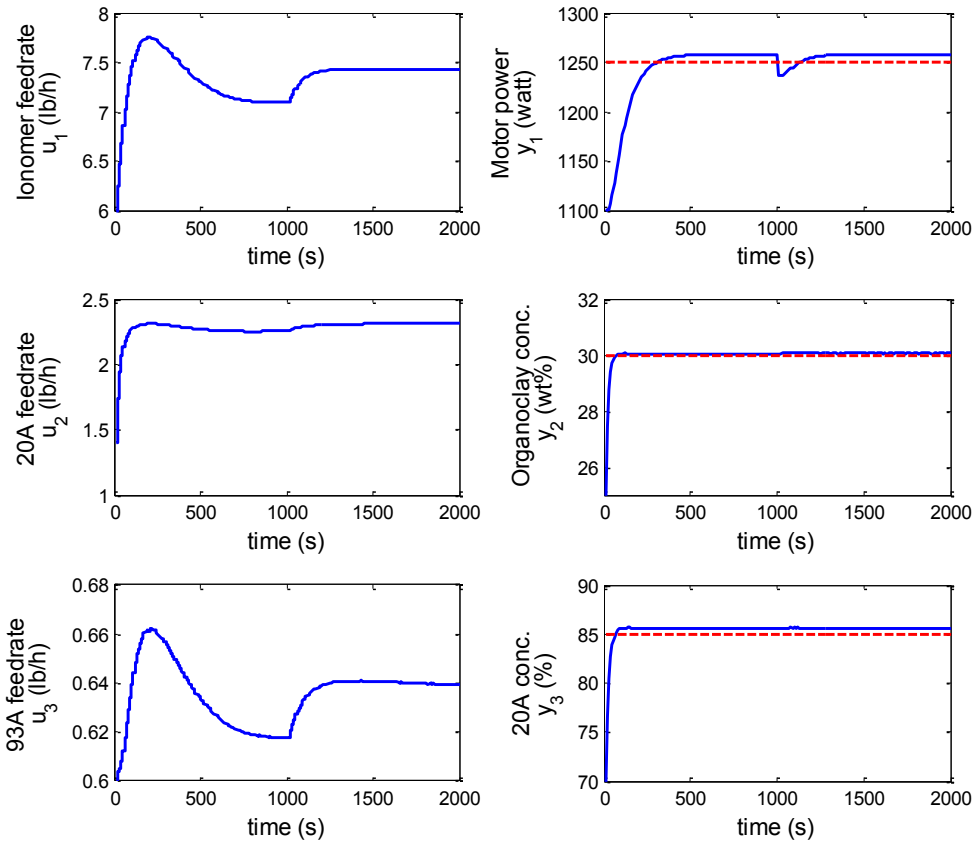


Figure 5-4: Controller $C_1$ performance: simulation results for set-point tracking and disturbance rejection. The dashed lines in the right-hand panels represent the set-points, and the solid lines represent the process outputs

## 5.6 Controller Experimental Implementation

### 5.6.1 Hardware–Software Implementation Scheme

Online implementation of the control scheme on a real process requires an interface between the process and the computer, where the real-time measurements are acquired from the hardware of the process (in our case using the DAQ hardware), and the optimal control actions are calculated by the computer and implemented within predesigned control interval (10 s). Therefore, a hierarchical strategy [127], shown in Figure 5-5, was employed to implement controller $C_1$ on the pilot-scale twin screw extruder process described in section 3.6, where a "hardware controller" acts the interface to the on-line control algorithms. The hardware controller is responsible for acquiring sensor signals from the DAQ hardware, translating the sensor signals (e.g., current/voltage) to real values (e.g., motor power and feed-rates), sending them to mathematical software for control action computation, and converting them back to sensor signals, which are then sent back to the DAQ hardware for implementation on the process.

In this study, we realized such a hardware controller using LabVIEW®. The control algorithm was executed in the Matlab® script of LabVIEW® by taking advantage of the LabVIEW® Active interface with Matlab®. Besides, the "timed" loop was employed to implement the control action within the control interval.

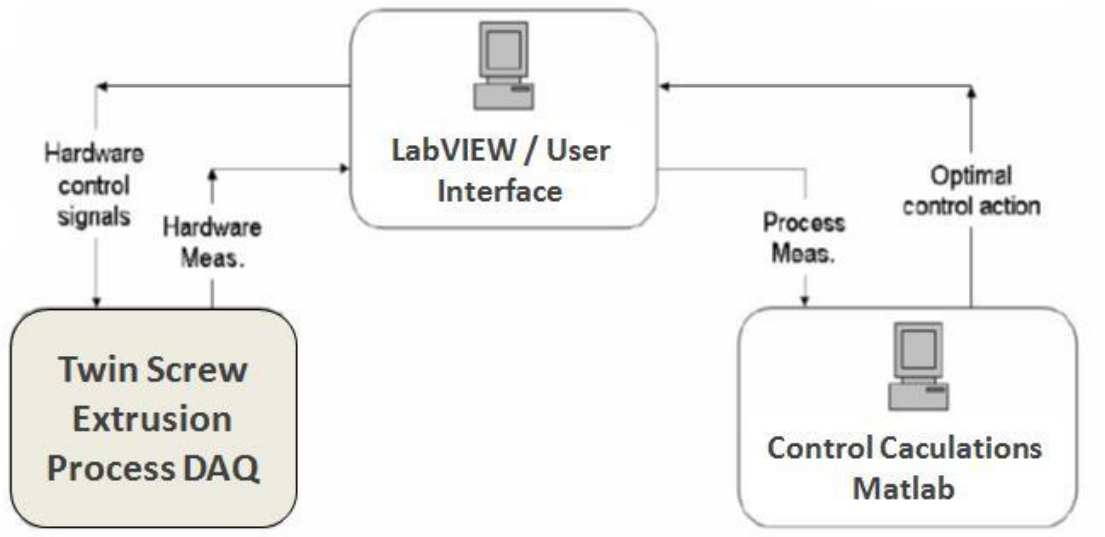


Figure 5-5: Labview–Matlab interface for experimental implementation of controller $C_1$ on a pilot-scale twin screw extrusion process [39]

### 5.6.2 Experimental Results

The basic control scheme designed and simulated in the previous part of this chapter was implemented on an experimental extrusion process, and its performance in set-point tracking was evaluated under the conditions in Table 5-10. Beginning from the baseline conditions, a step change was made in the desired set-point value of $y_1$ and $y_3$, while $y_2$ was kept constant because it is important to maintain the organoclay concentration in masterbatches at the desired value ($y_2$ = 25 wt. %).

Table 5-10: Process output variable baseline and set-points used in the experiment

| | Motor power $y_1$ (Watt) | Organoclay conc. $y_2$ (wt. %) | 20A conc. $y_3$ (%) |
|---|---|---|---|
| Baseline | 1100 | 25 | 70 |
| Set-points | 1300 | 25 | 75 |

The performance of the basic control system is shown in Figure 5-6, where the tuning parameters for controller $C_1$ is modified as following for ensuring a stable process: $R$ = diag[1 1 1]; $Q$ = diag[0.05 5 10]. The right-hand panel shows that the controller $C_1$ is able to track the set-points of motor power and 20A concentration with some offsets while maintain the organoclay concentration essentially constant. As we discussed in the previous section, the control system only have one degree of freedom, which cannot lead to completely offset-free set-point tracking for all the three process output variables.

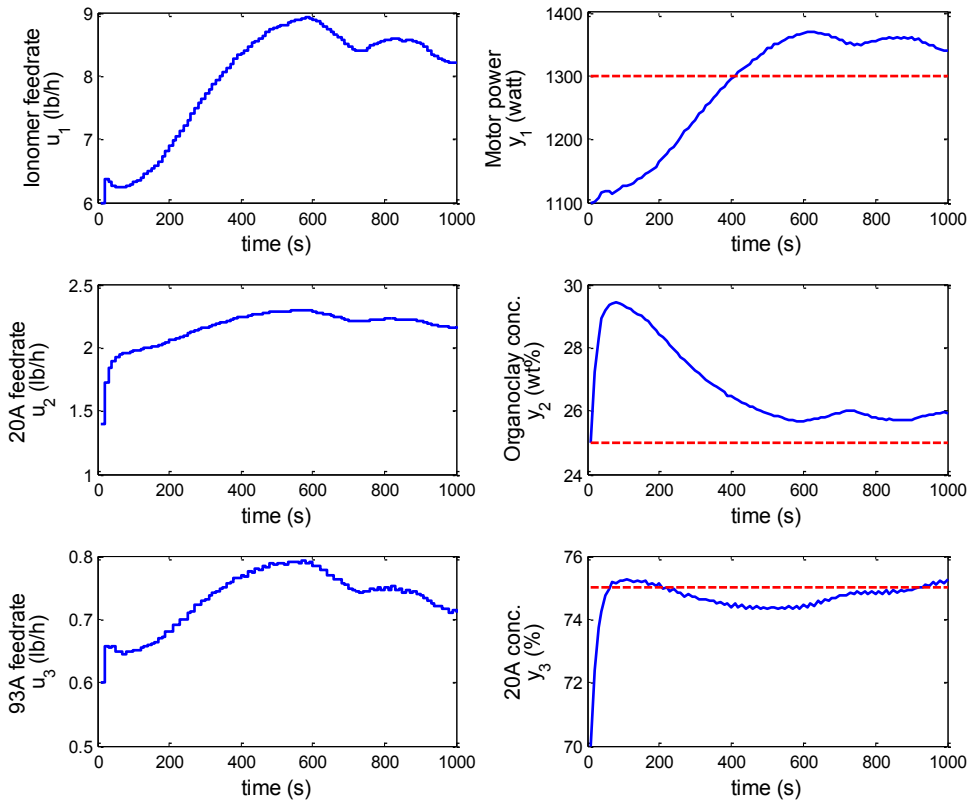


Figure 5-6: Controller $C_1$ performance on the experimental pilot-scale extruder: responses under conditions listed in Table 5-10

## 5.7 Conclusions

This chapter presented a MIMO model predictive control strategy for the innermost controller $C_1$ and demonstrated its performance both in the simulation environment and on a pilot-scale extrusion system. The key features of the controller $C_1$ are listed as follows:

1. The controller structure was determined to be a $3 \times 3$ system with Na ionomer feed-rate, 20A feed-rate, and 93A feed-rate as its manipulative variables and motor power, organoclay concentration, and 20A concentration as its controlled variables.

2. A MIMO model consisting of three MISO linear models was identified for predicting the process behavior. The idea of using linear models for the extrusion process was motivated by the fact that this process is reasonably linear around the operating point.

3. Base on the identified MIMO model, a model predictive controller with constraints was designed and appropriately tuned to ensure the set-point tracking for important process outputs such as organoclay concentration and 20A concentration.

The results of both simulation and experimental study show satisfactory controller performance on set-point tracing and disturbance rejection. Although offsets are present in motor power and 20A concentration, this will not significantly sabotage the performance of the overall control scheme since an outer-level multivariate controller $C_2$ will be designed (see Chapter 6) to enable effective control of end-use properties.

# Chapter 6

# CONTROL SYSTEM DESIGN AND IMPLEMENTATION II: PRODUCT END-USE PROPERTIES

## 6.1 Introduction

The traditional control strategy, discussed in the previous chapter, employs process outputs as the indicators of product end-use properties; however, these strategies is inadequate to ensure the attainment of products with desired end-use properties, because the process variables are only surrogate indicators of the end-use characteristics. As more direct indicators of these properties, product quality variables were regulated in several recent studies [66, 69], but this is still not sufficient to guarantee that the manufactured products will meet end-use property specification. To achieve customer requirements of acceptable performance products, it is critical to extend the basic control scheme of regulating process outputs to advanced control scheme explicitly involving the control of end-use properties.

In this chapter, we present such an advanced control scheme for regulating product end-use properties explicitly and efficiently. We first discuss the model, $M_{yw}$, relating end-use properties, $\boldsymbol{w}$, to the process outputs, $\boldsymbol{y}$, in section 6.2.1. Based on the model, a MIMO model predictive controller $C_2$ is designed and implemented together with the innermost loop controller $C_1$ in simulation in sections 6.2.2 and 6.3, respectively.

## 6.2 Controller Design

The purpose of controller $C_2$ is to follow the set-points of end-use properties by manipulating the set-points for the process outputs, which are then tracked by the innermost loop controller $C_1$. As discussed in Chapter 3, for the illustrative extrusion process, the end-use properties of interest are secant modulus, $w_1$, and elongation at break, $w_2$, which naturally are the controlled variables of this controller. Since it is desirable to keep the clay concentration constant in the masterbatches, process output variable $y_2$ cannot be selected as the input. Thus, the input variables of controller $C_2$ are motor power, $y_1$, and 20A concentration, $y_3$. Because the model predictive controllers are efficient in handling multivariable and constrained processes, the controller $C_2$ is also designed as a model predictive controller.

### 6.2.1 Model Development

The model, $M_{yw}$, used for predicting end-use properties, $w_1$ and $w_2$, by process outputs, $y_1$ and $y_3$, is expected to be a linear model (see Equations 6-1 and 6-2) without dynamics due to the slow rate of obtaining product property measurements. The model parameters were obtained from the data of step changes in process outputs, shown in Table 6-1.

$$\boldsymbol{w} = \boldsymbol{K}\boldsymbol{y} + \boldsymbol{b} \tag{6-1}$$

where , $\boldsymbol{w} = [w_1\ w_2]^T$, $\boldsymbol{y} = [y_1\ y_3]^T$, and

$$\boldsymbol{K} = \begin{pmatrix} 0.019 & 1.76 \\ -0.0188 & -2.62 \end{pmatrix}; \boldsymbol{b} = \begin{pmatrix} 94.9 \\ 440 \end{pmatrix} \tag{6-2}$$

Table 6-1: Experimental results of step changes implemented in motor power and 20A concentration

| No. | Inputs of controller $C_2$ | | Outputs of controller $C_2$ | |
|---|---|---|---|---|
| | Motor power $y_1$ (Watt) | 20A conc. $y_3$ (%) | Secant modulus $w_1$ (MPa) | Elongation at break $w_2$ (%) |
| 1 | 1376.59 | 80 | 266.78 | 199.29 |
| 2 | 1208.10 | 80 | 257.16 | 210.01 |
| 3 | 1068.44 | 80 | 254.34 | 208.99 |
| 4 | 1293.45 | 70 | 243.95 | 228.31 |
| 5 | 1154.38 | 70 | 233.29 | 239.84 |
| 6 | 1012.34 | 70 | 238.59 | 248.27 |
| 7 | 1214.03 | 60 | 219.29 | 270.86 |
| 8 | 1106.82 | 60 | 222.52 | 260.57 |
| 9 | 986.76 | 60 | 224.36 | 250.63 |

The gain matrix $\boldsymbol{K}$ of the model reveals important physics of the relationship between '$\boldsymbol{w}$' and '$\boldsymbol{y}$'. For example, secant modulus and elongation of break are negatively correlated (opposite signs in the columns of $\boldsymbol{K}$), and the secant modulus is improved as the 20A concentration increases, whereas the elongation at break is deteriorated with increased 20A clay composition. Also, note that $y_3$ affects the end-use properties more significantly than $y_1$ (larger values in the second column of the gain matrix compared to the values in the first column). Therefore, from intuition, these observations indicate that even a perfect tuned controller cannot improve the secant modulus and the elongation at break spontaneously (see section 6.3).

The model predictions and actual measurements are shown in Figure 6-1. Although not perfect correlation between '$\boldsymbol{w}$' and '$\boldsymbol{y}$' was observed, the model is able to provide a reasonable prediction of the properties, which is therefore sufficient enough for designing and implementing the controller.

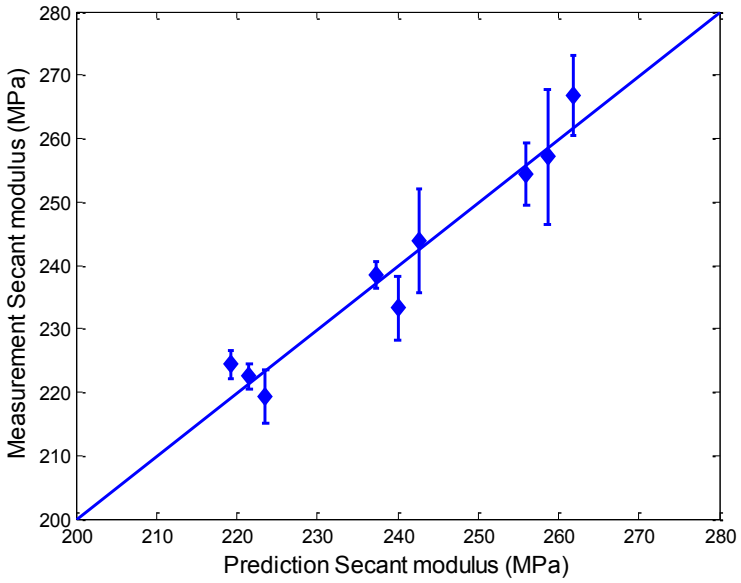


(a)

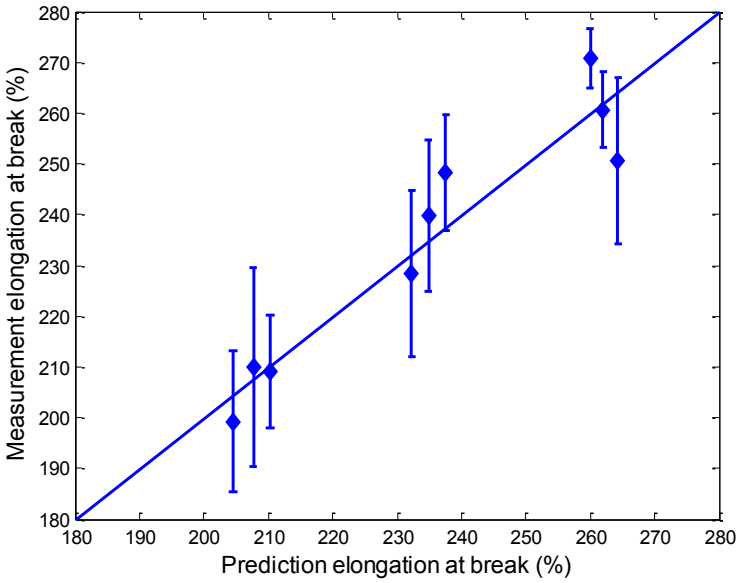


(b)

Figure 6-1: Model $M_{yw}$ predictions and measurements of (a). secant modulus; (b). elongation at break. The solid lines are the Y = X lines. Error bars represent the 95% confidence intervals obtained by five samples for each point

### 6.2.2 Model Predictive Control

The outer loop controller $C_2$ is also implemented as a model predictive controller with characteristics listed below:

1. Since no inference models are used to provide the estimates of end-use properties at a faster rate, the controller is implemented at a much slower rate (i.e., the rate of obtaining property measurements), which is 5000 s (~ 1.4 h). The sampling time of this loop is selected based on the criteria proposed in Appendix F.

2. A plant–model mismatch is introduced by multiple 0.95 to each parameter in the model.

3. The control action $y(t)$ is computed by minimizing the objective function $J$:

$$J = \sum_{j=1}^{p}\left[w_{k+j}^{T} Q w_{k+j} + y_{k+j}^{T} R y_{k+j}\right] \quad 6\text{-}3$$

subject to the following constraints:

$$\begin{bmatrix} y_{min}(k|k) \\ y_{min}(k+1|k) \\ \vdots \\ y_{min}(k+m-1|k) \end{bmatrix} \leq \begin{bmatrix} y(k|k) \\ y(k+1|k) \\ \vdots \\ y(k+m-1|k) \end{bmatrix} \leq \begin{bmatrix} y_{max}(k|k) \\ y_{max}(k+1|k) \\ \vdots \\ y_{max}(k+m-1|k) \end{bmatrix} \quad 6\text{-}4$$

$$\begin{bmatrix} w_{min}(k|k) \\ w_{min}(k+1|k) \\ \vdots \\ w_{min}(k+m-1|k) \end{bmatrix} \leq \begin{bmatrix} w(k|k) \\ w(k+1|k) \\ \vdots \\ w(k+m-1|k) \end{bmatrix} \leq \begin{bmatrix} w_{max}(k|k) \\ w_{max}(k+1|k) \\ \vdots \\ w_{max}(k+m-1|k) \end{bmatrix} \quad 6\text{-}5$$

where, $\boldsymbol{w} = [w_1\ w_2]^T$, $\boldsymbol{y} = [y_1\ y_3]^T$, $Q$ and $R$ are diagonal weighting matrices, $k$ is the sampling instant, $m$ is the control horizon, and $p$ is the prediction horizon. As in the standard MPC algorithm, the receding strategy is employed: Only the first element of the vector $y(t)$ is applied, rejecting the rest and repeating the optimization procedure at the next sampling instant.

## 6.3 Controller Implementation in Simulation

The performance of the control scheme involving controllers $C_1$ and $C_2$ was evaluated in simulation using the conditions shown in Table 6-2. In simulation I, a step increase is made in secant modulus simultaneously with step decreased in elongation at break. In simulation II, simultaneous step increases are made in both secant modulus and elongation at break. In both simulations, the innermost loop controller $C_1$ was implemented as designed in section 5.5. The prediction horizon was selected as 69.40 h, and the control horizon was at 23.13 h. The tuning parameters for controller $C_2$ are listed below: $Q$ = diag[50 800]; $R$ = diag[0 0].

Table 6-2: Product property baseline and set-points used in simulations

| | Secant modulus $w_1$ (MPa) | Elongation at break $w_2$ (%) |
|---|---|---|
| Baseline | 238.61 | 238.81 |
| Simulation I: set-points | 223.61 | 253.81 |
| Simulation II: set-points | 253.61 | 253.81 |

The results of simulation I are shown in Figure 6-2, where it can be seen, from the right-hand panel, that controller $C_2$ is able to track the end-use property set-points with small offsets. The performance of controller $C_1$ can be observed in the left-hand panel. As expected from the discussion in the previous chapter about the performance of controller $C_1$, offsets are presented in both $y_1$ and $y_3$, and the offset in $y_3$ is smaller than that is in $y_1$. These offsets in the process outputs act as the disturbances of controller $C_2$, which contribute to the offsets in the end-use properties.

As discussed in the previous section, the model, $M_{yw}$, indicates that not arbitrarily set-points of $w_1$ and $w_2$ can be tracked efficiently: The controller cannot improve both of the end-use properties spontaneously due to the physics of the nanocomposites, where decreased 20A composition in the clay blend deteriorates the secant modulus while enhances the elongation at break (see Chapter 3). This point is buttressed by the results of simulation II, shown in Figure 6-3. The objective of this simulation is to follow the positive step changes in secant modulus and elongation at break spontaneously. However, this objective is physically impossible (see section 6.2.1). Therefore, it is not surprising that, as presented in Figure 6-3, the elongation at break increases whereas the secant modulus decreases a little (see right-hand panel) as the 20A concentration decreases (see left-hand panel). Also, $y_1$ and $y_3$ present large offsets, which are due to that the feed-rate of 93A (input of innermost loop controller $C_1$) has reached its physical limit.

Further, note that the controller $C_2$ took almost 10 h to reach the desired set-points for the end-use properties. This observation indicates that it is necessary to incorporate inference models to improve the controller performance as well as realize on-line control of the properties.

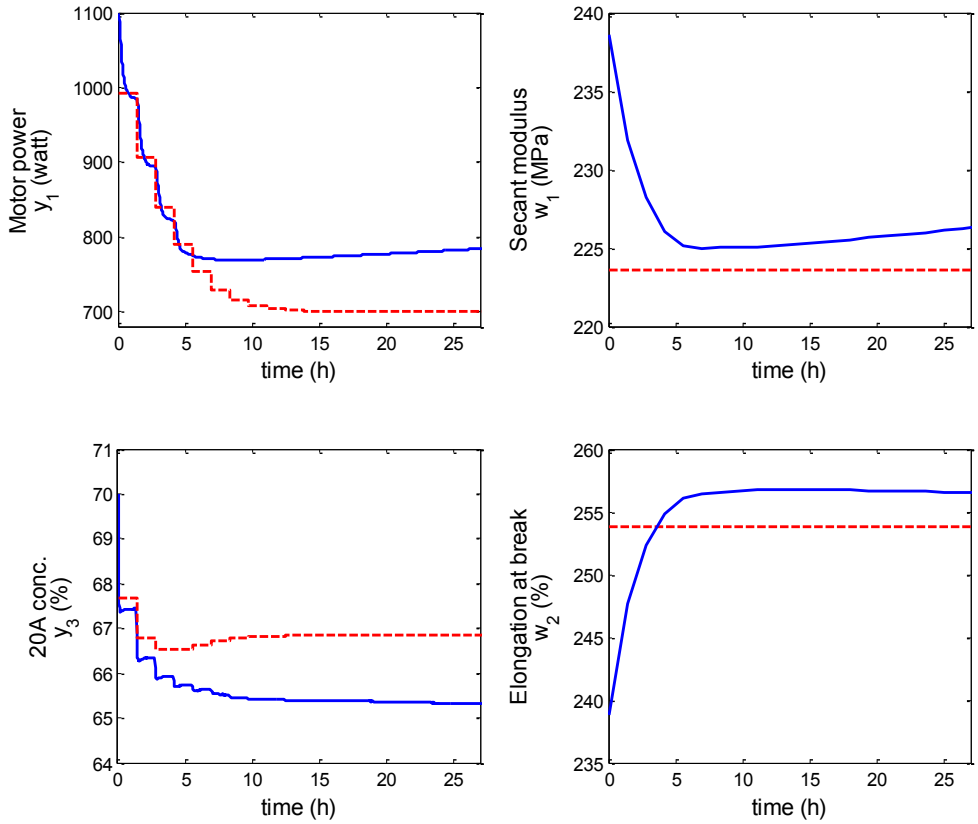


Figure 6-2: The performance of the control scheme involving controllers $C_1$ and $C_2$ for simulation I in Table 6-2. The dashed lines represent the ***y/w*** set-points, while the solid lines represent the ***y/w*** measurements

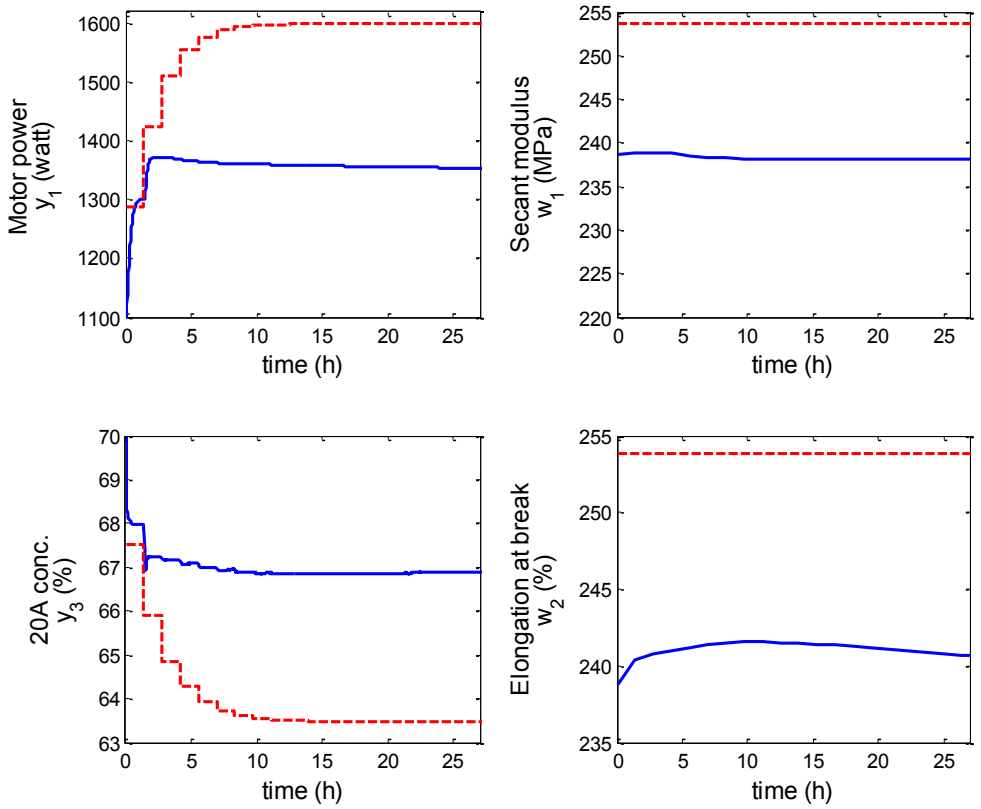


Figure 6-3: The performance of the control scheme involving controllers $C_1$ and $C_2$ for simulation II in Table 6-2. The dashed lines represent the ***y/w*** set-points, while the solid lines represent the ***y/w*** measurements

## 6.4 Conclusions

This chapter discusses the controller design and implementation of the outer loop controller $C_2$ for regulating product end-use properties. A steady-state model was developed to relate the end-use properties with process output variables. Based on this model, we designed controller $C_2$ as a MIMO model predictive controller. The simulations performed in this chapter buttress the physics of the process, where the controller cannot improve the secant modulus and elongation at break simultaneously. The results also show that inference models are required to improve the controller performance and realize on-line control of these infrequently available properties.

# Chapter 7

# CONTROL SYSTEM DESIGN AND IMPLEMENTATION III: CUSTOMER FEEDBACK CONTROLLER REGULATOR

## 7.1 Introduction

The control scheme discussed thus far not only involves a controller $C_1$ for process variable regulation (e.g., motor power, organoclay concentration, and 20A concentration), but also incorporates a controller $C_2$ for product end-use property regulation explicitly (e.g., tensile strength and toughness). However, the product end-use properties are only surrogate indicators of the product end-use performance characteristics. Therefore, even under perfect implementation of such a control scheme, there can be no guarantee product performance in end-use will be precisely as required by the customer. Especially with products tailored for specific applications, it is essential to incorporate actual customer feedback on product performance into the overall control scheme.

The objective therefore is to develop a scheme whereby customer feedback on product performance – whether the product performed acceptable as desired or not — is used explicitly to take rational corrective action if the product does not perform in end-use precisely as designed. Such a scheme is illustrated in Figure 7-1 where the binary customer feedback information, $z$ ($z = 1$ when the product performs in end-use precisely as designed, and $z = 0$ otherwise) is used to determine appropriate set point $\boldsymbol{w}^*$ for the product quality attributes. To accomplish this objective, we design and implement, for the first time, a customer feedback regulator $C_3$ which is illustrated by

our specific example of manufacturing polymer nanocomposites for a packaging film application. Some theoretical study relating to the characteristics of the regulator (e.g., achievable probability of acceptance) is also discussed in this chapter.

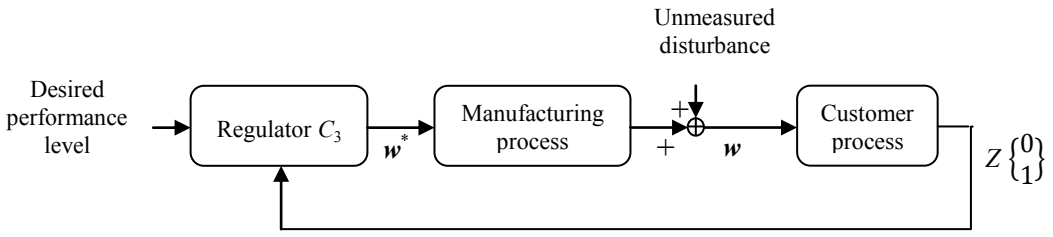


Figure 7-1: The customer feedback control scheme. The inner two loops involving process variable control and end-us property control are considered as the manufacturing process

## 7.2 Product Quality Specifications

Manufactured products are accepted by end-use customers only when their product quality attributes (e.g., for packaging films: tensile strength, toughness (represented by elongation at break), tear strength, etc.) lie within a specific range of values. Table 7-1 shows a typical set of customer specifications on end-use properties for the polymer nanocomposites used in the packaging industry.

Table 7-1: Example customer specifications on end-use properties for polymer nanocomposites used in the packaging industry

| Property | Desired value with variance |
|---|---|
| Tensile strength, $w_1$ | 25.9 ± 1.41 (MPa) |
| Toughness, $w_2$ | 235 ± 20 (%) |
| Tear strength, $w_3$ | 50 ± 6.32 (lb/ft) |

For products from the same lot in a manufacturing process, it is reasonable to assume that the variability observed in the product properties $\boldsymbol{w}$ follows a multivariate normal distribution with mean vector $\boldsymbol{\mu}$ and a covariance matrix $\boldsymbol{\Sigma}$, so that when the manufacturing process is operating properly, for the product with specifications in Table 7-1, the 3-dimensional $\boldsymbol{w}$ vector is represented as:

$$\boldsymbol{w} = \boldsymbol{w}^* + \varepsilon;\ \boldsymbol{w}^* = \boldsymbol{\mu} = \begin{bmatrix}\mu_1\\ \mu_2\\ \mu_3\end{bmatrix}, \varepsilon = N(0, \boldsymbol{\Sigma}), \boldsymbol{\Sigma} = \begin{bmatrix}\sigma_1^2 & \rho_1\sigma_1\sigma_2 & \rho_2\sigma_1\sigma_3\\ \rho_1\sigma_1\sigma_2 & \sigma_2^2 & \rho_3\sigma_2\sigma_3\\ \rho_2\sigma_1\sigma_3 & \rho_3\sigma_2\sigma_3 & \sigma_3^2\end{bmatrix} \quad 7\text{-}1$$

where $\boldsymbol{w}^*$ is the desired set-point vector.

We assume that the manufacturing process is designed to meet the customer specifications at a pre-specified performance level $\pi^*$ = 95%. Then, for the given customer specification ranges $r_1$, $r_2$, and $r_3$, for the three $w$ variables, according to the customer specifications shown in Table 7-1, we designed a manufacturing process with appropriate variability so that the customer specifications are achieved at 95% performance level; then the standard deviations associated with each $w$ variable, $\sigma_1$, $\sigma_2$, and $\sigma_3$, cannot exceed the following specific values:

$$\sigma_1 = \frac{r_1}{\sqrt{C}}, \sigma_2 = \frac{r_2}{\sqrt{C}}, \sigma_3 = \frac{r_3}{\sqrt{C}} \quad 7\text{-}2$$

with the constant $C$ determined from the Chi-square distribution with 3 degrees of freedom value, which for the prescribed 95% performance level is obtained as:

$$C = \chi_3^2(1 - 0.95) = 7.81 \quad 7\text{-}3$$

The implication of Equation 7-2 is as follows: with 95% confidence, the observed values for each $w_i$, by definition of a 95% confidence interval, will lie in the range $w_i^* \pm \sqrt{C}\sigma_i$; this range will map directly onto the customer specified desired

range (and hence the manufactured process will be acceptable) only if the standard deviations associated with each variable do not exceed the values shown in Equation 7-2. For the example shown in Table 7-1, the customer specification ranges $r_1$, $r_2$, and $r_3$, are given as:

$$r_1 = 1.41, r_2 = 20, r_3 = 6.32 \qquad 7\text{-}4$$

So that to meet the customer specification at a performance level of 95%, the allowable standard deviations must not exceed the following values:

$$\sigma_1 = 0.5, \sigma_2 = 7.16, \sigma_3 = 2.28 \qquad 7\text{-}5$$

Finally, we note that end-use properties are correlated, (as implied in Equation 7-1); for the specific example, we consider a correlation structure represented by the following correlation coefficients:

$$\rho_1 = -0.42, \rho_2 = -0.67, \rho_3 = 0.63 \qquad 7\text{-}6$$

Consequently, the "acceptance region" in the example system's 3-dimensional product characteristics space in which at least 95% of the manufactured products will fall under normal conditions, is described by the following inequality:

$$(\boldsymbol{w} - \boldsymbol{\mu}_0)^T \boldsymbol{\Sigma}^{-1} (\boldsymbol{w} - \boldsymbol{\mu}_0) \leq 7.81 \text{ with } \boldsymbol{\Sigma} = \begin{bmatrix} \sigma_1^2 & \rho_1\sigma_1\sigma_2 & \rho_2\sigma_1\sigma_3 \\ \rho_1\sigma_1\sigma_2 & \sigma_2^2 & \rho_3\sigma_2\sigma_3 \\ \rho_2\sigma_1\sigma_3 & \rho_3\sigma_2\sigma_3 & \sigma_3^2 \end{bmatrix} \qquad 7\text{-}7$$

where from Table 7-1, $\boldsymbol{\mu}_0$ = [25.9 235 50]$^T$, and the standard deviations and the correlation coefficients are as in Equations 7-5 and 7-8. Thus, to produce acceptable products, the manufacturing process must be designed to maintain the product properties at the target values, with intrinsic variability no larger than the values

shown in Equation 7-5. In what follows, we assume that the end-use property control loop is capable of achieving this objective.

Problems arise when unmeasured disturbances perturb process operation away from conditions that customarily lead to the production of products whose properties lie in the acceptable region. This is particularly problematic because it is impossible to measure all possible product properties variables that contribute to the product's end-use performance. Under these conditions, the performance level (percentage of product that is acceptable by the customer) deteriorates and will not improve unless the disturbance is transient, or corrective action is taken to compensate for the effect of the disturbance. The role of the customer feedback controller may therefore be stated as follows: use customer feedback information (the most direct indicator of whether the produced product is able to meet the customer's end-use, not just measurements of product attributes) and employ it directly within the overall control scheme to take rational corrective action whenever the product performance level falls below a desired level as a result of the influence of a disturbance.

## 7.3 The Customer Feedback Control Scheme

The customer feedback loop as indicated in Figure 7-1 utilizes the (binary) customer feedback data to determine appropriate set-point targets for the product end-use properties. For the specific illustrative example described above, consider that of the three indicated properties, only $w_1$ and $w_2$ are measurable, while $w_3$ is not. Keep in mind, however, that all three end-use properties determine end-use performance. The basic premise of "Customer Feedback Control" is that one can take advantage of the correlations among these properties ($\rho \neq 0$), to compensate for the effects of disturbances on the unmeasured property by adjusting the values of the measured

properties commensurately. Thus, customer feedback control involves judiciously manipulating the measured properties to maximize the chances of meeting performance requirements.

The proposed customer feedback control scheme incorporating customer feedback information consists of the following three components: (i) modeling $z$ as a function of the measured product properties, $\boldsymbol{w}_m$, (ii) designing the controller $C_3$ based on the model, and (iii) developing a methodology to implement the controller.

### 7.3.1 Modeling Approach

In the proposed customer feedback control, the customer feedback information is integrated into a control loop that is outside the loop where the measured product attributes is effectively regulated; by utilizing the customer feedback data, the control decisions are then based on computing appropriate set-point targets for the measured product attributes to ensure the acceptable product performance. To facilitate making appropriate control decisions, it is necessary first to relate the customer feedback variable to the measured product attributes (in the illustrative example, $w_1$ and $w_2$).

As discussed in Garge *et al.* [128], the key impediment to designing customer feedback controller is associated with the following intrinsic characteristics of customer feedback information: (i) it is binary (the customer is either satisfied with the product, in which case $z = 1$, or not, in which case $z = 0$); and (ii) it is available infrequently (often on the order of days or weeks or however long it takes the customer to assess product performance in end-use). The binary characteristic of $z$ is illustrated in Figure 7-2, which shows representative data on measurements of $w_1$ and $w_2$ for 100 lots of product and the corresponding customer feedback. The challenge involved is twofold: (i) How does one model $z$ as a function of $\boldsymbol{w}$, particularly because

while $\boldsymbol{w}$ is continuous, the dependent variable $z$ is binary? (ii) How does one use such a model to implement a feedback controller?

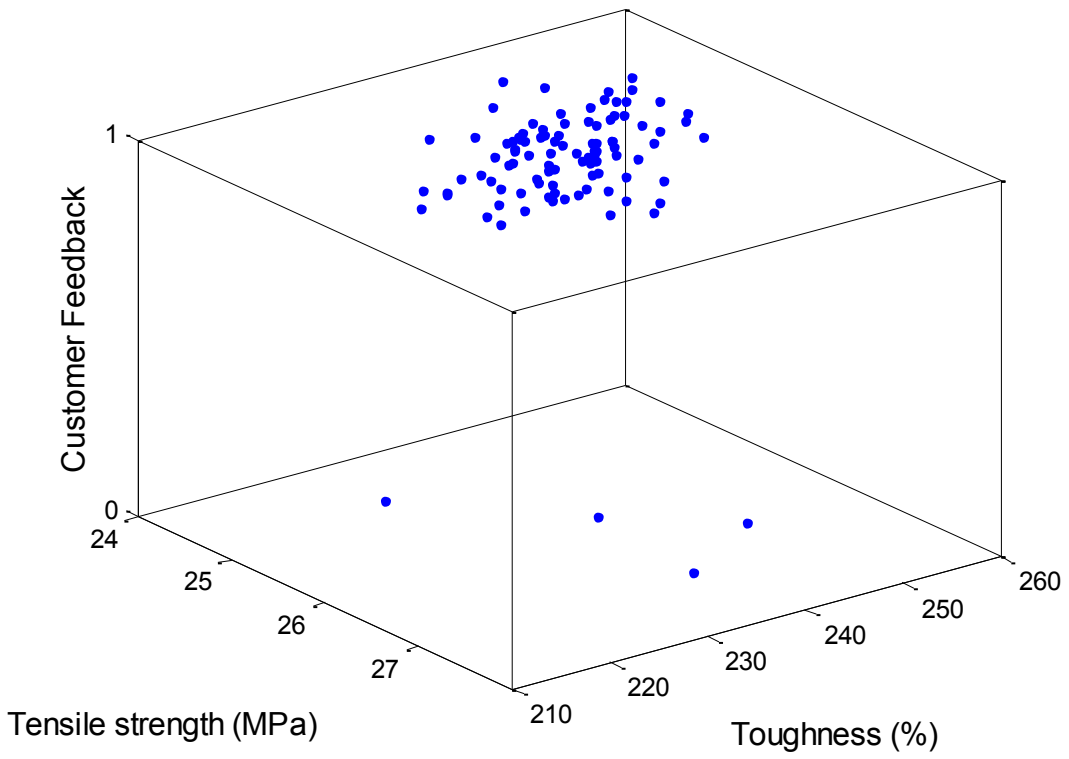


Figure 7-2: Customer feedback data on the measurements of tensile strength $w_1$ and toughness $w_2$ (the total number is 100)

Our modeling approach employs binary logistic regression (BLR) whereby $\boldsymbol{w}$, is used to compute $\pi(\boldsymbol{w})$, the probability of acceptance, defined as the probability that $z$ = 1, i.e., that the product with the indicated set of end-use characteristics meets the customer performance requirements [129]. The general mathematical form of the BLR model is given by:

$$ln\left[\frac{\pi(\boldsymbol{w}_m)}{1-\pi(\boldsymbol{w}_m)}\right] = \beta_0 + \sum_{i=1}^{m} \beta_i w_i \qquad 7\text{-}8$$

where $w_i$ is the $i^{th}$ measured product attribute. In the specific illustrative example, with two measured end-use properties, Equation 7-8 becomes:

$$ln\left[\frac{\pi(w_1, w_2)}{1-\pi(w_1, w_2)}\right] = \beta_0 + \beta_1 w_1 + \beta_2 w_2 \qquad 7\text{-}9$$

This equation can also be rearranged to:

$$\pi(w_1,\ w_2) = \frac{e^{\beta_0+\beta_1 w_1+\beta_2 w_2}}{1+e^{\beta_0+\beta_1 w_1+\beta_2 w_2}} \qquad 7\text{-}10$$

Generally, the maximum likelihood estimation method (MLE) is applied to estimate the BLR model parameters ($\beta_i$) from data. Given the BLR model, this method provides the values for the unknown BLR model parameters which maximize the probability of obtaining the observed set of customer feedback data. For the example customer feedback data in Figure 7-2, the estimated parameters by MLE method are:

$$\beta_1 = -2.35, \beta_2 = -0.17, \beta_3 = 0.04 \qquad 7\text{-}11$$

### 7.3.2 Controller Design

The objective of controller design is to derive an appropriate control law for determining the current set-points for the measured end-use properties, $\boldsymbol{w}_m^*(k)$, at sampling time instant $k$, required to meet the desired target performance level in the manufactured products,

$$\pi_k(\boldsymbol{w}_m^*) = \pi^* \qquad 7\text{-}12$$

given the current feedback information (equivalently, the current actual performance level) (see Figure 7-1). In the specific illustrative example, $\boldsymbol{w}_m^*(k) = [w_1^*(k)\ w_2^*(k)]^T$, $\pi^*$ is the target probability of acceptance (the desired performance level, for example, 95%).

In the vector form, the currently recommended set-point targets, $\boldsymbol{w}_m^*(k)$, can be computed by:

$$\boldsymbol{w}_m^*(k) = \boldsymbol{w}_m^*(k-1) + \Delta\boldsymbol{w}_m(k) \qquad 7\text{-}13$$

where $\boldsymbol{w}_m^*(k\text{-}1)$ is the set-point value in the previous sampling interval. Here, the controller determines $\Delta\boldsymbol{w}_m^*(k)$, the change in the set-point required to meet the desired performance level. In the specific illustrative example, $\Delta\boldsymbol{w}_m(k) = [\Delta w_1(k)\ \Delta w_2(k)]^T$.

Mathematically, the problem may be stated as follows: Given the BLR model in Equation 7-8, for $\pi(\boldsymbol{w}_m)$, determine $\boldsymbol{w}_m^*$ such that $\pi(\boldsymbol{w}_m^*) = \pi^*$, the pre-specified desired performance level. The solution to this problem requires optimization in the most general case, because $\pi(\boldsymbol{w}_m^*)$ is a scalar and $\boldsymbol{w}_m^*$ will almost always be a vector. For the specific illustrative example, with two measured variables, the required two-dimensional control vector $\Delta\boldsymbol{w}_m(k)$ is determined as a minimum norm adjustment

vector $||\Delta \boldsymbol{w}_m(k)||$ that maximizes $\pi(\boldsymbol{w}_m^*)$; in this case, it can be shown that the solution is (see Appendix G):

$$\Delta \boldsymbol{w}_m(k) = \begin{bmatrix} \frac{\hat{\pi}^* \beta_1 - \beta_0 \beta_1 - \beta_1 \beta_2 w_2(k-1) - \beta_1^2 w_1(k-1)}{\beta_1^2 + \beta_2^2} \\ \frac{\hat{\pi}^* \beta_2 - \beta_0 \beta_2 - \beta_1 \beta_2 w_1(k-1) - \beta_2^2 w_2(k-1)}{\beta_1^2 + \beta_2^2} \end{bmatrix} \quad \text{7-14}$$

### 7.3.3 Controller Implementation

Concerning the controller implementation, there are two aspects that need to be taken into consideration: the conceptual sequence of implementing the controller and the practical considerations during the controller implementation.

#### 7.3.3.1 Conceptual Sequence

Before implementing the controller, we first estimate the BLR model parameters by historical customer feedback data. The model parameters remain constant and are not updated throughout the controller implementation: The reason is that the BLR model with *measured* property variables cannot perfectly illustrate the relationship between $z$ and all possible product properties variables that contribute to the product's end-use performance (e.g., in the specific illustrative example, customer feedback is determined by $w_1$, $w_2$ and $w_3$ simultaneously). Thus, our control strategy is to achieve desired customer acceptability by adjusting the set-point targets of measured property variables without updating the BLR model parameters.

Then, the conceptual sequence of controller implementation, shown in Figure 7-3, is described as follows:

1. Total number of $N$ customer responses is collected during each time interval $k$, and the performance of products with previous end-use properties set-point targets $\boldsymbol{w}_m(k\text{-}1)$ is evaluated by the probability of product acceptance $\pi_{k\text{-}1}(\boldsymbol{w}_m)$. $\pi_{k\text{-}1}(\boldsymbol{w}_m)$ is calculated by counting the percentage of the total number of '$z = 1$' in $N$ customer feedback data, shown as follows:

$$\pi(\boldsymbol{w}) = \frac{\sum_{i=1}^{N} z}{N} \qquad 7\text{-}15$$

2. The probability of acceptance $\pi_{k\text{-}1}(\boldsymbol{w}_m)$ is then compared with the desired acceptance level $\pi^*$. If $\pi_{k\text{-}1}(\boldsymbol{w}_m)$ is smaller than $\pi^*$, the new set-point targets for $w_1$ and $w_2$ are calculated using control actions shown in Equation 7-14 with the estimated BLR model parameters. If $\pi_{k\text{-}1}(\boldsymbol{w}_m)$ is larger or equal to $\pi^*$, the controller does not update current set-point targets for the measured end-use properties.

3. Steps 1 and 2 are repeated at each time interval $k$.

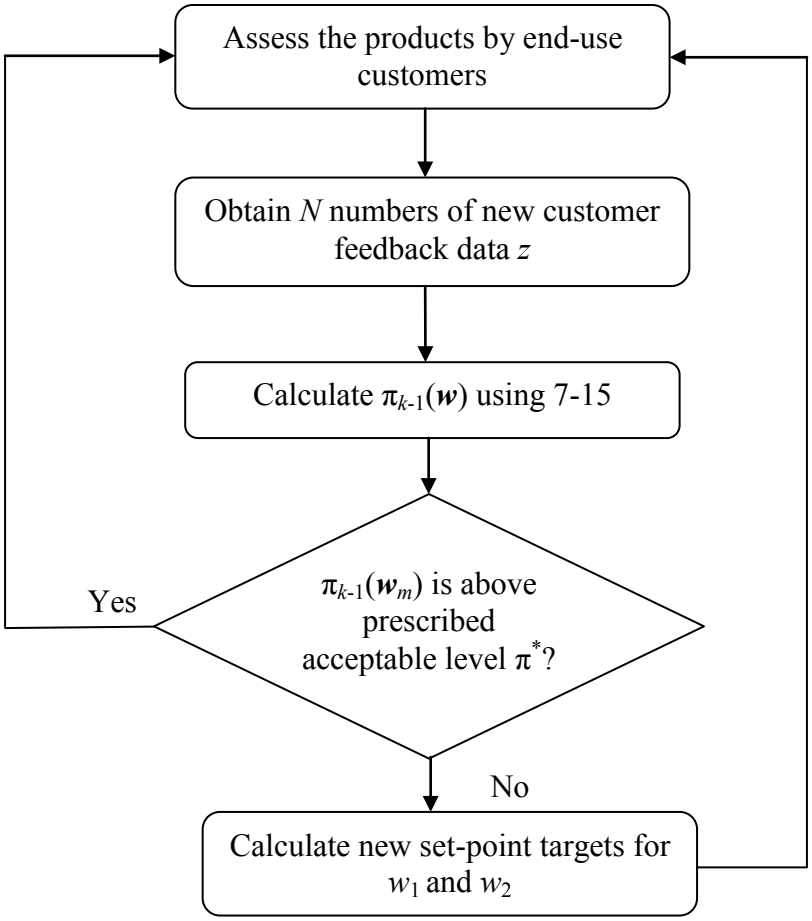


Figure 7-3: The conceptual sequence of controller implementation

#### 7.3.3.2 Practical Considerations

To implement the controller in practice, one has to consider the variability observed in the data. The variability in the data consists of two main aspects: (i) inherent variability in the end-use properties caused by measurement techniques, and (ii) uncertain variability of the customer feedback data $z$ when the customer processes the end-use product.

The procedure applied in practice is similar to the one described in previous section, but with the following two important modifications:

1. To account for the inherent variability in the end-use properties, instead of implementing the full change in set-point $\Delta \boldsymbol{w}_m(k)$, we introduced a weighting factors $0< \boldsymbol{\gamma} <1$ as follows:

$$\boldsymbol{w}_m^*(k) = \boldsymbol{w}_m^*(k-1) + \boldsymbol{\gamma} \circ \Delta \boldsymbol{w}_m(k) \qquad 7\text{-}16$$

   where $\boldsymbol{\gamma} = [\gamma_1\ \gamma_2\ \ldots\ \gamma_p]^T$ with $\gamma_i$ representing a 'weight' corresponding to $i^{th}$ product property. $\gamma_i$ is assumed to be inversely proportional to the standard error (SE) of the $N$ collected $i^{th}$ product property; thus, it can be computed by:

$$\gamma_i = \frac{K_i}{(SE)_i} \qquad 7\text{-}17$$

   where $K_i$ is a constant, which can also be considered as a tuning factor.

2. Considering the variability in customer feedback data, we used a damping factor to the targeting performance level by involving probability of acceptance of previous time interval $\pi_{k\text{-}1}(\boldsymbol{w}_m)$. As a result, Equation 7-12 was altered as follows:

$$\pi_k(\boldsymbol{w}_m^*) = \pi_{k-1}(\boldsymbol{w}_m) + \psi[\pi^* - \pi_{k-1}(\boldsymbol{w}_m)] \qquad 7\text{-}18$$

   Notice that the damping factor $\psi$ is employed to adjust the utilized portion of customer feedback information of the previous time interval. The parameter $\psi$, bounded between 0 and 1, can be tuned independently, with increasing aggressiveness as its value approaches

1. Consequently, $\hat{\pi}^*$, used to compute the control actions in 7-14, is modified as follows:

$$\hat{\pi}^*_{k-1} = ln\left[\frac{\pi_{k-1}(\boldsymbol{w}_m)+\psi[\pi^*-\pi_{k-1}(\boldsymbol{w}_m)]}{1-\pi_{k-1}(\boldsymbol{w}_m)+\psi[\pi^*-\pi_{k-1}(\boldsymbol{w}_m)]}\right] \quad 7\text{-}19$$

The main advantage of these modifications is that it accounts for the effects of variability existing both in end-use properties and in customer feedback data on the controller performance by parameters $\boldsymbol{\gamma}$ and $\psi$. In the case of our illustrative example, three tuning parameters such as $K_1$, $K_2$, and $\psi$ appear naturally in the modified procedure.

## 7.4 The Achievable Probability of Acceptable

Depending on the nature and magnitude of the disturbance responsible for reducing acceptable performance level, the customer feedback controller may or may not be able to eliminate the effect of the disturbance on the unmeasured properties completely. There is a maximal probability of acceptance that the customer feedback controller is able to achieve after the disturbance, which is defined as the achievable probability of acceptable. As part of the controller design process, it is necessary to develop a technique for determining achievable probability of acceptable in any attempt to recover from the occurrence of a performance-reducing disturbance.

### 7.4.1 The Determination of the Achievable Probability of Acceptable

To solve this problem, we first establish a mathematical relationship between the probability of acceptance $P$ and any given disturbance $\boldsymbol{d}$. Then, the achievable probability of acceptable is determined by maximizing $P$ based on the mathematical relationship.

Statistically, the probability of acceptance is the probability that the end-use properties of the manufactured products fall within the "acceptance region". According to the definition of acceptance region given by Equations 7-3 and 7-7, the probability of acceptance at any state can be expressed as:

$$P = P[(\boldsymbol{w} - \boldsymbol{\mu}_0)^T \boldsymbol{\Sigma}^{-1} (\boldsymbol{w} - \boldsymbol{\mu}_0) \leq C] \tag{7-20}$$

Similar to the special case for the 3-dimensional $\boldsymbol{w}$ vector (see Equation 7-1), the product properties $\boldsymbol{w}$ with ($m$+$n$) dimensions, where $m$ variables are measured while $n$ variables are not, also follows a multivariate normal distribution with mean vector $\boldsymbol{\mu}$ and a covariance matrix $\boldsymbol{\Sigma}$, represented as:

$$\boldsymbol{w} = \boldsymbol{w}^* + \varepsilon;\ \boldsymbol{w}^* = \boldsymbol{\mu} = \boldsymbol{\mu}_0 + \boldsymbol{\delta} = \begin{bmatrix} \mu_1 + \delta_1 \\ \mu_2 + \delta_2 \\ \cdots \\ \mu_m + \delta_m \\ \mu_{m+1} + d_1 \\ \cdots \\ \mu_{m+n} + d_n \end{bmatrix}, \varepsilon = N(0, \boldsymbol{\Sigma}) \tag{7-21}$$

where

$$\boldsymbol{\Sigma} = \begin{bmatrix} \sigma_1^2 & \rho_{12}\sigma_1\sigma_2 & \cdots & \rho_{1(m+n)}\sigma_1\sigma_{m+n} \\ \rho_{12}\sigma_1\sigma_2 & \sigma_2^2 & \cdots & \rho_{2(m+n)}\sigma_2\sigma_{m+n} \\ \vdots & \vdots & \ddots & \vdots \\ \rho_{1(m+n)}\sigma_1\sigma_n & \rho_{2(m+n)}\sigma_2\sigma_{(m+n)} & \cdots & \sigma_{m+n}^2 \end{bmatrix} \tag{7-22}$$

$$\boldsymbol{\mu}_0 = [\mu_1 \quad \cdots \quad \mu_m \quad \mu_{m+1} \quad \cdots \quad \mu_{m+n}]^T \tag{7-23}$$

$$\boldsymbol{\delta} = [\Delta\boldsymbol{w}; \boldsymbol{d}] = [\delta_1 \quad \cdots \quad \delta_m \quad d_1 \quad \cdots \quad d_n]^T \tag{7-24}$$

Notice that $\boldsymbol{\mu}$ is the mean vector of the ($m$+$n$) product properties at any given disturbance vector $\boldsymbol{d}$, which can be divided into two components: (i) $\boldsymbol{\mu}_0$, the vector of

initial mean, and (ii) $\boldsymbol{\delta}$, the vector of adjustments to the $m$ measured properties, $\Delta\boldsymbol{w} = [\delta_1\ \delta_2\ \dots\ \delta_m]^T$, and disturbances of the $n$ unmeasured properties, $\boldsymbol{d} = [d_1\ d_2\ \dots\ d_n]^T$.

If we define variable $D$ as

$$D = (\boldsymbol{w} - \boldsymbol{\mu}_0)^T \boldsymbol{\Sigma}^{-1} (\boldsymbol{w} - \boldsymbol{\mu}_0) \qquad 7\text{-}25$$

then the problem can be re-stated as follows: Given the pdf of $\boldsymbol{w}$ shown in Equation 7-21, determine the variable $D$'s pdf such that the probability of acceptance can be solved by calculating the cdf of the variable $D$ (see Equations 7-20 and 7-25).

To solve the problem, we first define a new variable $\boldsymbol{X}$ by de-trending $\boldsymbol{w}$ with its initial mean vector $\boldsymbol{\mu}_0$:

$$\boldsymbol{X} = \boldsymbol{w} - \boldsymbol{\mu}_0 \qquad 7\text{-}26$$

Then, the variable $D$ can be re-written as follows:

$$D = \boldsymbol{X}^T \boldsymbol{\Sigma}^{-1} \boldsymbol{X} = \left(\boldsymbol{\Sigma}^{-1/2} \boldsymbol{X}\right)^{\boldsymbol{T}} (\boldsymbol{\Sigma}^{-1/2} \boldsymbol{X}) \qquad 7\text{-}27$$

As a linear combination of the multivariate normally distributed variable $\boldsymbol{w}$, the variable $\boldsymbol{X}$ also follows a multivariate normal distribution with a new mean vector $\boldsymbol{\delta}$ and the same covariance matrix $\boldsymbol{\Sigma}$. Recall that if $\boldsymbol{X}$ follows a multivariate normal distribution with $N(\boldsymbol{X}^*, \boldsymbol{\Lambda})$ and $\boldsymbol{Y} = \mathbf{B}\boldsymbol{X} + \mathbf{b}$, then $\boldsymbol{Y}$ also follows a multivariate normal distribution with $N(\mathrm{E}(\boldsymbol{Y})\ , \mathrm{Cov}(\boldsymbol{Y}))$, where the mean and covariance can be calculated by $\mathrm{E}(\boldsymbol{Y}) = \mathbf{B}\boldsymbol{X}^* + \mathbf{b}$ and $\mathrm{Cov}(\boldsymbol{Y}) = \mathbf{B}\boldsymbol{\Lambda}\mathbf{B}^{\mathrm{T}}$ (see Chapter 5 in Gut [130]).

If the variable $\boldsymbol{Y}$ is defined as:

$$\boldsymbol{Y} = \boldsymbol{\Sigma}^{-1/2} \boldsymbol{X} \qquad 7\text{-}28$$

then $\boldsymbol{Y}$ is also multivariate normally distributed with the mean and covariance shown below:

$$E(\boldsymbol{Y}) = \boldsymbol{\Sigma}^{-1/2}\boldsymbol{\delta} \tag{7-29}$$

$$Cov(\boldsymbol{Y}) = \boldsymbol{\Sigma}^{-1/2}\boldsymbol{\Sigma}\boldsymbol{\Sigma}^{-1/2} = \boldsymbol{I} \tag{7-30}$$

Since the covariance matrix of the variable $\boldsymbol{Y}$ is an identity matrix, $Y_1$, $Y_2$ … $Y_{n+m}$ are ($n$+$m$) independent, normally distributed random variables with means shown in Equation 7-29 and unit standard deviations. Therefore, the variable $\boldsymbol{Y}$'s squared norm, $\boldsymbol{Y}^{\mathrm{T}}\boldsymbol{Y}$, is distributed according to the noncentral Chi-square distribution with ($m$+$n$) degrees of freedom and a noncentrality parameter $\lambda$ (see Chapter 1 in Muirhead [131]), where

$$\lambda = \left(\boldsymbol{\Sigma}^{-1/2}\boldsymbol{\delta}\right)^{T}\left(\boldsymbol{\Sigma}^{-1/2}\boldsymbol{\delta}\right) = \boldsymbol{\delta}^{T}\boldsymbol{\Sigma}^{-1}\boldsymbol{\delta} \tag{7-31}$$

From Equation 7-27 and the definition of $\boldsymbol{Y}$ (see Equation 7-28), it is observed that the variable $D$ is the squared norm of the variable $\boldsymbol{Y}$. Therefore, the pdf of the variable $D$ is a noncentral Chi-square distribution with ($m$+$n$) degree of freedom and noncentrality parameter $\lambda$ shown in Equation 7-31. As a result, the probability of acceptance depicted in Equation 7-20 is the cdf of the noncentral Chi-square distribution, shown below:

$$P = F(C; k; \lambda) = e^{-\lambda/2}\sum_{j=0}^{\infty}\left[\frac{\left(\frac{1}{2}\lambda\right)^{j}}{j!}Q(C; k+2j)\right] \tag{7-32}$$

where $k$ is the degree of freedom ($k = m+n$), $\lambda$ is the noncentrality parameter shown in by Equation 7-31, $C$ = 7.81 (see Equation 7-3), and $Q(C; k+2j)$ is the cdf of the central Chi-square distribution with ($k$+2$j$) degrees of freedom.

The mathematical expression of the probability of acceptance (Equation 7-32) shows that the probability of acceptance solely depends on $\lambda$, which is a measurement of how far the distribution of properties with a mean vector $\boldsymbol{\mu}$ for any given

disturbance vector $\boldsymbol{d}$ deviates from its initial distribution with the initial means $\boldsymbol{\mu}_0$. Specifically, higher value of $\lambda$ indicates larger deviation, which in turn leads to decreased probability of acceptance. Therefore, for any given disturbance vector, $\boldsymbol{d}$, the achievable probability of acceptance is the maximum of the cdf of a noncentral Chi-square distribution with $k$ degrees of freedom and the minimal noncentrality parameter $\lambda_{min}$ given by the expression:

$$P_{max} = F(C; k; \lambda_{min}) = e^{-\lambda_{min}/2} \sum_{j=0}^{\infty} \left[ \frac{\left(\frac{1}{2}\lambda_{min}\right)^j}{j!} Q(C; k + 2j) \right] \qquad 7\text{-}33$$

where $\lambda_{min}$ depends on the adjustments to the measured product properties, $\Delta\boldsymbol{w}_m$, and the magnitude of the disturbance, $\boldsymbol{d}$.

In the specific illustrative example with the 3-dimensional $\boldsymbol{w}$ vector but for which only the 2-dimensional subset, $[w_1, w_2]^T$, is measured, in the event of a step change disturbance of magnitude $d$ affecting $w_3$, the derivation of $\lambda_{min}$ is as follows.

$$\lambda_{min} = [\delta_1^* \quad \delta_2^* \quad d]\boldsymbol{\Sigma}^{-1} \begin{bmatrix} \delta_1^* \\ \delta_2^* \\ d \end{bmatrix} \qquad 7\text{-}34$$

where $\boldsymbol{\Sigma}$ is the covariance matrix defined in Equation 7-22, and $\delta_1^*$ and $\delta_2^*$ are the corresponding adjustments must be made for properties $w_1$ and $w_2$. Note that the values of $\delta_1^*$ and $\delta_2^*$ are only related to the covariance matrix parameters and $d$ (see Appendix H). The value of $P_{max}$ for given $\lambda_{min}$ can be readily calculated by software such as MATLAB®.

### 7.4.2 The Effect of the Disturbance Magnitude

The advantage of knowing the achievable probability of acceptance $P_{max}$ in advance is that this parameter provides insights into whether it is worthwhile to implement the customer feedback controller for performance recovery. For a given process with a constant variability (i.e., covariance matrix parameters does not change with time), ***d*** is the only variable that affects the achievable probability of acceptance (see Equations 7-33 and 7-34). Therefore, the study of the effect of the disturbance magnitude on $P_{max}$ will be insightful into making rational and judicious decisions of whether or not to implement the customer feedback controller for performance recovery. This study is illustrated by the afore-mentioned example involving $w_1$ and $w_2$ measurements.

For a step disturbance affecting unmeasured property $w_3$, the disturbance magnitude $d$ of interest ranges from 0 lb/ft to -10 lb/ft, listed in Table 7-2. For each $d$ under consideration, we calculated the following parameters using the covariance matrix parameters in Equations 7-5 and 7-6: the necessary adjustments $\delta_1^*$ and $\delta_2^*$ made for properties $w_1$ and $w_2$ respectively (Equations H-8 and H-9), the corresponding $\lambda_{min}$ (Equations 7-34), and $P_{max}$ (Equations 7-33). The results are shown in Table 7-2 and Figure 7-4.

From the results, we observe that under normal condition (i.e., $d = 0$), the achievable probability of acceptance can reach to the pre-specified performance level 95%; however, when the disturbance occurs (i.e., $d \neq 0$), $\lambda_{min}$ increases and the achievable probability of acceptance deteriorates with increased disturbance magnitude. This observation can be explained as follows: Based on the expressions of $\delta_1^*$ and $\delta_2^*$, $\lambda_{min}$ can be further simplified as:

$$\lambda_{min} = 0.193d^2 \qquad 7\text{-}35$$

where the constant 0.193 is computed using the covariance matrix parameters in Equations 7-5 and 7-6 (see Appendix H). Therefore, $\lambda_{min}$ is proportional to the square of the disturbance magnitude $d$. With increased disturbance magnitude, the distribution of properties with current mean vector deviates further from its initial distribution with initial means (i.e., larger $\lambda_{min}$), which as a result decreases the achievable probability of acceptance.

Table 7-2: The achievable acceptance of probability, $P_{max}$, the minimal noncentrality parameter, $\lambda_{min}$, and the corresponding adjustments of measurable properties, $\delta_1^*$ and $\delta_2^*$, at a given disturbance $d$

| $d$ (lb/ft) | $\delta_1^*$ (MPa) | $\delta_2^*$ (%) | $\lambda_{min}$ | $P_{max}$ (%) |
|---|---|---|---|---|
| 0 | 0.00 | 0.00 | 0.00 | 94.99 |
| -2 | 0.30 | -3.98 | 0.77 | 90.03 |
| -4 | 0.59 | -7.96 | 3.09 | 71.76 |
| -6 | 0.89 | -11.93 | 6.95 | 41.34 |
| -8 | 1.18 | -15.91 | 12.36 | 14.80 |
| -10 | 1.48 | -19.89 | 19.31 | 2.96 |

Also, note that the achievable probability of acceptance drops below 50% when the disturbance magnitude is larger than 5.5, and the achievable probability of acceptance becomes as low as 2.96% when the disturbance magnitude equals to 10 lb/ft. Usually, it is not economically efficient to implement the customer feedback controller when the predicted achievable probability of acceptance is below 50%; therefore, in the specific illustrative example, when the disturbance magnitude is larger than 5.5, a decision of not implementing the customer feedback controller $C_3$ should be made.

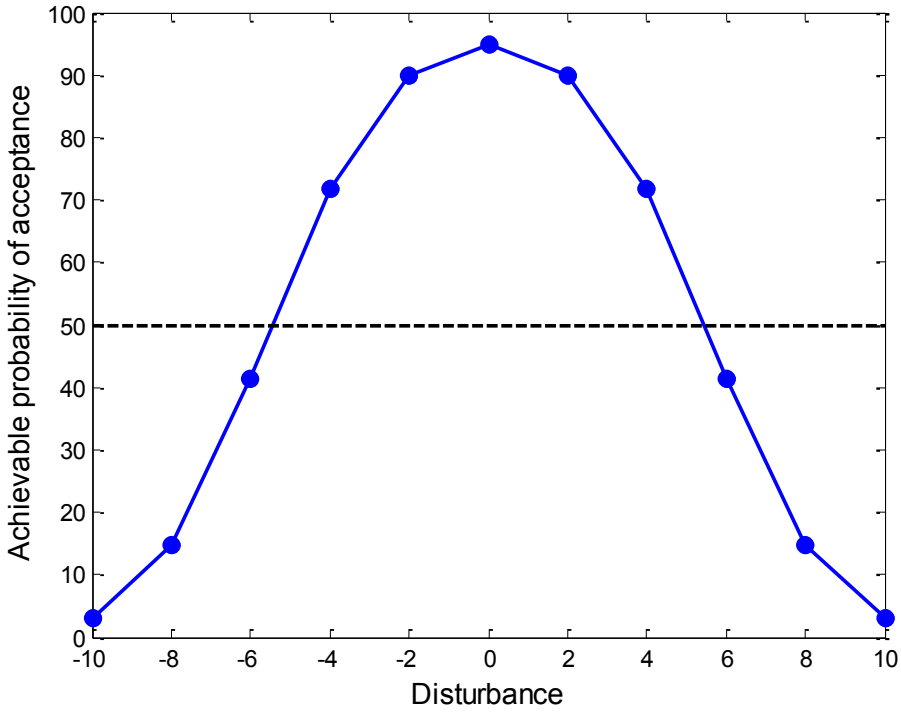


Figure 7-4: The achievable probability of acceptance with respect to disturbance magnitude. The green line is the achievable probability of acceptance, 50%

## 7.5 Simulation Case Study

A simulation case study is presented based on the illustrative example noted above involving two measurable properties (i.e., tensile strength and toughness). The customer feedback for this illustrative example is first simulated, and then the customer feedback controller is implemented to restore the dropped performance level due to the effect of the disturbance in the unmeasured end-use property (i.e., tear strength).

### 7.5.1 Customer Feedback Simulation

The simulation of customer feedback includes the acceptable region establishment, product attribute simulation, and customer assessment.

First, an "acceptance region" is defined in the example system's 3-dimensional attribute space generated from the customer specifications shown in Table 7-1. The expression of the acceptance region, in which at least 95% of the manufactured products will fall under normal conditions, is described in 7-7. Figure 7-5 shows the quality specification region (a cuboid) and the actual acceptable region (an ellipsoid). The ellipsoidal region indicates strong correlations among the end-use attributes, which implies that only certain combinations of the product attributes will lead to acceptable end-use performance.

As discussed before, the product attributes are assumed to follow a multivariate normal distribution with the mean values $\boldsymbol{\mu}$ and the covariance matrix $\boldsymbol{\Sigma}$, shown in Equation 7-1. Note that the mean values $\boldsymbol{\mu}$ are the same as the desired set-points $\boldsymbol{w}^*$ specified by the customer feedback controller, and the covariance matrix parameters are presented in Equations 7-5 and 7-6. Given the means and the covariance matrix, we generate the product attribute data randomly so that the attribute

variables are multivariate normally distributed. A representative example of product attribute data is shown in Figure 7-5. Each point in the figure represents a product with a specific combination of the product attributes.

The product attribute data are then delivered to the customer for performance assessment. As illustrated in Figure 7-5, if the point lies within the acceptance region (the ellipsoid), it means that the product shows satisfactory end-use performance, and the corresponding customer feedback information $z$ is assumed as 1 (blue dots); otherwise, z is assumed as 0 (red dots). It is assumed that the 100 products are sent to the customer for evaluation every day and the customer responses are collected at the end of each day.

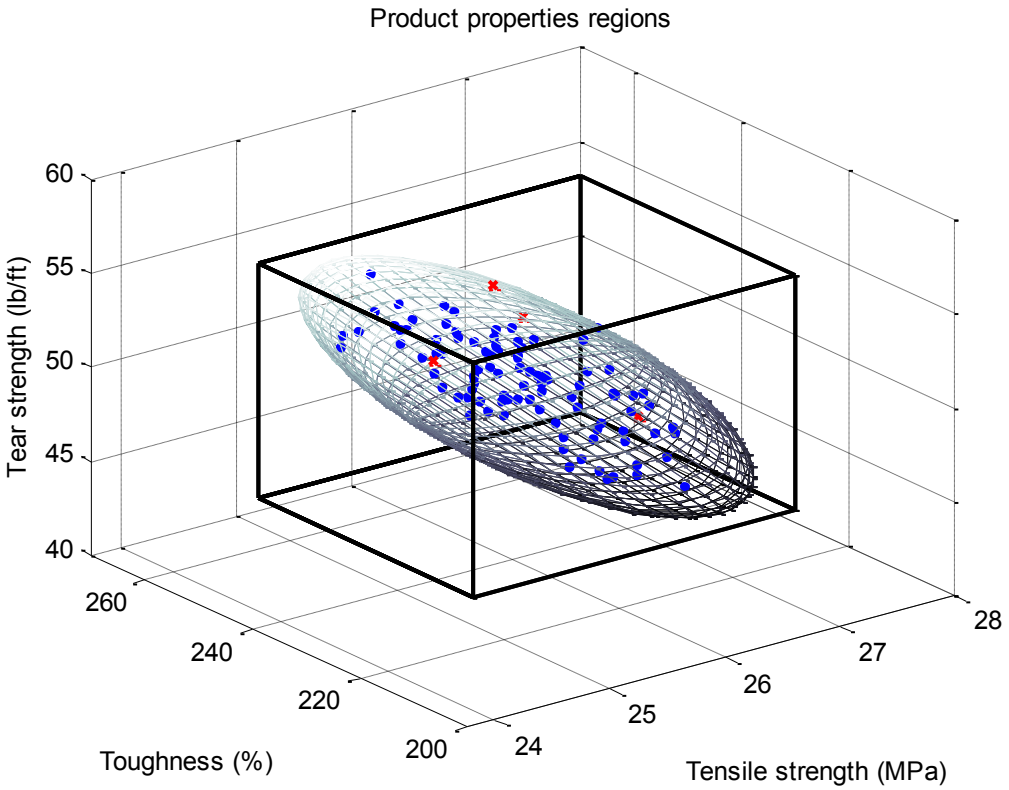


Figure 7-5: Customer feedback simulation: Each point represents measured properties of a particular product lot, in which blue points are the accepted products while red points are the unaccepted products; the region encompassed by the ellipsoid refers to the acceptable region; and the region inside the cuboid is regarded as the quality specifications provided by the customer

### 7.5.2 Controller Implementation via Simulation

Our goal of the customer feedback controller is to implement appropriate control actions (e.g., compute the set-point targets of the measurable properties $w_1$ and $w_2$) every day to enhance the performance level (the probability of acceptance). Towards achieving this goal, we first estimate the parameters for BLR model using the data of the first days (Figures 7-2 and 7-5), shown in Equation 7-11.

Then, the following procedure is implemented every day:

1. The set-points calculated from the previous day are employed to generate the product property data by Equation 7-1, and the corresponding customer feedback data are obtained from Equation 7-7.

2. Based on the customer feedback data $z$, the probability of customer acceptance for previous lot is evaluated by $\pi_{k-1}(\boldsymbol{w}_m)$ using equation 7-15. Also, the current desired probability of product acceptance is calculated via Equation 7-19.

3. The control action $\Delta\boldsymbol{w}_m(k)$ is computed from Equation 7-14 by taking the variability of customer feedback information into consideration. Here, the values of the tuning parameters are listed: $K_1 = 0.02$, $K_2 = 0.6$, and $\psi = 0.9$.

4. The property set-point targets of $w_1$ and $w_2$ for the next day are computed using Equation 7-13.

### 7.5.3 Simulation Results

The simulation results, shown in Figure 7-6, involve the probability of acceptance trajectory in 100 days. Initially, under normal condition, with $\boldsymbol{w}_0^*(k) = [25.9 \text{ MPa } 235 \text{ \% } 50 \text{ lb/ft}]^T$, the probability of customer acceptance is about 95%. Then, a disturbance is introduced on the 20$^{th}$ day, which shifts the mean of the unmeasured property, tear strength, from 50 lb/ft to 46 lb/ft, instantaneously reducing the product performance level, (the probability of customer acceptance) from 95% to

23%. From the magnitude of the disturbance, we are able to compute the maximum achievable performance level to be achievable 71.76%.

The customer feedback controller, which implements corrective action daily on the basis of feedback information from the customer, resulted in the trajectory shown in Figure 7-6 whereby the performance level is improved to something in the neighborhood of 70%, consistent with the computed maximum achievable value (see Table 7-2).

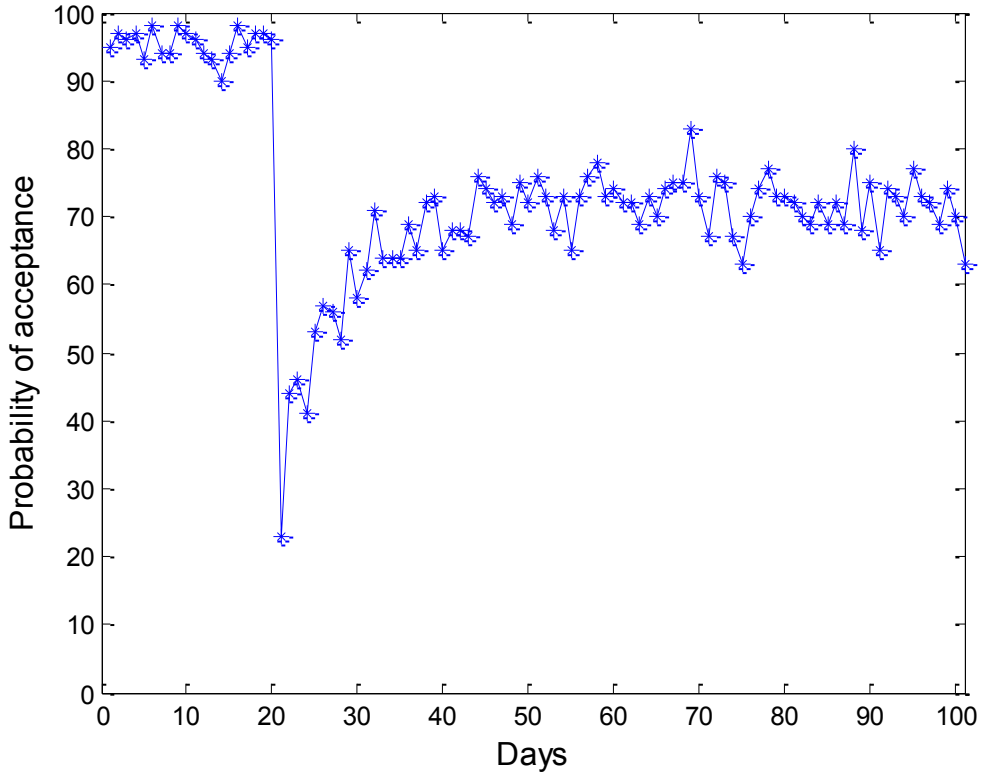


Figure 7-6: Performance of the customer feedback controller in simulation on an illustrative example process: In response to a disturbance occurring on the 20$^{th}$ day. An initial state: 95% acceptability, after the disturbance state: 23% acceptability, and final state: 70% acceptability.

The actual trajectories of the measured end-use properties in 100 days are shown in Figure 7-7. It can be seen that in the process of compensating for the effect of the disturbance on the unmeasured tear strength, improving the performance level required an increase in the set-point for tensile strength in conjunction with a decrease in the set-point for toughness. The final mean values for the end-use properties are $\boldsymbol{w}_m^*(k)$ = [26.49 MPa 226.85 %]$^T$. The total adjustments the customer feedback controller had to make are $\delta_1 = 0.59$ for tensile strength and $\delta_2 = -8.15$ for toughness, which is also consistent with the computed maximum achievable value (see Table 7-2).

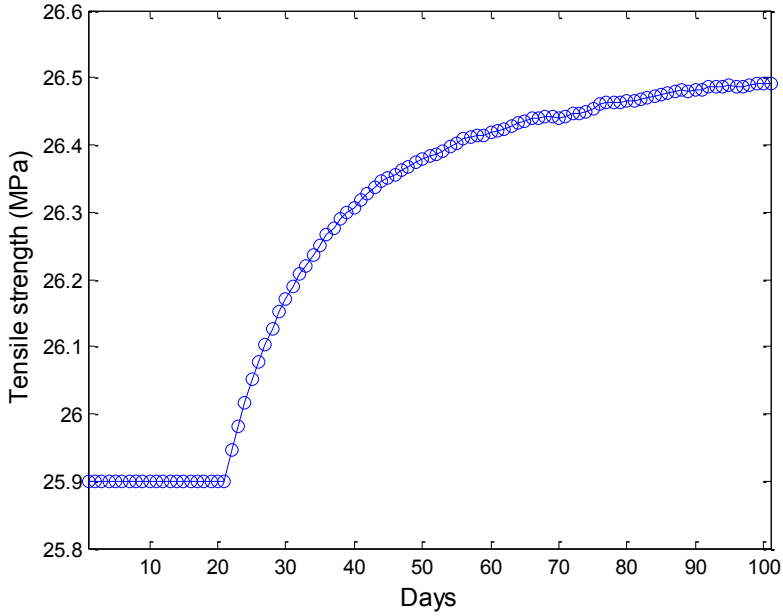


(a)

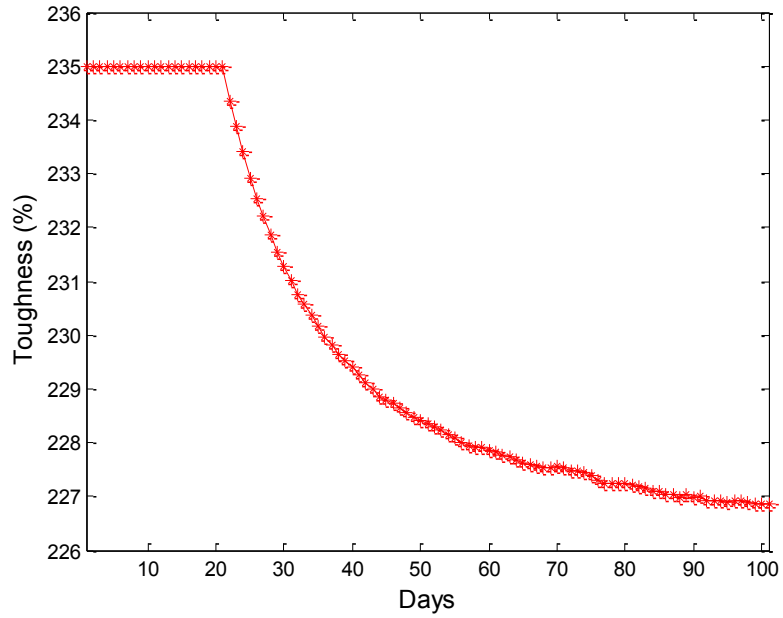


(b)

Figure 7-7: The trajectories for (a). tensile strength; (b). toughness in 100 days; the disturbance occurs at the 20th day

## 7.6 Conclusions

In this chapter, a customer feedback controller explicitly including customer feedback information has been designed to ensure acceptable product end-use performance by determining appropriate set-point targets of the measured properties for the quality controller. The controller design was based on a binary logistic regression (BLR) model which relates the continuous product properties with binary customer feedback data. Then, we derived a control strategy that utilizes this model to compute the appropriate targets for the measured properties required to maximize the probability of acceptance up to a pre-specified value.

To account for the variability from the measured product properties and from customer feedback data, we defined three tuning parameters $K_1$, $K_2$, and $\psi$ when the customer feedback controller is implemented in practice. In addition, the achievable probability of acceptance, which is the best probability of acceptance that the feedback controller can achieve after the disturbance, was proved to be the cumulative distribution function of a noncentral Chi-square distribution. Accordingly, the achievable probability of acceptance and the correspondingly theoretical adjustments for the measured properties made by the customer feedback controller were computed for a wide range of disturbance.

Finally, we implemented the designed controller to an industrial polymer nanocomposites manufacturing process by simulation. The simulation results illustrate how, in response to a disturbance that shifted the unmeasured property where the performance level was dramatically deteriorated, the customer feedback controller successfully increases the probability of acceptance to the achievable probability of acceptance. Also, the adjustments for the measured properties made by the controller in the simulation matches those computed theoretically based on the analytical

solution of the achievable probability of acceptance. Future studies should focus on determining the criteria of tuning the customer feedback parameters $K_1$, $K_2$, and $\psi$ (see Chapter 8).

# Chapter 8

# SUMMARY AND FUTURE WORK

## 8.1 Summary

The work presented in this dissertation provides guidelines for developing a paradigm to manufacture designed products for tailored applications in which the target end-use characteristics are consistently achieved. This paradigm includes designing products for specific end-use applications and determining manufacturing processes (i.e., product design), following which the processes must be operated using appropriate control strategies to produce products with acceptable end-use performance (i.e., control system design).

While product design has received deserved attention, the equally important next step – a control scheme designed for ensuring that what the manufacturing process produces will perform as designed – has received little or even no attention. In addition, since it is the customer that evaluates the product performance in end-use, the control strategy required for achieving the objectives of product design must extend well beyond the traditional control scheme of merely controlling process output variables and even beyond the product end-use characteristics control; it must *explicitly* incorporate customer feedback on the product performance, in order to ascertain consistent attainment of desired product end-use performance characteristics. However, this feedback is completely missing from the control schemes typically employed on manufacturing processes.

To address these challenging issues, the work in this thesis aims to develop and validate a framework for integrating product design with appropriate control strategies required for achieving acceptable product performance consistently. Because of their current and future importance, polymer nanocomposites are used as the focusing problem. Therefore, the framework is illustrated by manufacturing polymer nanocomposites using extrusion processes for packaging of cereals and cookies/crackers. The key results and conclusions of this work are summarized as follows.

### 8.1.1 Systematic Product Design

As an inseparable component of the framework, a systematic product design was employed first to determine the manufacturing material, consequent manufacturing process, and required operating conditions in manufacturing polymer nanocomposites. According to the packaging application, polymer nanocomposites based on Na ionomer and an organically modified MMT (Cloisite® 20A) were determined as the manufacturing material. To facilitate the clay dispersion in the polymer matrix, a two-step melt mixing masterbatch method was employed to manufacture the material, using the TSE for producing clay-rich masterbatches and the DSM micro compounder for diluting the masterbatches to desired clay concentration. By using a series of carefully designed experiments, we determined the optimal combination of processing conditions in DSM and TSE and clay concentration required to obtain product with desired end-use properties (e.g., stiffness and toughness). This work has provided, for the first time, a systematic procedure for determining the optimal combination of processing conditions and clay concentration

required to achieve desired end-use properties, using a two-step melt mixing masterbatch method in manufacturing polymer nanocomposites.

In the case of manufacturing polymer nanocomposites, product design also involves the identification of factors that affect the clay dispersion significantly. Both literature and experimental studies reveal that the organoclay type has a significant effect on the clay dispersion, which affects the end-use properties in turn. In our polymer nanocomposites system, it was found that the Cloisite® 20A (20A) improves the clay dispersion, while the Cloisite® 93A (93A) deteriorates the extent of clay exfoliation. The 20A concentration in the 20A and 93A mixture was identified as the factor dispersion sensitive factor and was used as the manipulated variable for the control of the end-use properties.

### 8.1.2 Quantification of Clay Dispersion

Prior to control system design, inference models are needed for predicting end-use properties and realizing on-line property control. However, in the case of polymer nanocomposites, developing these models requires a quantitative description of clay dispersion such that mathematical relationships (i.e., inference models) are able to be established among clay dispersion, end-use properties, and processing variables. Unfortunately, currently available techniques (e.g., X-ray diffraction and TEM) can only provide qualitative information about the organoclay dispersion.

We proposed a novel methodology for quantifying clay dispersion proposed, based on describing particle length distribution data from TEM micrographs with a gamma probability distribution model, $\gamma(\alpha, \beta)$, where the parameters $\alpha$, the mean number of platelets per particle, and $\beta$, the mean "effective platelet length", are shown to be related to the degree of dispersion. Next, using several published data sets on a

wide variety of polymer nanocomposites, an explicit quantitative relationship between these parameters and the extent of dispersion were established successfully. Specifically, the dispersion characteristics were captured effectively by a characteristic dispersion parameter, $\delta$, defined along dispersion contours represented by the empirical relation $\delta = \alpha + 0.05\beta$, where $\delta < 5$ for exfoliated composites, $5 < \delta < 6.5$ for less exfoliated composites with stacks containing several layers, and $\delta > 6.5$ for intercalated composites. In addition, the proposed method was validated successfully via independent *experiments* involving two nanocomposites with different morphologies.

The unique advantage of this methodology is that the proposed dispersion parameter arises as a combination of parameters derived from mechanisms of clay particle formation, and a probability model that has been rigorously validated as appropriate for representing particle length distributions. All the parameters are therefore related directly to physical characteristics of clay particles, and hence provide theoretical insight into the structures of these particles in the polymer matrix. Furthermore, we believe that this method facilitates quantitative comparison of clay dispersion for polymer nanocomposites prepared with different polymers, reinforced with different organoclays, or prepared under different processing conditions. Therefore, this methodology has several potential applications, which will be discussed in section 8.2.1.

### 8.1.3 Control System Design and Implementation

The proposed control scheme has a multiple-loop structure with a controller at each cascading level: (i) the innermost loop with controller $C_1$ for controlling process outputs, $y$, by adjusting manipulated variables, $u$, (ii) the outer loop with controller $C_2$ for regulating the product end-use properties, $w$, by manipulating the process outputs, $y$, and (iii) the outermost loop with controller $C_3$ for improving customer satisfaction by using customer feedback data, $z$, to compute appropriate set-points for end-use properties, $w$. The controller $C_1$ and $C_2$ were designed as multiple-input multiple-output model predictive controllers since such controllers are more effective in the case of multivariable and constrained processes, while controller $C_3$ was designed as an unconventional customer feedback controller utilizing customer feedback data to take rational corrective action if the product does not perform in end-use precisely as designed.

The controller structure of $C_1$ was configured as a $3 \times 3$ system, where the process input and output variables were selected judiciously and rationally. The model, $M_{uy}$, was identified by an empirical approach based entirely on input-output data. Preliminary experiments, involving step change in each single input variable and staircase change in one input variable, revealed that the process is approximately linear around the operating point determined by product design. The input excitations in the final identification test were carefully designed as generalized binary noise signals, from which three multiple-inputs single-output (MISO) linear models were successfully identified. The model structures for the outputs revealed how the process outputs relate to the process inputs and the disturbances, which is in agreement with the process physics. Based on the set of MISO models, the controller $C_1$ was designed,

followed by controller implementation in simulation first for appropriately tuning the controller parameters. Then, the performance of the controller was tested on the experimental process based on a LabVIEW-Matlab software interface. Offsets were observed, which may be due to the reason that there is only one truly independent manipulated variable. However, these offsets were not expected to deteriorate the performance of the overall control scheme, because the outer loop controller $C_2$ is able to compensate for the offsets.

The controller $C_2$ is based on the model, $M_{yw}$, which relates the end-use properties $w$ with the process output variables $y$ by a steady-state gain matrix. The simulation results of implementing the controllers $C_1$ and $C_2$ showed that the control scheme cannot achieve any arbitrary set-points of end-use properties; the achievable product specifications must be within the permission of process physics.

As the most direct indicator of product end-use performance, the customer feedback on product performance needs to be incorporated into the overall control scheme. Since it is impossible to measure and control all possible product properties variables, $w$, that contribute to the product's end-use performance, when disturbances occur, the performance level (percentage of product that is acceptable by the customer) deteriorates and will not improve unless the disturbance is transient, or corrective action is taken to compensate for the effect of the disturbance. Therefore, the customer feedback controller use customer feedback information, $z$, (the most direct indicator of whether the produced product is able to meet the customer's end- use, not just measurements of product attributes $\boldsymbol{w}_m$) and employ it directly within the overall control scheme to take rational corrective action whenever the product performance level falls below a desired level as a result of the influence of a disturbance.

The main challenge of designing such a controller is the binary characteristics of the customer feedback data; therefore, a novel modeling technique is required to relate the binary customer feedback data with the continuous product end-use properties. To do this, we employed binary logistic regression (BLR) method where the binary data were first converted to real-valued probability of receiving acceptable performance (i.e., probability of acceptance), followed by the development of a mathematical relationship between this new variable and end-use property variables. Based on the BLR model, the customer feedback controller $C_3$ was developed to maximize the probability of acceptance by adjusting set-point targets for $\boldsymbol{w}_m$, which were determined by a closed form "minimum norm" solution to maximize the probability of acceptance. The controller was implemented in simulation by introducing tuning parameters such as $K_1$, $K_2$, and $\psi$. The controller showed satisfactory performance in the simulation, where it was able to improve the probability of acceptance after the disturbance occurred.

In addition, it is necessary to develop a technique for determining achievable probability of acceptable in any attempt to recover from the occurrence of a performance-reducing disturbance. The probability of acceptance was proven to be the cumulative distribution function of a noncentral Chi-square distribution, where it only depends on the noncentrality parameter $\lambda$. Since the probability of acceptance improves as $\lambda$ decreases, the achievable probability of acceptable, $P_{max}$, can be obtained by the minimal noncentrality parameter $\lambda_{min}$, where $\lambda_{min}$ depends on the adjustments to the product properties, $\Delta\boldsymbol{w}_m$, and the magnitude of the disturbance, $\boldsymbol{d}$. Based on these insights, we studied the effects of disturbance magnitude on $P_{max}$, which was illustrated by the example involving three end-use properties with two of

them measured. The results of this theoretical study were consistent with the simulation results, where $P_{max}$ decreases dramatically as the magnitude of disturbance increases. The advantage of knowing the achievable probability of acceptance in advance for a given disturbance is that this parameter provides insights into whether it is worthwhile to implement the customer feedback controller for performance recovery.

## 8.2 Future Work

Several opportunities of future research can be extended from the work in this dissertation, and they are summarized as follows.

### 8.2.1 Applications of the Quantification Method of Clay Dispersion

Quantitative measurements of the microstructures of polymer nanocomposites provide a better understanding of correlations between material processing-microstructure-property characteristics [132]. The dispersion quantification method proposed in this thesis can be used to the following applications: (i) systematic studies of the effects of important factors on clay dispersion, where quantitative correlations between factors (e.g., surface structure of the clay, material processing, clay loading, ect.) and microstructure are required, and (ii) inference model development, where it is necessary to correlate the material microstructure with their processing and properties.

#### 8.2.1.1 Systematic Studies of the Effects of Important Factors on Clay Dispersion

Several factors, involving chemistry of the polymer and organoclays, processing conditions, and nanofiller amount, have significant effects on the clay dispersion as well as the product properties. Literature review has demonstrated that

interfacial interactions between polymers and organoclays are dominant in achieving high dispersion, and the processing conditions also affect the clay dispersion (see section 2.2 and Chapter 3). In addition, the nanofiller amount in the polymer matrix affects the clay dispersion as well as the product properties [35]. Usually, product properties are improved with increased nanofiller loadings [133, 134]; however, such property improvements can only be achieved below an optimum nanofiller amount [135]. Therefore, an optimal combination of polymer and organoclay chemistry, processing conditions, and nanofiller loading is required to facilitate clay dispersion. However, due to the lack of an effective method to quantify the clay dispersion, such a study is not presented in current literature. With the assistance of the quantification method proposed in this thesis, the comprehensive studies of the effects of interfacial interactions, material processing, and nanofiller loading become possible, which will provide a more fundamental understanding of the reinforcement mechanisms.

#### 8.2.1.2 Inference Model Development

As discussed in Chapter 6, an effective on-line control of product properties requires these properties to be obtained at a much faster rate. To predict the infrequently measured product properties at a frequent enough rate, it is imperative to develop inference models for these properties that can accurately estimate these variables. Since the clay dispersion is the most relevant and direct indicator of product end-use properties, it is desirable to relating this variable to the property characteristics for reliable estimation.

The inference models for end-use properties of polymer nancomposites, $M_{y\delta w}$, are expected to consist of the following models: (i) $M_{y\delta}$ – relating the process output variables, $y$, to the clay dispersion indicator, $\delta$, and (ii) $M_{\delta w}$ – relating the clay

dispersion indicator, $\delta$, to the end-use properties, $w$. The $M_{y\delta}$ model may be developed by response surface design of experiment, from which mathematical correlations between $y$ and $\delta$ can be obtained. The $M_{\delta w}$ may be based on the composites theories (e.g., Halpin-Tsai and Mori-Tanaka); however, the details of this model are not clear right now and need further research before the implementation of this model (see Appendix C for some initial efforts for establishing the model).

Next, the inference model will be used to predict the end-use properties at a fast rate for controlling the properties in real-time.

### 8.2.2 Customer Feedback Controller: Stability Analysis and Tuning Strategies

In this thesis, we utilized the customer feedback information, for the first time, to design a customer feedback controller. The controller was implemented in simulation successfully by choosing appropriate tuning parameters such as parameters $K_1$, $K_2$, and $\psi$. However, systematic strategies for choosing the controller parameters are remaining issues.

These challenging issues can be addressed by theoretical robust stability analysis (see examples in Mukati and Ogunnaike [136]). The stability analysis may provide insights into how the choices of various $K_1$, $K_2$, and $\psi$ parameter values jointly and individually affect closed-loop stability, which will be used to develop tuning rules for the customer feedback controller.

### 8.2.3 Validation of the Overall Control Scheme

The overall control scheme, consisting of three controllers at three levels, was proposed in this dissertation for manufacturing polymer nanocomposites processes. The controller $C_1$ of the innermost loop has been experimental implemented on a pilot-

scale extrusion process, while controllers $C_2$ and $C_3$ were tested only in simulation environment. To validate the overall control scheme on the experimental process, it is necessary to go through the following steps: (i) involve inference models, $M_{y\delta w}$, to predict end-use properties at a fast enough rate for on-line control of the properties, (ii) test and validate controller $C_2$ on real extrusion process, and (iii) implement and validate the overall control scheme incorporating customer feedback controller $C_3$ on the real process, where the customer feedback information will be obtained after testing the materials in the lab environment. Then, we will generalize the principles and concepts to be applicable to other products.

## REFERENCES


1. Giordano, G.; Inman, H., Thinking small pays big. *Plast. Eng* **2010,** 66, (1), 6-10.
2. Bhattacharya, S. N.; Kamal, M. R.; Gupta, R. K., *Polymeric nanocomposites: theory and practice*. Hanser Gardner Publications: 2008.
3. Usuki, A.; Kojima, Y.; Kawasumi, M.; Okada, A.; Fukushima, Y.; Kurauchi, T.; Kamigaito, O., Synthesis of nylon 6-clay hybrid. *Journal of Materials Research(USA)* **1993,** 8, (5), 1179-1184.
4. Okada, A.; Usuki, A., Twenty years of polymer-clay nanocomposites. *Die Angewandte Makromolekulare Chemie* **2006,** 291, (12), 1449-1476.
5. Cho, J. W.; Paul, D. R., Nylon 6 nanocomposites by melt compounding. *Polymer* **2001,** 42, (3), 1083-1094.
6. Yano, K.; Usuki, A.; Okada, A.; Kurauchi, T.; Kamigaito, O., Synthesis and properties of polyimide clay hybrid. *Journal of Polymer Science Part A: Polymer Chemistry* **1993,** 31, (10), 2493-2498.
7. Messersmith, P. B.; Giannelis, E. P., Synthesis and barrier properties of poly (ε-aprolactone)-layered silicate nanocomposites. *Journal of Polymer Science Part A: Polymer Chemistry* **1995,** 33, (7), 1047-1057.
8. Schmidt, D.; Shah, D.; Giannelis, E. P., New advances in polymer/layered silicate nanocomposites. *Current Opinion in Solid State and Materials Science* **2002,** 6, (3), 205-212.
9. Gilman, J. W.; Jackson, C. L.; Morgan, A. B.; Harris Jr, R.; Manias, E.; Giannelis, E. P.; Wuthenow, M.; Hilton, D.; Phillips, S. H., Flammability properties of polymer layered-silicate nanocomposites: polypropylene and polystyrene nanocomposites. *Chem. Mater* **2000,** 12, (7), 1866-1873.
10. Azeredo, H., Nanocomposites for food packaging applications. *Food Research International* **2009,** 42, (9), 1240-1253.
11. Garces, J. M.; Moll, D. J.; Bicerano, J.; Fibiger, R.; McLeod, D. G., Polymeric nanocomposites for automotive applications. *Advanced Materials* **2000,** 12, (23).
12. Gacitua, W.; Ballerini, A.; Zhang, J., Polymer nanocomposites: synthetic and natural fillers a review. *Maderas, Cienc. tecnol*, 159-178.
13. Terman, G. W., A little goes a long way. In LWW: 2005.
14. Pavlidou, S.; Papaspyrides, C. D., A review on polymer–layered silicate nanocomposites. *Progress in Polymer Science* **2008,** 33, (12), 1119-1198.
15. Fornes, T. D.; Yoon, P. J.; Hunter, D. L.; Keskkula, H.; Paul, D. R., Effect of organoclay structure on nylon 6 nanocomposite morphology and properties. *Polymer* **2002,** 43, (22), 5915-5933.

16. Ratinac, K. R.; Gilbert, R. G.; Ye, L.; Jones, A. S.; Ringer, S. P., The effects of processing and organoclay properties on the structure of poly (methyl methacrylate)-clay nanocomposites. *Polymer* **2006,** 47, (18), 6337-6361.
17. Scarfato, P.; Scatteia, L.; Costa, G.; Acierno, D. In *Effect of the organoclay structure on morphology and rheological response of PBT nanocomposites*, 2005; WILEY-VCH Verlag Weinheim: 2005.
18. Yoon, P. J.; Hunter, D. L.; Paul, D. R., Polycarbonate nanocomposites. Part 1. Effect of organoclay structure on morphology and properties. *Polymer* **2003,** 44, (18), 5323-5339.
19. Shah, R. K.; Hunter, D. L.; Paul, D. R., Nanocomposites from poly (ethylene-co-methacrylic acid) ionomers: effect of surfactant structure on morphology and properties. *Polymer* **2005,** 46, (8), 2646-2662.
20. Aranda, P.; Ruiz-Hitzky, E., Poly (ethylene oxide)-silicate intercalation materials. *Chemistry of Materials* **1992,** 4, (6), 1395-1403.
21. Wu, J.; Lerner, M. M., Structural, thermal, and electrical characterization of layered nanocomposites derived from sodium-montmorillonite and polyethers. *Chemistry of Materials* **1993,** 5, (6), 835-838.
22. Ogata, N.; Jimenez, G.; Kawai, H.; Ogihara, T., Structure and thermal/mechanical properties of poly (I-lactide)-clay blend. *Journal of Polymer Science Part B: Polymer Physics* **1997,** 35, (2), 389-396.
23. Mehrotra, V.; Giannelis, E. P., Conducting molecular multilayers: intercalation of conjugated polymers in layered media. *Mater Res Soc Synp Proc* **1990,** 171, 39-44.
24. Fornes, T. D.; Paul, D. R., Formation and properties of nylon 6 nanocomposites. *Polímeros* **2003,** 13, (4), 212-217.
25. Fornes, T. D.; Yoon, P. J.; Keskkula, H.; Paul, D. R., Nylon 6 nanocomposites: the effect of matrix molecular weight. *Polymer* **2001,** 42, (25), 9929-9940.
26. Chavarria, F.; Shah, R. K.; Hunter, D. L.; Paul, D. R., Effect of melt processing conditions on the morphology and properties of nylon 6 nanocomposites. *Polymer Engineering and Science* **2007,** 47, (11), 1847-1864.
27. Vaia, R. A.; Giannelis, E. P., Polymer melt intercalation in organically-modified layered silicates: model predictions and experiment. *Macromolecules* **1997,** 30, (25), 8000-8009.
28. Huang, J.-C.; Zhu, Z.-k.; Yin, J.; Qian, X.-f.; Sun, Y.-Y., Poly (etherimide)/montmorillonite nanocomposites prepared by melt intercalation: morphology, solvent resistance properties and thermal properties. *Polymer* **2001,** 42, (3), 873-877.
29. Ton-That, M.-T.; Perrin-Sarazin, F.; Cole, K. C.; Bureau, M. N.; Denault, J., Polyolefin nanocomposites: formulation and development. *Polymer Engineering & Science* **2004,** 44, (7), 1212-1219.
30. Tillekeratne, M.; Jollands, M.; Cser, F.; Bhattacharya, S. N., Role of mixing parameters in the preparation of poly (ethylene vinyl acetate) nanocomposites by melt blending. *Journal of Applied Polymer Science* **2006,** 100, (4), 2652-2658.

31. Dennis, H. R.; Hunter, D. L.; Chang, D.; Kim, S.; White, J. L.; Cho, J. W.; Paul, D. R., Effect of melt processing conditions on the extent of exfoliation in organoclay-based nanocomposites. *Polymer* **2001,** 42, (23), 9513-9522.
32. Besco, S.; Modesti, M.; Lorenzetti, A., Influence of Processing Parameters on the Structure of Melt Blended Polyethylene/Organoclay Nanocomposites Produced by a Masterbatch Route. *Polymer Engineering and Science* **2013,** 53, (4), 689-698.
33. Fasulo, P. D.; Rodgers, W. R.; Ottaviani, R. A.; Hunter, D. L., Extrusion processing of TPO nanocomposites. *Polymer Engineering & Science* **2004,** 44, (6), 1036-1045.
34. Lertwimolnun, W.; Vergnes, B., Effect of processing conditions on the formation of polypropylene/organoclay nanocomposites in a twin screw extruder. *Polymer Engineering & Science* **2006,** 46, (3), 314-323.
35. Jollands, M.; Gupta, R. K., Effect of mixing conditions on mechanical properties of polylactide/montmorillonite clay nanocomposites. *Journal of Applied Polymer Science* **2010,** 118, (3), 1489-1493.
36. Scatteia, L.; Scarfato, P.; Acierno, D., Processing, rheology and structure of melt compounded PBT-clay nanocomposites having different chemical composition. *e-Polymers* **2006**.
37. Mittal, V., *Optimization of polymer nanocomposite properties*. Wiley. com: 2009.
38. Garge, S. C.; Wetzel, M. D.; Ogunnaike, B. A., On Control of Reactive Extrusion Processes. *AIChE Conference* **2006**.
39. Garge, S. C.; Wetzel, M. D.; Ogunnaike, B. A., Inference-based scheme for controlling product end-use properties in reactive extrusion processes. *Industrial & Engineering Chemistry Research* **2010,** 49, (17), 8021-8034.
40. Sinha Ray, S.; Okamoto, M., Polymer/layered silicate nanocomposites: a review from preparation to processing. *Progress in Polymer Science* **2003,** 28, (11), 1539-1641.
41. Wang, K. H.; Choi, M. H.; Koo, C. M.; Choi, Y. S.; Chung, I. J., Synthesis and characterization of maleated polyethylene/clay nanocomposites. *Polymer* **2001,** 42, (24), 9819-9826.
42. Fornes, T. D.; Hunter, D. L.; Paul, D. R., Effect of sodium montmorillonite source on nylon 6/clay nanocomposites. *Polymer* **2004,** 45, (7), 2321-2331.
43. Filippi, S.; Marazzato, C.; Magagnini, P.; Minkova, L.; Dintcheva, N. T.; La Mantia, F. P., Organoclay nanocomposites from ethylene-acrylic acid copolymers. *Macromolecular Materials and Engineering* **2006,** 291, (10), 1208-1225.
44. Cser, F.; Bhattacharya, S. N., Study of the orientation and the degree of exfoliation of nanoparticles in poly (ethylene-vinyl acetate) nanocomposites. *Journal of Applied Polymer Science* **2003,** 90, (11), 3026-3031.
45. Wang, S.; Hu, Y.; Zong, R.; Tang, Y.; Chen, Z.; Fan, W., Preparation and characterization of flame retardant ABS/montmorillonite nanocomposite. *Applied Clay Science* **2004,** 25, (1), 49-55.
46. Berghaus, U.; Hensen, F., *Plastics extrusion technology*. Hanser Verlag: 1997.

47. http://www.polymerprocessing.com/operations/tscrew/ts1.gif.
48. Chen, H.; Sundararaj, U.; Nandakumar, K.; Wetzel, M. D., Investigation of the melting mechanism in a twin-screw extruder using a pulse method and online measurement. *Industrial & Engineering Chemistry Research* **2004,** 43, (21), 6822-6831.
49. Booy, M. L., Geometry of fully wiped twin screw equipment. *Polymer Engineering & Science* **1978,** 18, (12), 973-984.
50. Potente, H.; Ansahl, J.; Klarholz, B., Design of tightly intermeshing co-rotating twin screw extruders. *International Polymer Processing(Germany)* **1994,** 9, (1), 11-25.
51. Eslami, H. Understanding screw design for film extrusion process. http://www.macroeng.com/understanding-screw-design-for-film-extrusion-process.php
52. Frankland, J. How much L/D do you really need? http://www.ptonline.com/columns/how-much-ld-do-you-really-need
53. McCrum, N. G.; Buckley, C. P.; Bucknall, C. B., Principles of polymer engineering. In Oxford University Press (Oxford and New York): 1997.
54. Rauwendaal, C. J., Analysis and experimental evaluation of twin screw extruders. *Polymer Engineering & Science* **1981,** 21, (16), 1092-1100.
55. White, J. L., *Twin screw extrusion: technology and principles*. Hanser Publishers: New York, 1991.
56. Rauwendaal, C., *Polymer extrusion*. Hanser Publishers: New York, 1990.
57. Strong, A. B., *Plastics: materials and processing*. 2nd ed.; Prentice-Hall, Inc.: Upper Saddle River, New Jersey, 2000.
58. Sharmin, R.; Sundararaj, U.; Shah, S.; Vande Griend, L.; Sun, Y.-J., Inferential sensors for estimation of polymer quality parameters: Industrial application of a PLS-based soft sensor for a LDPE plant. *Chemical Engineering Science* **2006,** 61, (19), 6372-6384.
59. Liu, X.; Li, K.; McAfee, M.; Nguyen, B. K.; McNally, G. M., Dynamic gray-box modeling for on-line monitoring of polymer extrusion viscosity. *Polymer Engineering & Science* 52, (6), 1332-1341.
60. Wang, L.; Chessari, C.; Karpiel, E., Inferential control of product quality attributes application to food cooking extrusion process. *Journal of Process Control* **2001,** 11, (6), 621-636.
61. Zhang, J.; Martin, E. B.; Morris, A. J.; Kiparissides, C., Inferential estimation of polymer quality using stacked neural networks. *Computers & Chemical Engineering* **1997,** 21, S1025-S1030.
62. Garge, S. C.; Wetzel, M. D.; Ogunnaike, B. A., Quantification of the melting process in a c-rotating twin-screw extruder: a hybrid modeling approach. *Polymer Engineering & Science* **2007,** 47, (7), 1040-1051.
63. Seborg, D.; Edgar, T. F.; Mellichamp, D., *Process dynamics & control*. Wiley. com: 2006.

64. Zehev Tadmor, I. K., *Engineering principles of plasticating extrusion*. Van Nostrand Reinhold Company: New York, 1970.
65. Iqbal, M. H.; Sundararaj, U.; Shah, S. L., New approach to develop dynamic gray box model for a plasticating twin-screw extruder. *Industrial & Engineering Chemistry Research* **2009,** 49, (2), 648-657.
66. Mudalamane, R.; Bigio, D. I., Process variations and the transient behavior of extruders. *Aiche Journal* **2003,** 49, (12), 3150-3160.
67. Haley, T. A.; Mulvaney, S. J., On-line system identification and control design of an extrusion cooking process: Part II. Model predictive and inferential control design. *Food Control* **2000,** 11, (2), 121-129.
68. Zagal, A.; Vivaldo-Lima, E.; Manero, O., A mathematical model for the reactive extrusion of methyl methacrylate in a co-rotating twin-screw extruder. *Industrial & Engineering Chemistry Research* **2005,** 44, (26), 9805-9817.
69. Choulak, S.; Couenne, F.; Le Gorrec, Y.; Jallut, C.; Cassagnau, P.; Michel, A., Generic dynamic model for simulation and control of reactive extrusion. *Industrial & Engineering Chemistry Research* **2004,** 43, (23), 7373-7382.
70. Chen, Z. L.; Chao, P. Y.; Chiu, S. H., Proposal of an empirical viscosity model for quality control in the polymer extrusion process. *Polymer Testing* **2003,** 22, (5), 601-607.
71. Pabedinskas, A.; Cluett, W. R., Controller design and performance analysis for a reactive extrusion process. *Polymer Engineering & Science* **1994,** 34, (7), 585-597.
72. Iqbal, M. H.; Sundararaj, U.; Shah, S. L., Identification of transient responses of a plasticating twin screw extruder due to excitation in feed rate. *Polymer Engineering & Science* **2011**, 482-491.
73. Trifkovic, M.; Sheikhzadeh, M.; Choo, K.; Rohani, S., Model identification of a twin screw extruder for thermoplastic vulcanizate (TPV) applications. *Polymer Engineering & Science* **2010,** 50, (6), 1168-1177.
74. Ozbek, M. O.; Bayram, G.; Ozgen, C., Molecular weight control of poly (ethylene terephthalate) in extrusion process. *Polymer Engineering & Science* **2014,** 54, 459-465.
75. Trifkovic, M.; Sheikhzadeh, M.; Choo, K.; Rohani, S., Model predictive control of a twin-screw extruder for thermoplastic vulcanizate (TPV) applications. *Computers & Chemical Engineering* **2011,** 36, 247-254.
76. Broadhead, T. O.; Patterson, W. I.; Dealy, J. M., Closed loop viscosity control of reactive extrusion with an in-line rheometer. *Polymer Engineering & Science* **1996,** 36, (23).
77. Potente, H.; Kretschmerz, K.; Pohl, T., Physico-Mathematical Model for the Description of the Temperature Development and the Power Consumption in Co-Rotating Twin Screw Extruders. *International Polymer Processing* **2004,** 19, (1), 3-12.
78. Shah, R. K., Polymer-layered silicate nanocomposites by melt processing. *Ph.D. dissertation, University of Texas at Austin* **2006**.
79. Xia, X.; Cai, S.; Xie, C., Preparation, structure and thermal stability of Cu/LDPE nanocomposites. *Materials Chemistry & Physics* **2006,** 95, (1), 122-129.

80. McNally, T.; Raymond Murphy, W.; Lew, C. Y.; Turner, R. J.; Brennan, G. P., Polyamide-12 layered silicate nanocomposites by melt blending. *Polymer* **2003,** 44, (9), 2761-2772.
81. Lin, B.; Thu¨men, A.; Heim, H.-P.; Scheel, G.; Sundararaj, U., Nylon 66/clay nanocomposite structure development in a twin screw extruder. *Polymer Engineering & Science* **2009,** 49, (4), 824-834.
82. Spencer, M. W.; Cui, L.; Yoo, Y.; Paul, D. R., Morphology and properties of nanocomposites based on HDPE/HDPE-g-MA blends. *Polymer* **2010,** 51, (5), 1056-1070.
83. Cui, L.; Paul, D. R., Evaluation of amine functionalized polypropylenes as compatibilizers for polypropylene nanocomposites. *Polymer* **2007,** 48, (6), 1632-1640.
84. Ozko, G.; Bayram, G.; Quaedflieg, M., Effects of microcompounding process parameters on the properties of ABS/polyamide-6 blends based nanocomposites. *Journal of Applied Polymer Science* **2008,** 107, (5), 3058-3070.
85. Breuer, O.; Sundararaj, U.; Toogood, R. W., The design and performance of a new miniature mixer for specialty polymer blends and nanocomposites. *Polymer Engineering & Science* **2004,** 44, (5), 868-879.
86. Zhu, L.; Xanthos, M., Effects of process conditions and mixing protocols on structure of extruded polypropylene nanocomposites. *Journal of Applied Polymer Science* **2004,** 93, (4).
87. Etelaaho, P.; Nevalainen, K.; Suihkonen, R.; Vuorinen, J.; Hanhi, K.; Jarvela, P., Effects of direct melt compounding and masterbatch dilution on the structure and properties of nanoclay-filled polyolefins. *Polymer Engineering & Science* **2009,** 49, (7), 1438-1446.
88. Borse, N. K.; Kamal, M. R., Melt processing effects on the structure and mechanical properties of PA-6/clay nanocomposites. *Polymer Engineering & Science* **2006,** 46, (8), 1094-1103.
89. Ghasemi, I.; Karrabi, M.; Mohammadi, M.; Azizi, H., Evaluating the effect of processing conditions and organoclay content on the properties of styrene-butadiene rubber/organoclay nanocomposites by response surface methodology. *Express Polym Lett* **2009,** 4, 62-70.
90. Kubisova, H.; Merinska, D.; Svoboda, P., PP/clay nanocomposite: optimization of mixing conditions with respect to mechanical properties. *Polymer bulletin* **2010,** 65, (5), 533-541.
91. Domenech, T.; Vergnes, B.; Peuvrel-Disdier, E. In *Influence of twin-screw processing conditions on structure and properties of polypropylene-organoclay nanocomposites*, 27th World Congress of the Polymer Processing Society, Marrakech: Morocco 2011; 2011.
92. Chaudhary, D. S.; Prasad, R.; Gupta, R. K.; Bhattacharya, S. N., Morphological influence on mechanical characterization of ethylene-vinyl acetate copolymer-clay nanocomposites. *Polymer Engineering & Science* **2005,** 45, (7), 889-897.

93. Wetzel, M. D., Kinematic, thermodynamic and structural factors governing the dispersion of nanoclays in polymer mels. *APE ANTEC Tech. Papers* **2012**, 1103-1112.
94. Ogunnaike, B. A., *Random phenomena: fundamentals of probability and statistics for engineers*. Taylor & Francis Group: Boca Raton, FL, 2009.
95. Pappas, W.; Brown Ii, H.; Fukuda, G.; Adnew, R.; Bigio, D., Variable strength stress break analysis in a twin screw extruder. In SPE ANTEC Tech. Papers: 2012.
96. Wetzel, M. D.; Denelsbeck, D. In *A perturbation method to characterize reactive extrusion*, ANTEC 2003 Conference Proceedings, 2003; 2003; pp 3791-3796.
97. Garge, S. C.; Wetzel, M. D.; Ogunnaike, B. A., Control-relevant model identification of reactive extrusion processes. *Journal of Process Control* **2012,** 22, (8), 1457-1467.
98. Cser, F.; Bhattacharya, S. N., Study of the orientation and the degree of exfoliation of nanoparticles in poly (ethylene vinyl acetate) nanocomposites. *Journal of Applied Polymer Science* **2003,** 90, (11), 3026-3031.
99. Morgan, A. B.; Gilman, J. W., Characterization of polymer layered silicate (clay) nanocomposites by transmission electron microscopy and X ray diffraction: A comparative study. *Journal of Applied Polymer Science* **2003,** 87, (8), 1329-1338.
100. Lee, H.; Fasulo, P. D.; Rodgers, W. R.; Paul, D. R., TPO based nanocomposites. Part 1. Morphology and mechanical properties. *Polymer* **2005,** 46, (25), 11673-11689.
101. Shah, R. K.; Kim, D. H.; Paul, D. R., Morphology and properties of nanocomposites formed from ethylene/methacrylic acid copolymers and organoclays. *Polymer* **2007,** 48, (4), 1047-1057.
102. Kim, D. H.; Fasulo, P. D.; Rodgers, W. R.; Paul, D. R., Structure and properties of polypropylene-based nanocomposites: Effect of PP-g-MA to organoclay ratio. *Polymer* **2007,** 48, (18), 5308-5323.
103. Zhao, J.; Morgan, A. B.; Harris, J. D., Rheological characterization of polystyrene-clay nanocomposites to compare the degree of exfoliation and dispersion. *Polymer* **2005,** 46, (20), 8641-8660.
104. Dolgovskij, M. K.; Macosko, C. W.; Lortie, F. In *Effects of stress on the exfoliation of polystyrene nanocomposites*, ANTEC, 2004; 2004; pp 1336-1340.
105. Ploehn, H. J.; Liu, C., Quantitative analysis of montmorillonite platelet size by atomic force microscopy. *Industrial & Engineering Chemistry Research* **2006,** 45, (21), 7025-7034.
106. Bourbigot, S.; Vanderhart, D. L.; Gilman, J. W.; Bellayer, S.; Stretz, H.; Paul, D. R., Solid state NMR characterization and flammability of styrene-acrylonitrile copolymer montmorillonite nanocomposite. *Polymer* **2004,** 45, (22), 7627-7638.
107. Tavares, B.; Ines, M.; da Silva, P. S.; da Silva, E.; Legramanti, C.; Passos, A.; Cucinelli Neto, R. In *The evaluation polymeric nanocomposites from nuclear magnetic resonance relaxometry*, ICQNM 2012, The Sixth International Conference on Quantum, Nano and Micro Technologies, 2012; 2012; pp 52-55.
108. Paul, D. R.; Robeson, L. M., Polymer nanotechnology: nanocomposites. *Polymer* **2008,** 49, (15), 3187-3204.

109. Eckel, D. F.; Balogh, M. P.; Fasulo, P. D.; Rodgers, W. R., Assessing organo-clay dispersion in polymer nanocomposites. *Journal of Applied Polymer Science* **2004,** 93, (3), 1110-1117.
110. Luo, Z. P.; Koo, J. H., Quantification of the layer dispersion degree in polymer layered silicate nanocomposites by transmission electron microscopy. *Polymer* **2008,** 49, (7), 1841-1852.
111. Tyson, B. M.; Abu Al-Rub, R. K.; Yazdanbakhsh, A.; Grasley, Z., A quantitative method for analyzing the dispersion and agglomeration of nano-particles in composite materials. *Composites Part B: Engineering* **2011,** 42, (6), 1395-1403.
112. Bray, D. J.; Gilmour, S. G.; Guild, F. J.; Taylor, A. C., Quantifying nanoparticle dispersion by using the area disorder of Delaunay triangulation. *Journal of the Royal Statistical Society: Series C (Applied Statistics)* **2012,** 61, (2), 253-275.
113. Nam, P. H.; Maiti, P.; Okamoto, M.; Kotaka, T.; Hasegawa, N.; Usuki, A., A hierarchical structure and properties of intercalated polypropylene/clay nanocomposites. *Polymer* **2001,** 42, (23), 9633-9640.
114. Carastan, D. J.; Vermogen, A.; Masenelli Varlot, K.; Demarquette, N. R., Quantification of clay dispersion in nanocomposites of styrenic polymers. *Polymer Engineering & Science* **2010,** 50, (2), 257-267.
115. Vermogen, A.; Masenelli-Varlot, K.; Roland, S.; Duchet-Rumeau, J.; Boucard, S.; Prele, P., Evaluation of the structure and dispersion in polymer-layered silicate nanocomposites. *Macromolecules* **2005,** 38, (23), 9661-9669.
116. Ogunnaike, B. A., *Random phenomena: fundamentals of probability and statistics for engineers*. CRC Press: 2010.
117. Fornes, T. D.; Paul, D. R., Modeling properties of nylon 6/clay nanocomposites using composite theories. *Polymer* **2003,** 44, (17), 4993-5013.
118. Shah, R. K.; Paul, D. R., Comparison of nanocomposites prepared from sodium, zinc, and lithium ionomers of ethylene/methacrylic acid copolymers. *Macromolecules* **2006,** 39, (9), 3327-3336.
119. Chavarria, F.; Paul, D. R., Comparison of nanocomposites based on nylon 6 and nylon 66. *Polymer* **2004,** 45, (25), 8501-8515.
120. Iqbal, M. H., *Advanced control of the twin screw extruder*. 2010; Vol. 72.
121. Ogunnaike, B. A.; Ray, W. H., *Process dynamics, modeling, and control*. Oxford University Press New York: 1994; Vol. 9.
122. Zhu, Y., *Multivariable system identification for process control*. Elsevier: 2001.
123. Skogestad, S.; Postlethwaite, I., Multivariable feedback control: analysis and design. *New York* **1996**.
124. Gurovich, D.; Macosko, C. W.; Tirrell, M., The influence of filler-filler and filler-polymer interactions on the physical properties of silica-filled liquid polyisoprene. *Rubber chemistry and technology* **2004,** 77, (1), 1-12.
125. Tulleken, H. J. A. F., Generalized binary noise test-signal concept for improved identification-experiment design. *Automatica* **1990,** 26, (1), 37-49.

126. Camacho, E. F.; Bordons, C., *Model predictive control*. Springer London: 2004; Vol. 2.
127. Lawrence, M.; Erdem, G.; Abel, S.; Morari, M.; Mazzotti, M.; Morbidelli, J. L., Online optimisation and feedback control of a SMB plant: a LabVIEW matlab procedural implementation. *Virtuelle Instrumente in der Praxis* **2004**.
128. Garge, S. C.; Ogunnaike, B. A. In *Customer feedback control for assuring acceptable product end-use performance*, AIChE Conference, 2007; 2007.
129. Hosmer, D. W.; Lemeshow, S., *Applied logistic regression*. Wiley-Interscience: 2000; Vol. 354.
130. Gut, A., *An intermediate course in probability*. Springer: 2009.
131. Muirhead, R. J., *Aspects of multivariate statistical theory*. Wiley. com: 2009; Vol. 197.
132. Higginson, R. L.; Sellars, C. M., *Worked examples in quantitative metallography*. Maney: 2003.
133. Singh, R. P.; Zhang, M.; Chan, D., Toughening of a brittle thermosetting polymer: effects of reinforcement particle size and volume fraction. *Journal of materials science* **2002,** 37, (4), 781-788.
134. Thostenson, E. T.; Li, C.; Chou, T.-W., Nanocomposites in context. *Composites Science and Technology* **2005,** 65, (3), 491-516.
135. Khare, H. S.; Burris, D. L., A quantitative method for measuring nanocomposite dispersion. *Polymer* 51, (3), 719-729.
136. Mukati, K.; Rasch, M.; Ogunnaike, B. A., An alternative structure for next generation regulatory controllers. Part II: Stability analysis, tuning rules and experimental validation. *Journal of Process Control* **2009,** 19, (2), 272-287.
137. Halpin, J. C.; Pagano, N. J., The laminate approximation for randomly oriented fibrous composites. *Journal of composite materials* **1969,** 3, (4), 720-724.
138. Ashton, J. E.; Halpin, J. C.; Petit, P. H., *Primer on composite materials: analysis*. Technomic Publishing Company: 1969.
139. http://www.matweb.com/search/DataSheet.aspx?MatGUID=06db83714082407b93b245f98b086476
140. http://www.matweb.com/search/datasheet.aspx?matguid=85d5971e2c084a0a9f7e246fcbbcf3c1
141. Clark, S. P., *Handbook of physical constants*. Geological Society of America: 1966; Vol. 97.
142. http://www.matweb.com/search/datasheet.aspx?MatGUID=3181d0899a0b46a592eb37c47f0f841b
143. Costin, M. H.; Taylor, P. A.; Wright, J. D., A critical review of dynamic modeling and control of plasticating extruders. *Polymer Engineering & Science* **1982,** 22, (7), 393-401.

144. Marlin, T. E.; Marlin, T. E., *Process control: designing processes and control systems for dynamic performance*. McGraw-Hill New York: 1995; Vol. 2.
145. Stewart, J., *Multivariable calculus: concepts and contexts*. Cengage Learning: 2009.

## Appendix A

## TEM MICROGRAPHS USED FOR IMAGE ANALYSIS

This appendix includes all the TEM micrographs used for image analysis in Chapter 4. Figure A-1 shows the TEM images for Sample 1, while Figure A-2 shows the TEM images for Sample 2.

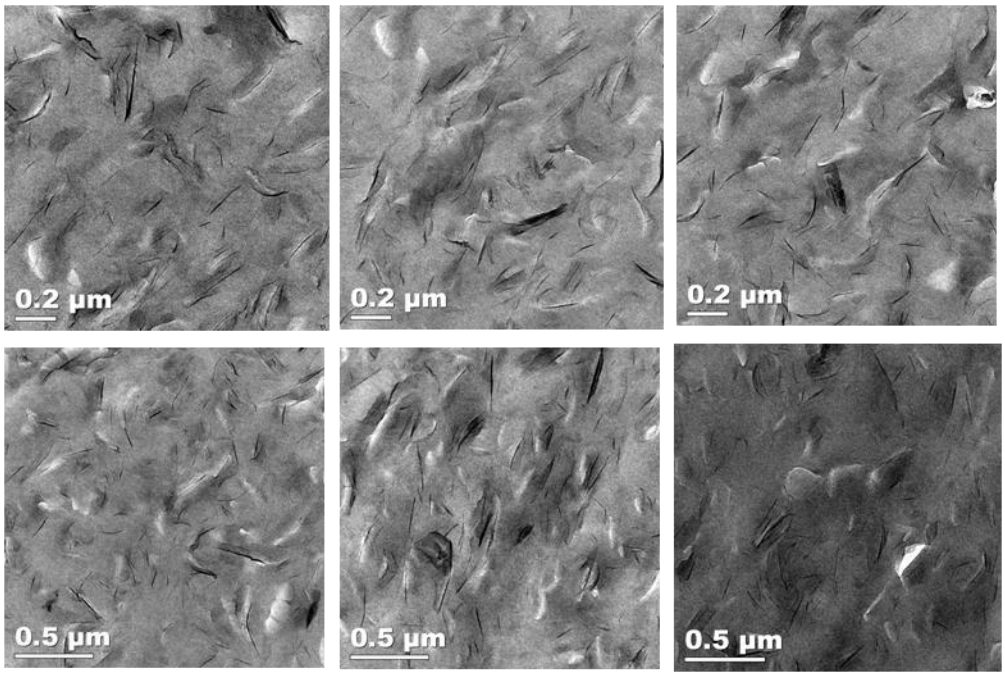


Figure A-1: TEM micrographs for image analysis of Sample 1

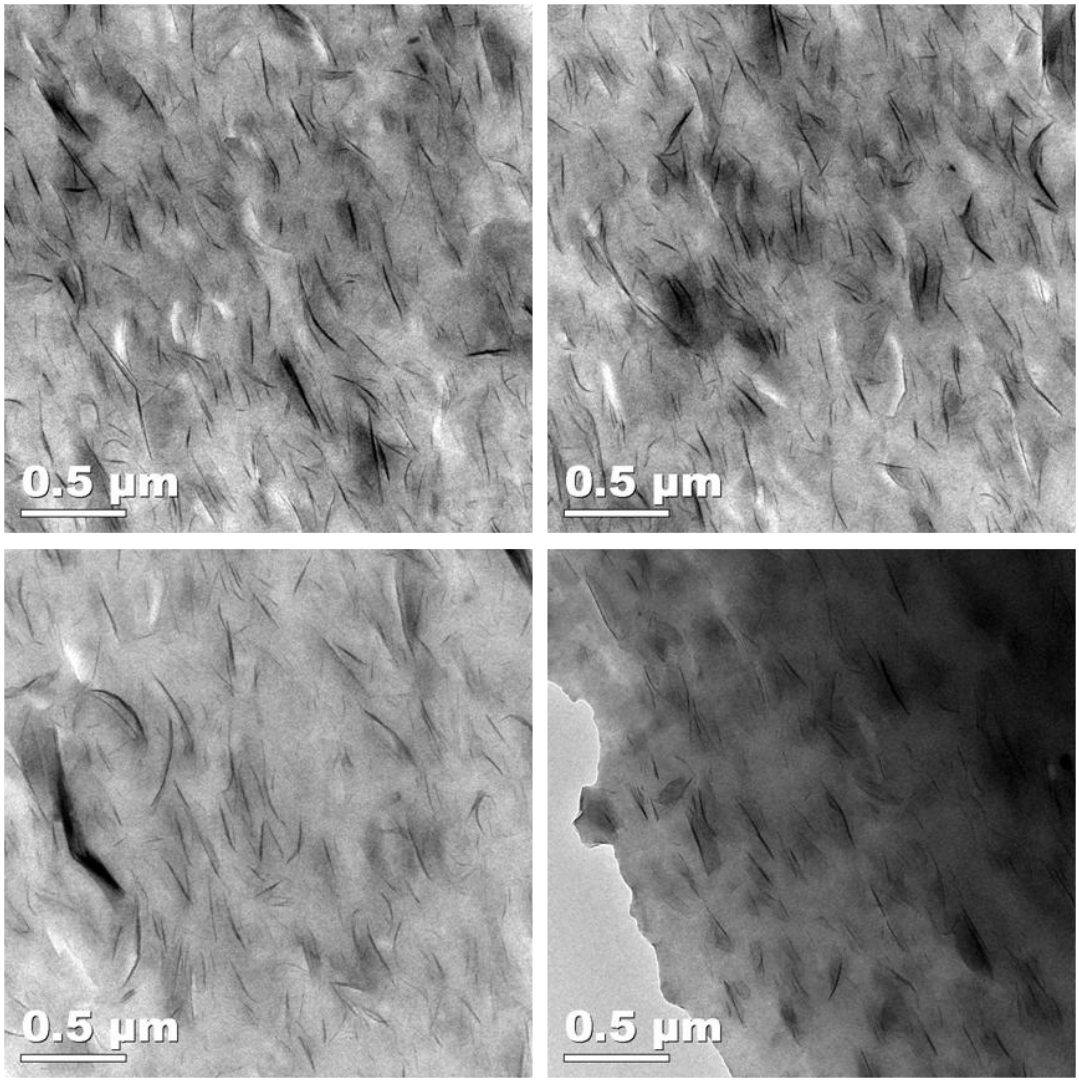


Figure A-2: TEM micrographs for image analysis of Sample 2

## Appendix B

## SCATTER PLOT OF $\alpha$ VERSUS $\beta$ WITH ERROR BARS FOR VARIOUS POLYMER NANOCOMPOSITES

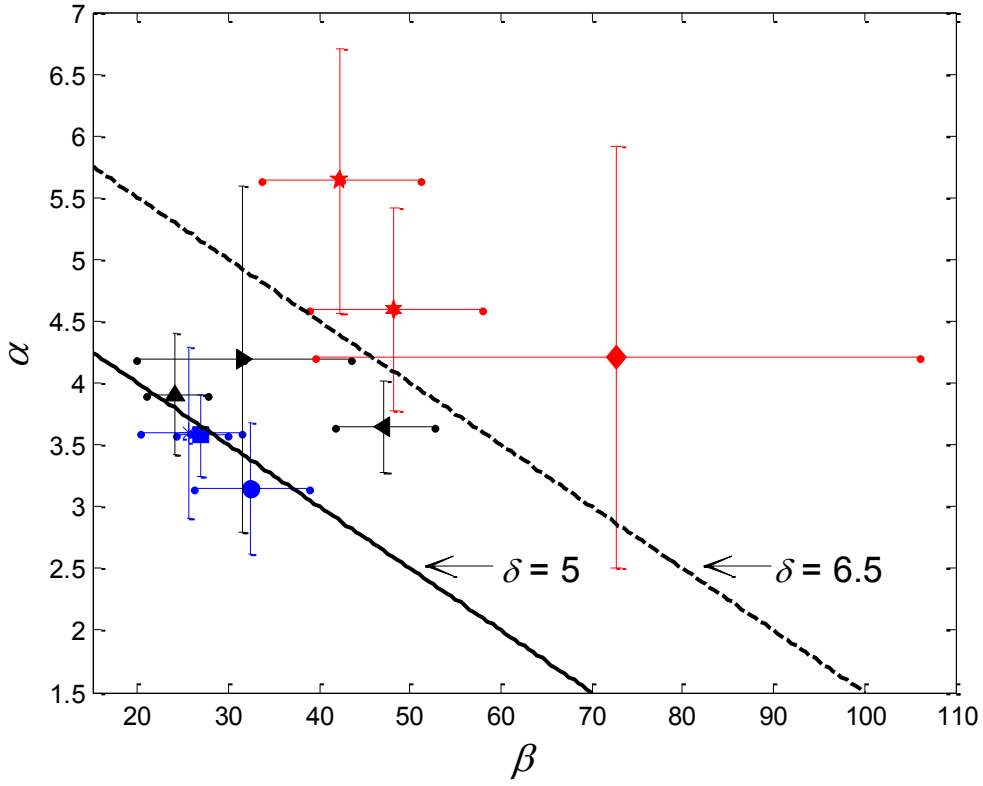


Figure B-1: Scatter plot of $\alpha$ versus $\beta$ for various polymer nanocomposites: * for PA-6/$(HE)_2M_1R_1$-YM NC; ● for PA-6/$(HE)_2M_1R_1$-WY NC; ■ for Zn ionomer/$M_2(HT)_2$ NC; ▲ for Na ionomer/$M_2(HT)_2$ NC; ► for EMAA-1/$M_2(HT)_2$ NC; ◄ for Li ionomer/$M_2(HT)_2$ NC; ♦ for PP/$M_2(HT)_2$ NC (1wt%); six-pointed star in red PP/$M_2(HT)_2$ NC (2.8wt%), five-pointed star in red for PP/$M_2(HT)_2$ NC (6.8wt%). The error bars represent 95% confidence intervals. The indicated lines are "dispersion contours" represented by $\alpha + 0.05\beta = \delta$

## Appendix C

## PRELIMINARY WORK OF ESTABLISHING INFERENCE MODELS BASED ON HALPIN-TSAI COMPOSITE THEORY

In this appendix, we present some initial efforts towards establishing inference models for predicting nanocomposites' end-use properties. As discussed in section 8.2.1.2, to establish such inference models, it is necessary to relate the dispersion index, $\delta$, to end-use properties based on composite theories. One of the most widely used composite theories developed by Halpin-Tsai is well known for predicting the stiffness of unidirectional composites as a function of aspect ratio [137].

In the Halpin-Tsai theory, the longitudinal and transverse engineering moduli, are shown in the following form:

$$\frac{E}{E_m} = \frac{1+\zeta\eta\phi_f}{1-\eta\phi_f} \qquad \text{C-1}$$

where $E$ and $E_m$ represent the modulus of the composite and matrix, respectively, $\phi_f$ is the volume fraction of the filler, $\zeta$ is a shape parameter associated with loading direction and filler geometry, and $\eta$ is represented by:

$$\eta = \frac{E_f/E_m - 1}{E_f/E_m + \zeta} \qquad \text{C-2}$$

where $E_f$ represent the modulus of the filler. It is important to note that $\zeta$ was determined to be related to the aspect ratio of the filler in the polymer matrix. Specifically, for the case of MMT as the filler, $\zeta$ is given by [138]:

$$\zeta = 2(l/t) \qquad \text{C-3}$$

where $l$ and $t$ are the length and thickness of the dispersed platelet, respectively, and thus ($l/t$) represents the aspect ratio of the platelet, which is the direct indicator of clay dispersion in the polymer matrix.

Based on this theory, we illustrate how to relate $\delta$ to ($l/t$) and further to the modulus of nanocomposites, using the two in-house samples presented in Chapter 4 as examples. The physical properties of the materials used for preparing nanocomposites are listed in Table C-1, where the modulus of Na ionomer was obtained by tensile testing experiments in our lab and the modulus of organoclays is the modulus of MMT. The mechanical properties of the two samples are shown in Table C-2, where the volume fraction of the filler is computed from the weight fraction of the filler, $\phi_{fw}$, by the following equation:

$$\phi_f = \frac{\phi_{fw}}{\phi_{fw}+(1-\phi_{fw})\frac{\rho_f}{\rho_m}} \qquad \text{C-4}$$

where $\rho_m$ and $\rho_f$ are the density of the polymer and the filler, respectively. Also, the density of the organoclay mixture for Sample 2 was determined as 1.79 g/cm$^3$.

Then, we predict the aspect ratio for each sample using the modulus (see Table C-2) based on the Halpin-Tsai equations C-1 and C-2. The results are shown in Table C-3, which indicate that both aspect ratio and dispersion index can quantify the clay dispersion effectively. Now, the dispersion index can be related to the aspect ratio using mathematical equations; therefore $M_{\delta w}$ is able to be developed for linking the dispersion index to composite's modulus. In this appendix, we showed the procedure of establishing $M_{\delta w}$; however, to determine such a model, it is necessary to obtain modulus and dispersion index data for a sequence of different processing conditions and 20A concentrations.

Table C-1: Physical properties of polymer (Surlyn® 8945) and organoclays (Cloisite® 20A and Cloisite® 93A)

| Material | Density ($g/cm^3$) | Modulus (GPa) |
|---|---|---|
| Surlyn® 8945 | 0.95 [139] | 0.15 |
| Cloisite® 20A | 1.77 [140] | 178 [141] |
| Cloisite® 93A | 1.88 [142] | |

Table C-2: Dispersion characteristics of Sample 1 (Na ionomer/$M_2(HT)_2$ nanocomposites) and Sample 2 (Na ionomer/organoclay mixture nanocomposites)

| Sample number | Materials | wt. % MMT | vol. % MMT | Modulus (GPa) |
|---|---|---|---|---|
| 1 | Na ionomer/20A NC | 5.0 | 2.75 | 0.274 |
| 2 | Na ionomer/organoclay mixture NC (20A:93A = 20:80) | 5.0 | 2.72 | 0.225 |

Table C-3: Predicted aspect ratios and corresponding dispersion indexes for Sample 1 (Na ionomer/$M_2(HT)_2$ nanocomposites) and Sample 2 (Na ionomer/organoclay mixture nanocomposites)

| Sample number | Materials | Aspect ratio, $l/t$ | Dispersion index, $\delta$ |
|---|---|---|---|
| 1 | Na ionomer/20A NC | 16.45 | 5.85 ± 0.69 |
| 2 | Na ionomer/organoclay mixture NC (20A:93A = 20:80) | 10.15 | 6.96 ± 0.82 |

## Appendix D

## IDENTIFIED MISO MODELS FOR THE EXTRUSION PROCESS

Motor power MISO model (BJ):

$$
\begin{aligned}
&y(t) \\
&= \frac{5.204q^{-1} - 1.184q^{-2} - 3.838q^{-3}}{1 - 3.052q^{-1} + 4.345q^{-2} - 3.768q^{-3} + 1.863q^{-4} - 0.386q^{-5}}u_1(t) \\
&+ \frac{0.839q^{-1} - 1.284q^{-2} - 0.444q^{-3}}{1 - 3.28\,q^{-1} + 4.841q^{-2} - 4.716q^{-3} + 3.033q^{-4} - 0.878q^{-5}}u_2(t) \\
&+ \frac{-19.45q^{-1} - 9.808q^{-2} - 35.51q^{-3}}{1 + 0.610q^{-1} - 0.272q^{-2} + 0.290q^{-3} - 0.575q^{-4} - 0.866q^{-5}}u_3(t) \\
&+ \frac{1 - 0.421q^{-1} - 0.424q^{-2}}{1 - 0.997q^{-1}}e(t)
\end{aligned}
\qquad \text{D-1}
$$

Clay content MISO model (ARMAX):

$$
\begin{aligned}
(1 - 0.986q^{-1} - 0.003q^{-2})y(t) \\
= (-1.82 + 1.76q^{-1})u_1(t) + (8.76 - 8.65q^{-1})u_2(t) + (10.44 \\
- 10.3q^{-1})u_3(t) + (1 + 0.042q^{-1})e(t)
\end{aligned}
\qquad \text{D-2}
$$

20A content MISO model (BJ):

$$
\begin{aligned}
y(t) = \frac{-0.124 + 0.124q^{-1}}{1 - 1.078q^{-1} + 0.078q^{-2}}u_1(t) + \frac{20.64 - 20.54q^{-1}}{1 - 1.004q^{-1} + 0.009q^{-2}}u_2(t) \\
+ \frac{-35.97 + 34.86q^{-1}}{1 - 0.926q^{-1} - 0.042q^{-2}}u_3(t) + e(t)
\end{aligned}
\qquad \text{D-3}
$$

# Appendix E

# STABILITY ANALYSIS OF THE INNERMOST CONTROL LOOP

In the multivariable cascade-type control scheme, the performance of the innermost loop is very important to the success of the overall control scheme. As one of the keys to high performance control, the stability of the innermost loop needs to be analyzed. As discussed in section 5.2, the motor power is as an indicator to clay dispersion in polymer matrix, and it can be measured on-line in a much faster and cheaper way compared to other methods for quantifying dispersion. Therefore, we only focus on motor power.

In this appendix, we first study the dynamics of twin screw extruder process. Characteristics of the motor power response identified by the dynamics study provide insight into the design and the stability of the closed-loop control system. Then, we conduct stability study of the innermost control loop and propose criteria for selecting controller parameters.

## E.1 Process Dynamics: Frequency Response and Process Disturbances

The dynamics of motor power were conducted via frequency responses. The advantage of this method is that it is convenient to correlate the frequency characteristics of motor power with the process disturbances. Based on the frequency ranges of disturbances, the disturbances in the twin screw extruder process (see section 2.4.1) are typically classified into four categories [143]:

- High frequency disturbances: The frequency of these disturbances occurs at the same frequency as the screw rotations (e.g., 1 rad/sec at a screw speed of 60 rpm). The disturbances are mainly caused by the rotations of the twin screws in the barrel and of the feeders when operated at high feed-rate.

- Intermediate frequency disturbances: The frequency of this class of disturbances is often in the range of 1 – 15 cycles/min (~$10^{-2}$ to 0.25 rad/sec). The origin of the disturbances is often attributed to mixing, melting and reaction mechanisms of polymers/fillers in the extruder. Feeder oscillations (at low feed-rate) are also involved in this class.

- Low frequency disturbances: This frequency component has a period of around 3 min (~$10^{-3}$) usually due to the process drift and feedstock change.

Using the BJ model for motor power response (see Equation E-1), we obtained the transfer functions $G_{11}$, $G_{12}$, and $G_{13}$ corresponding to Na ionomer feed-rate, 20A feed-rate, and 93A feed-rate, respectively. The results are shown in the following equations.

$$G_{11} = \frac{1.271s^4 + 6.588s^3 + 16.12s^2 + 16.41s + 0.3239}{s^5 + 0.9518s^4 + 1.657s^3 + 1.143s^2 + 0.265s + 0.005} \quad \text{E-1}$$

$$G_{12} = \frac{0.3417s^4 + 0.9978s^3 + 1.296s^2 + 0.4957s - 0.0002}{s^5 + 0.1302s^4 + 1.929s^3 + 0.1487s^2 + 0.0045s} \quad \text{E-2}$$

$$G_{13} = \frac{40.35s^4 - 33.39s^3 - 53.77s^2 - 136.1s + 17.73}{s^5 + 0.1438s^4 + 10.85s^3 + 0.8799s^2 + 17.45s + 0.532} \quad \text{E-3}$$

The frequency responses of $G_{11}$, $G_{12}$, and $G_{13}$ are shown in Figures E-1, E-2, and E-3, separately. The results shed light on the characteristics of the motor power response with regard to the process disturbances. First, the frequency responses of motor power to the three feed-rates are greatly damped in high frequency, which

indicates that the effect of screw rotation on motor power is very brief. Second, the intermediate frequency disturbances play dominant effects on the variations in the motor responses to the three feed-rates, which illustrates that the mixing and melting process of polymers and fillers are the major contributions to the disturbances in motor power. Third, the low frequency disturbances also affect the fluctuation in motor power responses to 20A feed-rate and 93A feed-rate, but not to Na ionomer feed-rate. Since 20A and 93A clays were fed through the same feeder, the feed composition changed, which is a low frequency disturbance. At last, the very low frequency disturbances ($< 10^{-3}$) show in the motor response to 20A feed-rate. This observation indicates that the external disturbances (e.g., moisture content of the feed) affect the motor power through the 20A feed-rate.

These characteristics of the motor power show that it is the low and intermediate frequency disturbances that of concern when it comes to controller design. Therefore, the objective of the innermost loop control is to reject the low frequency disturbances and minimize the effects of intermediate frequency disturbances to cover the frequency band of expected disturbances. This conclusion leads to the use of a PI controller for controlling the single motor power variable in the innermost loop, which is capable of rejecting low frequency disturbances. Note that, in this thesis, we employed a MPC for the innermost loop control, since the process of interest is a MIMO system (see Chapter 5).

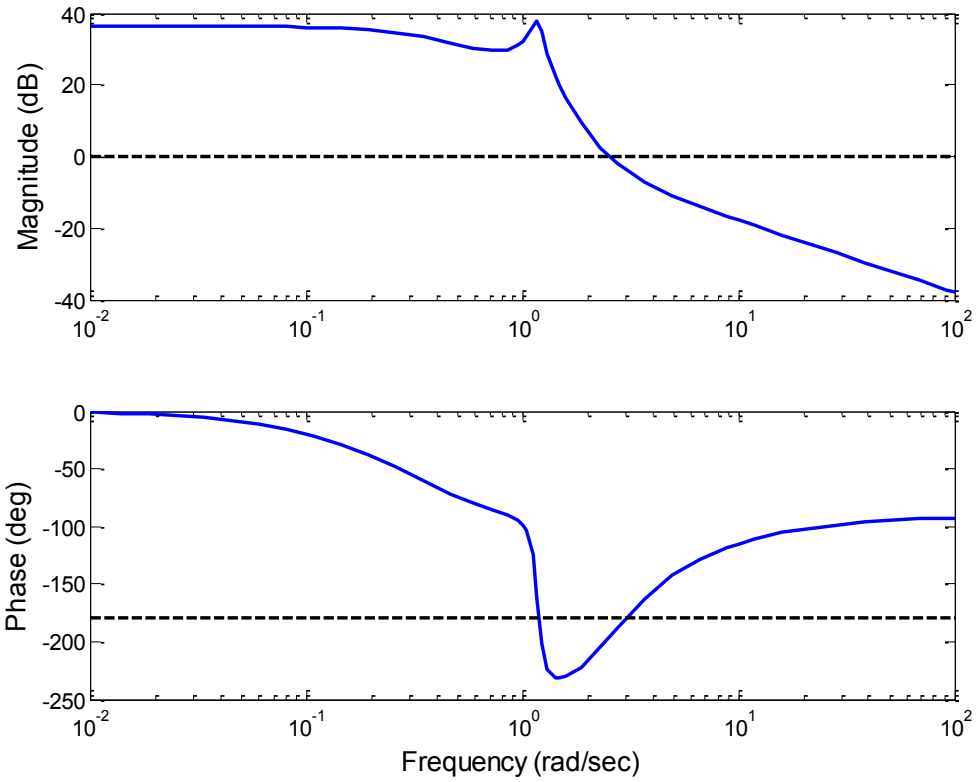


Figure E-1: Frequency response of the process $G_{11}$, the transfer function relating motor power to Na ionomer feed-rate

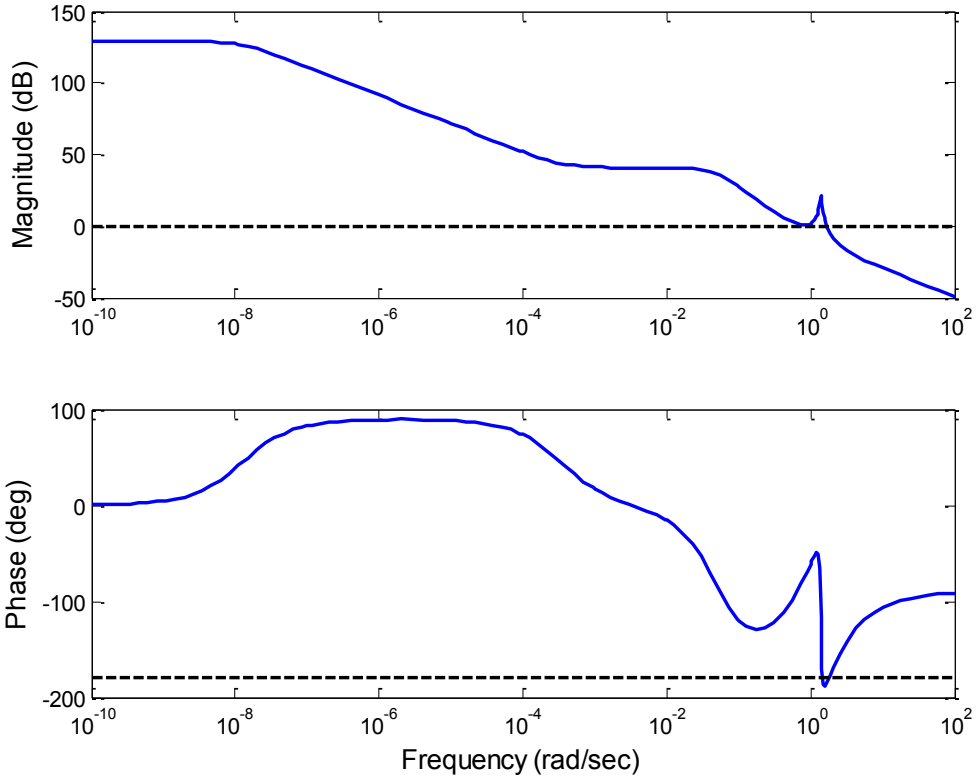


Figure E-2: Frequency response of the process $G_{12}$, the transfer function relating motor power to 20A feed-rate

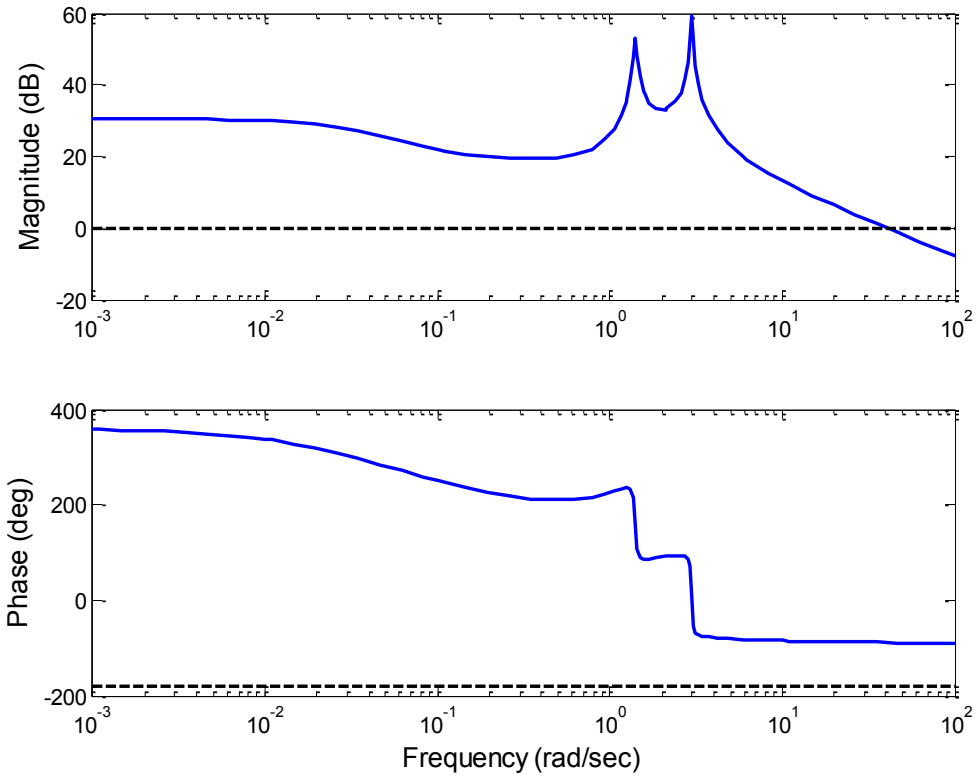


Figure E-3: Frequency response of the process $G_{13}$, the transfer function relating motor power to 93A feed-rate

## E.2 Stability Analysis: Root Locus Method

To study the close-loop stability of the innermost control loop, it is necessary to determine the controller type first. In this thesis, we employed the most basic controller for each input, the proportional controller. Specifically, $K_{11}$, $K_{12}$, $K_{13}$ are the controller gains for three input variables, respectively.

One of the tools for stability analysis of closed-loop system is the Bode plot. Unfortunately, this method cannot be used in this case, because the phase responses for the three open loop transfer functions $K_{11}G_{11}$, $K_{12}G_{12}$, and $K_{13}G_{13}$ (see Figures E-1, E-2, and E-3) exhibits non-monotonic phase angles [144]. Notice that gains do not affect the phase responses, so the phase responses of $K_{11}G_{11}$, $K_{12}G_{12}$, and $K_{13}G_{13}$ are the same as those of $G_{11}$, $G_{12}$, and $G_{13}$. We employ root locus analysis to study the stability of the innermost control loop. The results are shown in Figures E-4, E-5, and E-6 for three input variables, respectively. These figures depict the roots of the close-loop characteristic equations as the gain values vary. From the control theory, the close-loop is stable if all the roots have negative real parts. Therefore, we determined the critical point for each input variable, which was obtained by finding the gain value corresponding to the roots on the imaginary axis. The resulting stability regions are listed as follows.

$$K_{11} \in [0, 0.01135] \cup [1.5342, +\infty] \quad \text{E-4}$$

$$K_{12} \in [0, 0.21] \cup [1.55, +\infty] \quad \text{E-5}$$

$$K_{13} \in [0, 0.0023] \quad \text{E-6}$$

Equation E-6 shows that the stability region corresponding to the motor power relating to 93A feed-rate is really small, which indicates that only proportional

controller is not good enough for rejecting the disturbances from 93A feed-rate. Therefore, more sophisticated controller needs to be considered to ensure the stability of the innermost control loop as well as reject the disturbances in motor power response. This conclusion also provides theoretical support of using MPC for the innermost control loop in Chapter 5.

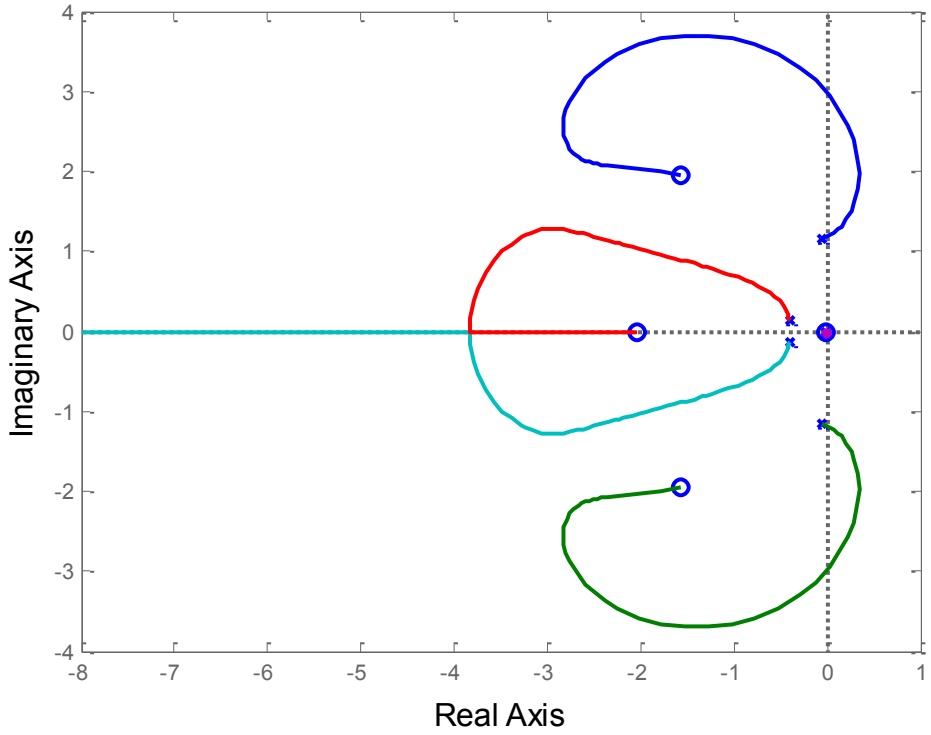


Figure E-4: Root locus of the close-loop characteristic equation $1 + K_{11}G_{11} = 0$, where $G_{11}$ is the transfer function relating motor power to Na ionomer feed-rate

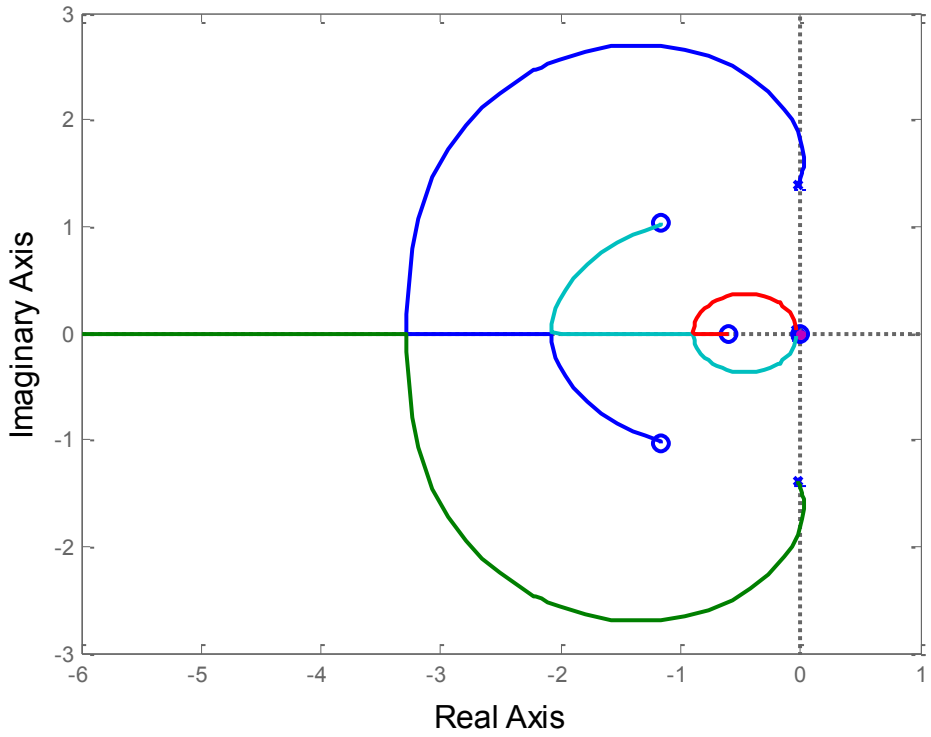


Figure E-5: Root locus of the close-loop characteristic equation $1 + K_{12}G_{12} = 0$, where $G_{12}$ is the transfer function relating motor power to 20A feed-rate

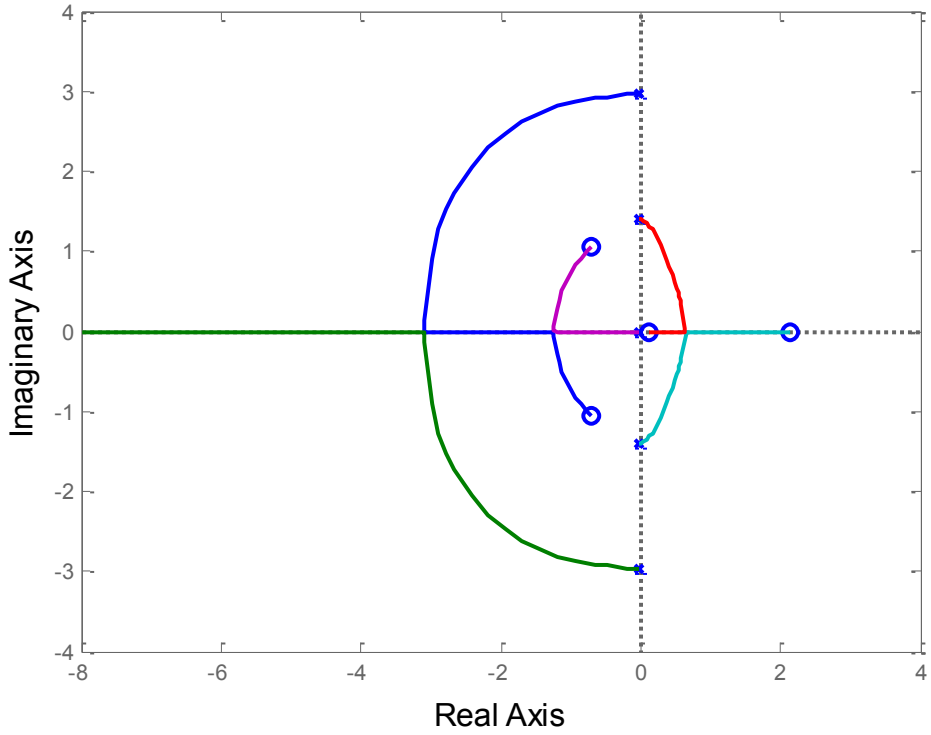


Figure E-6: Root locus of the close-loop characteristic equation $1 + K_{13}G_{13} = 0$, where $G_{13}$ is the transfer function relating motor power to 93A feed-rate

## Appendix F

## THEORETICAL CONTROL SYSTEM STABILITY

A theoretical stability study is conducted for the two inner-most control loops without the customer feedback loop, as shown in Figure F-1. Since the sampling time for the outermost customer feedback loop is of the order of days or weeks—significantly longer by far than the slowest plant characteristic response time—the sampling time of the third, outermost loop will have no effect on overall control system stability.

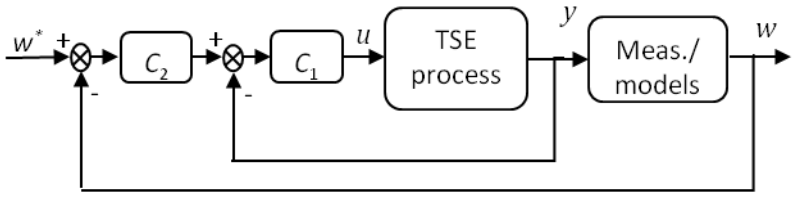


Figure F-1: Control scheme used for the theoretical stability study

The objective of this study is to establish guidelines for selecting sampling frequencies. The stability study was conducted via simulation, to characterize the effects of two distinct sample times, $ts_1$ for the inner loop (usually of the order of seconds/minutes in practice), and $ts_2$ for the outer loop (usually of the order of hours in practice), on the multi-rate cascade system's overall stability. To conduct such a stability study theoretically, we first determined the pulse transfer function of the

control system, from which the characteristic equation of the control system was obtained. Based on the characteristic equation, the control scheme's stability was then analyzed, and the sensitivity analysis was carried out.

## F.1 Pulse Transfer Function of the Control Scheme

We assume relatively simple nominal first-order-plus-time delay dynamics for the process characteristics in each loop (see Equations F-1 and F-2 for inner loop and outer loop, respectively), a zero-order hold (ZOH) element in front of each process, and proportional controller for each controller (the controller parameters are $k_{p1}$ and $k_{p2}$ for $C_1$ and $C_2$ respectively).

$$G_1 = \frac{K_1}{\tau_1 s+1} e^{-\alpha_1 s} \qquad \text{F-1}$$

$$G_2 = \frac{K_2}{\tau_2 s+1} e^{-\alpha_2 s} \qquad \text{F-2}$$

Based on these assumptions, the pulse transfer function of the control scheme shown in Figure F-1 was obtained as follows.

$$\begin{aligned} G(z) &= \frac{k_{p2} \cdot G_{in}(z) \cdot g_2(z)}{1 + k_{p2} \cdot G_{in}(z) \cdot g_2(z)} \\ g_2(z) &= K_2 z^{-\frac{\alpha_2}{ts_2}} \cdot \frac{(1-\phi_2) \cdot z^{-1}}{1-\phi_2 \cdot z^{-1}}, \phi_2 = e^{-\frac{ts_2}{\tau_2}} \end{aligned} \qquad \text{F-3}$$

where

$$\begin{aligned} G_{in}(z) &= \frac{k_{p1} \cdot g_1(z)}{1 + k_{p1} \cdot g_1(z)} \\ g_1(z) &= K_1 z^{-\frac{\alpha_1}{ts_1}} \cdot \frac{(1-\phi_1) \cdot z^{-1}}{1-\phi_1 \cdot z^{-1}}, \phi_1 = e^{-\frac{ts_1}{\tau_1}} \end{aligned} \qquad \text{F-4}$$

In the above equations, $g_1(z)$ and $g_2(z)$ are the pulse transfer functions of sampled continuous processes with ZOH elements for inner loop and outer loop, respectively.

Then, the characteristic equation of the control scheme was obtained by setting the denominator of the pulse transfer function (Equation F-3) to zero. The resulting characteristic equation is shown in the following equation:

$$z^{\frac{\alpha_1}{ts_1}+\frac{\alpha_2}{ts_2}+2} - (\phi_1+\phi_2)z^{\frac{\alpha_1}{ts_1}+\frac{\alpha_2}{ts_2}+1} + Hz^{\frac{\alpha_2}{ts_2}+1} + \phi_1\phi_2 z^{\frac{\alpha_1}{ts_1}+\frac{\alpha_2}{ts_2}} - H\phi_2 z^{\frac{\alpha_2}{ts_2}} + R = 0 \qquad \text{F-5}$$

where

$$\begin{aligned} H &= k_{p1}\cdot K_1\cdot(1-\phi_1); \\ R &= k_{p1}\cdot k_{p2}\cdot K_1\cdot K_2\cdot(1-\phi_1)\cdot(1-\phi_2) \end{aligned} \qquad \text{F-6}$$

## F.2 The Effects of $ts_1$ and $ts_2$ on the Multi-rate Cascade System's Stability

The characteristic equation may now be used to determine the set of $ts_1$ and $ts_2$ such that the closed-loop system is stable (i.e., all roots of the characteristic equation are within the unit circle). We employed Equation F-5 to generate Figures F-2 ($ts_2$ is constant) and F-3 ($ts_1$ is constant), a plot of closed-loop stability regions as a function of $K_1$ and $K_2$. The region below each curve is the stability region.

The simulation results indicate, among other things, that $ts_1$ exerts the dominant effect on overall system stability (the stability region expands as $ts_1$ increases), while $ts_2$, beyond a critical value, exerts no effect on stability (the stability region does not change after a critical value of $ts_2$). These results imply that once the stability of the inner loop (concerned with the control of the frequently measurable process variables) is established for a given sampling time, the companion sampling time for the outer loop should be selected to be at least as long as the critical value necessary for overall system stability.

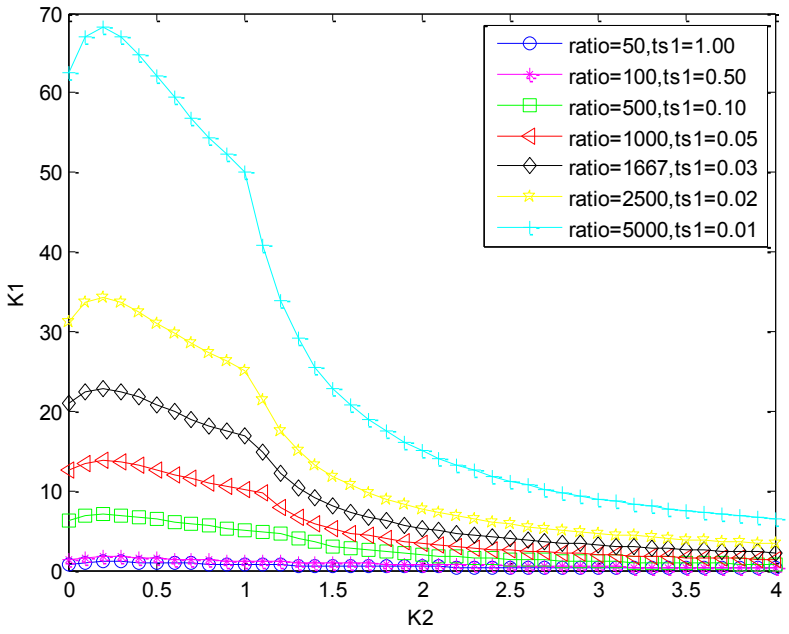


Figure F-2: Stability regions for the multi-rate cascade system: $ts_2 = 50$, $\tau_1 = \tau_2 = 1$, $k_{p1} = k_{p2} = 2$, and $\frac{\alpha_1}{ts_1} = \frac{\alpha_2}{ts_2} = 1$. Ratio is defined as $\frac{ts_2}{ts_1}$. The region below each curve is the stability region

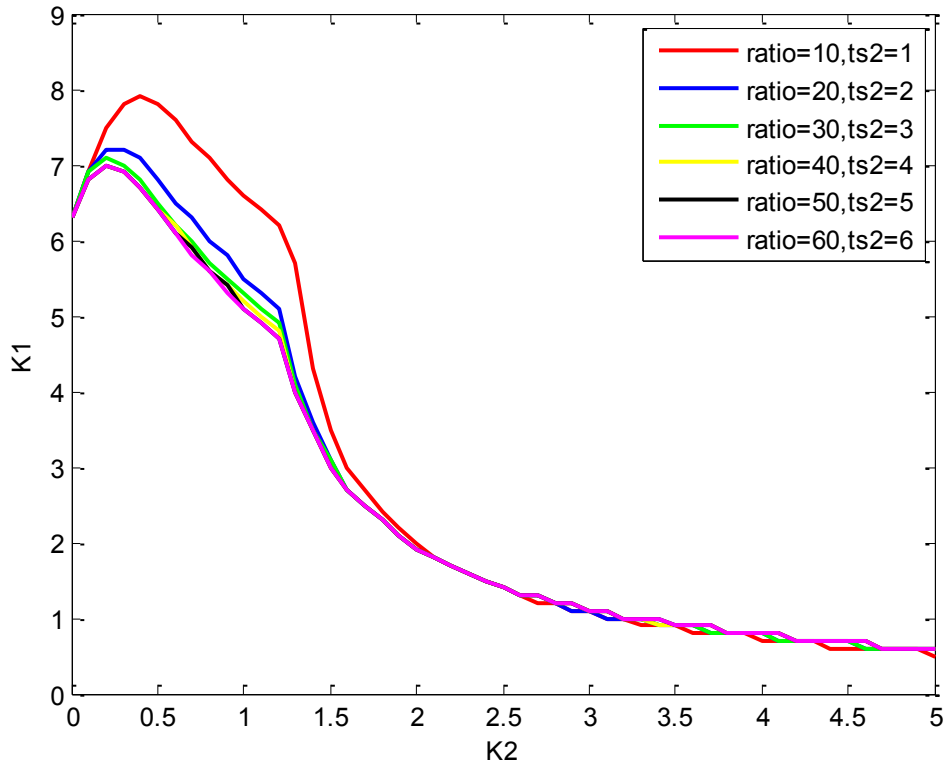


Figure F-3: Stability regions for the multi-rate cascade system: $ts_1 = 0.1$, $\tau_1 = \tau_2 = 1$, $k_{p1} = k_{p2} = 2$, and $\frac{\alpha_1}{ts_1} = \frac{\alpha_2}{ts_2} = 1$. Ratio is defined as $\frac{ts_2}{ts_1}$. The region below each curve is the stability region

## F.3 Sensitivity Analysis: the Effects of Process Model Parameters on the Multi-rate Cascade System's Stability

The sensitivity analysis of process model parameters $\alpha_1$ and $\alpha_2$ (time delay parameters) was carried out by determining the set of $\alpha_1$ and $\alpha_2$ such that the closed-loop system is stable based on the characteristic equation. The stability contour plots of $K_1$ versus $K_2$ for various time delays were obtained, shown in Figures F-4 and F-5. The region below each curve is the stability region. $m$, defined as $\frac{\alpha_1}{ts_1}$, represents the time delay of the inner loop, while $n$, defined as $\frac{\alpha_2}{ts_2}$, represents the time delay of the outer loop.

The simulation results show that $\alpha_1$ exerts the dominant effect on overall system stability (the stability region shrinks as $\alpha_1$ increases), while $\alpha_2$, has little effect on stability (the stability region does not change as $\alpha_2$ varies). Further, observed that the stability contours changes within a small range of the process gain of the outer loop $K_2$, while the stability contours changes along a large range of the process gain of the inner loop $K_1$ (see Figures F-2, F-3, F-4, and F-5). These results indicate that the overall stability of the control process is much more sensitive to the process model parameters of the inner loop compared to the process model parameters of the outer loop.

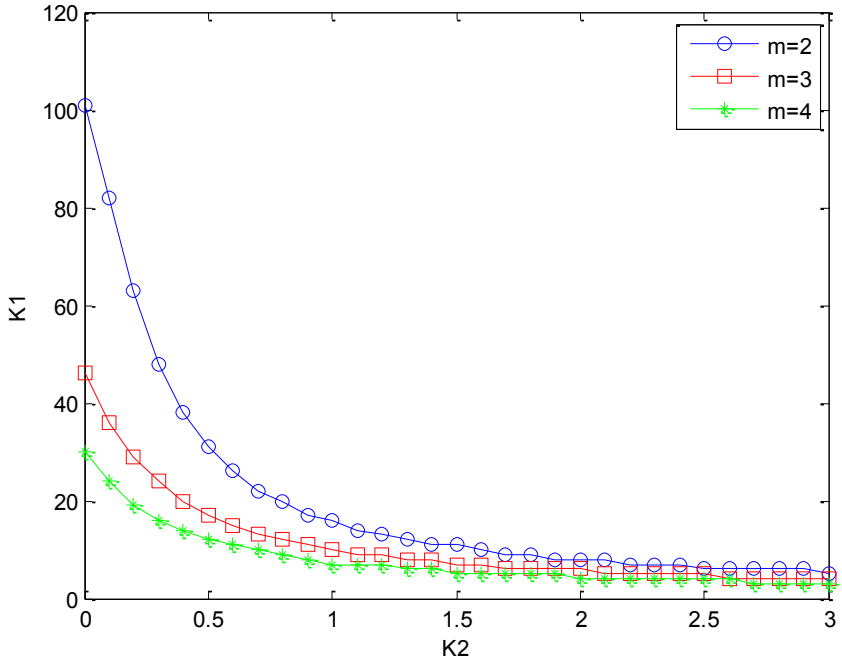


Figure F-4: Stability regions for the multi-rate cascade system: $m = \frac{\alpha_1}{ts_1}$, $ts_1 = 0.1, ts_2 = 70$, $\tau_1 = \tau_2 = 1$, and $k_{p1} = k_{p2} = 2$. The region below each curve is the stability region

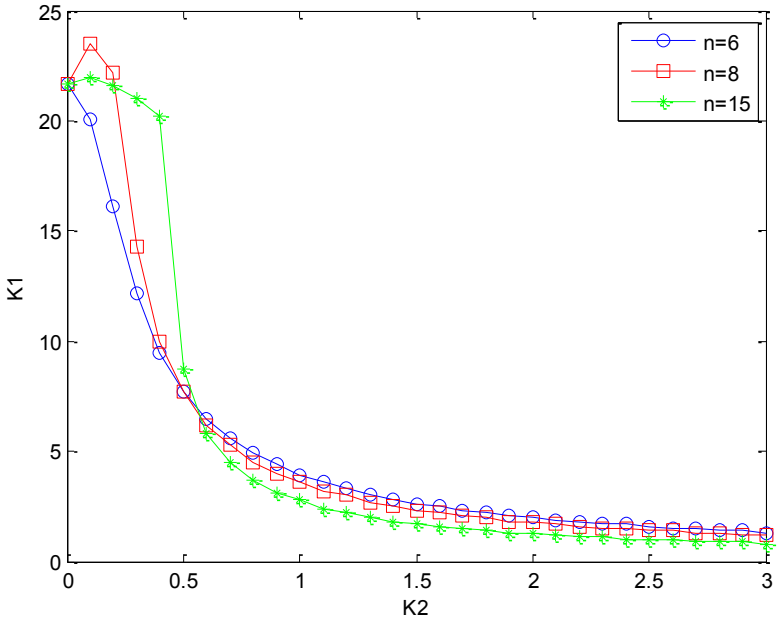


Figure F-5: Stability regions for the multi-rate cascade system: $n = \frac{\alpha_2}{ts_2}$, $ts_1 = 0.1, ts_2 = 70$, $\tau_1 = \tau_2 = 1$, and $k_{p1} = k_{p2} = 2$. The region below each curve is the stability region

## Appendix G

## DERIVATION OF CONTROL ACTIONS FOR CUSTOMER FEEDBACK CONTROLLER

For the specific case with two measured product attributes, the objective function is presented as follows:

$$\max_{\|\Delta \boldsymbol{w}_m\|} \pi(w_1, w_2) = \frac{e^{\beta_0+\beta_1 w_1+\beta_2 w_2}}{1+e^{\beta_0+\beta_1 w_1+\beta_2 w_2}} \quad \text{G-1}$$

where $\Delta \boldsymbol{w}_m = [\Delta w_1, \Delta w_2]^T$, and the BLR model parameters are estimated by MLE method using the historical customer response data. Considering the rearranged form of the BLR model in Equation 7-10, the objective function can be rearranged to:

$$\hat{\pi}^* = \beta_0 + \beta_1 w_1 + \beta_2 w_2 \quad \text{G-2}$$

where $\hat{\pi}^* = ln\left[\frac{\pi^*}{1-\pi^*}\right]$, and $\pi^*$ is the target probability. According to Equation 7-13, the objective function of Equation G-2 can be rewritten as:

$$\hat{\pi}^* = \beta_0 + \beta_1[w_1(k-1) + \Delta w_1(k)] + \beta_2[w_2(k-1) + \Delta w_2(k)] \quad \text{G-3}$$

from which, we obtain the expression of $\Delta w_2(k)$ as a function of $\Delta w_1(k)$:

$$\Delta w_2(k) = \frac{\hat{\pi}^* - \beta_0 - \beta_1[w_1(k-1)+\Delta w_1(k)]}{\beta_2} - w_2(k-1) \quad \text{G-4}$$

Also, the norm of control action vector $\Delta \boldsymbol{w}_m(k)$ can be expressed as:

$$\|\Delta \boldsymbol{w}_m\| = \sqrt{\Delta w_1^2(k) + \Delta w_2^2(k)} \quad \text{G-5}$$

Substituting $\Delta w_2(k)$ from Equation G-4 into Equation G-5, now the norm $\|\Delta \boldsymbol{w}_m\|$ is only related to the current control action $\Delta w_1(k)$ of the first element of product attributes:

$$\|\Delta \boldsymbol{w}_m\| = \sqrt{\Delta w_1^2(k) + \left[\frac{\hat{\pi}^* - \beta_0 - \beta_1[w_1(k-1) + \Delta w_1(k)]}{\beta_2} - w_2(k-1)\right]^2} \qquad \text{G-6}$$

Then, the minimum norm $\|\Delta \boldsymbol{w}_m\|$ can be obtained when the derivative of Equation G-6 equals to zero, that is:

$$\frac{d\|\Delta \boldsymbol{w}_m\|}{d(\Delta w_1(k))} = \frac{\Delta w_1(k) - \frac{\beta_1}{\beta_2^2}[\hat{\pi}^* - \beta_0 - \beta_1[w_1(k-1) + \Delta w_1(k)] - \beta_2 w_2(k-1)]}{\sqrt{\Delta w_1^2(k) + \left[\frac{\hat{\pi}^* - \beta_0 - \beta_1[w_1(k-1) + \Delta w_1(k)]}{\beta_2} - w_2(k-1)\right]^2}} = 0 \qquad \text{G-7}$$

Then, from equation G-7, we have obtained the control action $\Delta w_1(k)$ as follows:

$$\Delta w_1(k) = \frac{\hat{\pi}^* \beta_1 - \beta_0 \beta_1 - \beta_1 \beta_2 w_2(k-1) - \beta_1^2 w_1(k-1)}{\beta_1^2 + \beta_2^2} \qquad \text{G-8}$$

By substituting Equation G-8 into Equation G-4, the control action $\Delta w_2(k)$ yields:

$$\Delta w_2(k) = \frac{\hat{\pi}^* \beta_2 - \beta_0 \beta_2 - \beta_1 \beta_2 w_1(k-1) - \beta_2^2 w_2(k-1)}{\beta_1^2 + \beta_2^2} \qquad \text{G-9}$$

Therefore, the control actions to update the set-point targets for the measured product attributes can be expressed in a vector form as follows:

$$\Delta \boldsymbol{w}_m(k) = \begin{bmatrix} \frac{\hat{\pi}^* \beta_1 - \beta_0 \beta_1 - \beta_1 \beta_2 w_2(k-1) - \beta_1^2 w_1(k-1)}{\beta_1^2 + \beta_2^2} \\ \frac{\hat{\pi}^* \beta_2 - \beta_0 \beta_2 - \beta_1 \beta_2 w_1(k-1) - \beta_2^2 w_2(k-1)}{\beta_1^2 + \beta_2^2} \end{bmatrix} \qquad \text{G-10}$$

## Appendix H

## DERIVATION OF THE MINIMAL NONCENTRALITY PARAMETER $\lambda_{min}$ FOR THE ILLUSTRATIVE EXAMPLE WITH THREE-DIMENSIONAL PROPERTIES

In the specific illustrative example with the 3-dimensional $\boldsymbol{w}$ vector but for which only the 2-dimensional subset, $[w_1, w_2]^T$, is measured, in the event of a step change disturbance of magnitude $d$ affecting $w_3$, the noncentrality parameter $\lambda$ can be expressed as:

$$\lambda = [\delta_1 \quad \delta_2 \quad d]\boldsymbol{\Sigma}^{-1}\begin{bmatrix}\delta_1\\ \delta_2\\ d\end{bmatrix} \tag{H-1}$$

where $\delta_1$ and $\delta_2$ are the adjustments made for properties $w_1$ and $w_2$. Note that the disturbance $d$ is not transient and does not change with time. Thus, the noncentrality parameter $\lambda$ is a function of independent variables $\delta_1$ and $\delta_2$.

To determine the minimum of the variable $\lambda$ with respect to independent variables $\delta_1$ and $\delta_2$, we first need to calculate the stationary point and then determine whether this point is a minimal extremum or a maximal extremum.

First, the equation of $\lambda$ is rewritten as below:

$$\lambda = \frac{1}{\det|\boldsymbol{\Sigma}|}\begin{bmatrix}\delta_1\\ \delta_2\\ d\end{bmatrix}^T\begin{bmatrix}A & B & C\\ B & D & E\\ C & E & F\end{bmatrix}\begin{bmatrix}\delta_1\\ \delta_2\\ d\end{bmatrix} \tag{H-2}$$

where

$$\boldsymbol{\Sigma}^{-1} = \frac{1}{\det|\boldsymbol{\Sigma}|}\begin{bmatrix} A & B & C \\ B & D & E \\ C & E & F \end{bmatrix} \quad \text{H-3}$$

$$\begin{aligned} A &= (1-\rho_3^2)\sigma_2^2\sigma_3^2 \\ B &= \sigma_1\sigma_2\sigma_3^2(\rho_2\rho_3 - \rho_1) \\ C &= \sigma_1\sigma_2^2\sigma_3(\rho_1\rho_3 - \rho_2) \\ D &= (1-\rho_2^2)\sigma_1^2\sigma_3^2 \\ E &= \sigma_1^2\sigma_2\sigma_3(\rho_1\rho_2 - \rho_3) \\ F &= (1-\rho_1^2)\sigma_1^2\sigma_2^2 \end{aligned}$$

$$\det|\boldsymbol{\Sigma}| = \sigma_1^2 A + \rho_1\sigma_1\sigma_2 B + \rho_2\sigma_1\sigma_3 C \quad \text{H-4}$$

Then, Equation H-2 can be further simplified as:

$$\lambda = \frac{1}{\det|\boldsymbol{\Sigma}|}(A\delta_1^2 + D\delta_2^2 + Fd^2 + 2B\delta_1\delta_2 + 2B\delta_1 d + 2E\delta_2 d) \quad \text{H-5}$$

Based on Equation H-5, we calculate the first-order partial derivatives of $\lambda$ with respect to $\delta_1$ and $\delta_2$ respectively, given by

$$\frac{\partial\lambda}{\partial\delta_1} = \frac{1}{\det|\boldsymbol{\Sigma}|}(2A\delta_1 + 2B\delta_2 + 2Cd) \quad \text{H-6}$$

$$\frac{\partial\lambda}{\partial\delta_2} = \frac{1}{\det|\boldsymbol{\Sigma}|}(2D\delta_2 + 2B\delta_1 + 2Ed) \quad \text{H-7}$$

Then, setting these first-order derivatives to 0 and solving the equations, we obtain only one stationary point ($\delta_1^*$, $\delta_2^*$):

$$\delta_1^* = \frac{EB-CD}{AD-B^2}d \quad \text{H-8}$$

$$\delta_2^* = \frac{BC-AE}{AD-B^2}d \quad \text{H-9}$$

Next, we need to determine whether this point ($\delta_1^*$, $\delta_2^*$) is a minimal extremum or a maximal extremum. To tackle this problem, we derive all the second-order partial derivatives as follows.

$$\frac{\partial^2\lambda}{\partial\delta_1^2}=\frac{2A}{\det|\boldsymbol{\Sigma}|},\frac{\partial^2\lambda}{\partial\delta_2^2}=\frac{2D}{\det|\boldsymbol{\Sigma}|},\frac{\partial^2\lambda}{\partial\delta_1\delta_2}=\frac{2B}{\det|\boldsymbol{\Sigma}|} \quad \text{H-10}$$

Then, we have:

$$\left(\frac{\partial^2\lambda}{\partial\delta_1\delta_2}\right)^2-\frac{\partial^2\lambda}{\partial\delta_1^2}\cdot\frac{\partial^2\lambda}{\partial\delta_2^2}=\left(\frac{2B}{\det|\boldsymbol{\Sigma}|}\right)^2-\frac{2A}{\det|\boldsymbol{\Sigma}|}\cdot\frac{2D}{\det|\boldsymbol{\Sigma}|}=\frac{4\left(B^2-AD\right)}{(\det|\boldsymbol{\Sigma}|)^2} \quad \text{H-11}$$

Substituting Equation H-4 into Equation H-11, we obtain the following equation:

$$\left(\frac{\partial^2\lambda}{\partial\delta_1\delta_2}\right)^2-\frac{\partial^2\lambda}{\partial\delta_1^2}\cdot\frac{\partial^2\lambda}{\partial\delta_2^2}=\frac{4\delta_1^2\delta_2^2\delta_3^4\left(\rho_1^2+\rho_2^2+\rho_3^2-2\rho_1\rho_2\rho_3-1\right)}{(\det|\boldsymbol{\Sigma}|)^2} \quad \text{H-12}$$

Given the fact that the correlation coefficients are smaller than 1, the following inequality is always satisfied:

$$\left(\frac{\partial^2\lambda}{\partial\delta_1\delta_2}\right)^2-\frac{\partial^2\lambda}{\partial\delta_1^2}\cdot\frac{\partial^2\lambda}{\partial\delta_2^2}<0 \quad \text{H-13}$$

Also, the square of the second partial derivative regarding to $\delta_1$ is always larger than 0, which is:

$$\left(\frac{\partial^2\lambda}{\partial\delta_1^2}\right)^2=\left(\frac{2A}{\det|\boldsymbol{\Sigma}|}\right)^2>0 \quad \text{H-14}$$

By the Second Partial Derivative Test [145], the stationary point ($\delta_1^*$, $\delta_2^*$) is a minimal extremum of the function $\lambda(\delta_1, \delta_2)$. Therefore, $\lambda_{min}$ is obtained at this stationary point when $\delta_1 = \delta_1^*$ and $\delta_2 = \delta_2^*$ (see Equations H-8 and H-9).